Material Properties of Thermoelectric and Nuclear Energy Sources

A Dissertation
Presented in Partial Fulfillment of the Requirements for the
Degree of Doctor of Philosophy
with a
Major in Mechanical Engineering
in the
College of Graduate Studies
University of Idaho
by

Courtney Hollar

Major Professor: Ralph Budwig, Ph.D.
Committee Members: David Estrada, Ph.D.; Kamal Kumar, Ph.D.;
Yanliang Zhang, Ph.D.
Department Administrator: Steven Beyerlein, Ph.D.

May 2019

AUTHORIZATION TO SUBMIT DISSERTATION

This dissertation of Courtney Hollar, submitted for the degree of Doctor of Philosophy with a Major in Mechanical Engineering and titled “Material Properties of Thermoelectric and Nuclear Energy Sources," has been reviewed in final form. Permission, as indicated by the signatures and dates given below, is now granted to submit final copies to the College of Graduate Studies for approval.

Major Professor: _____ Date: _____

Ralph Budwig, Ph.D.

Committee Members:

_____ Date: _____

David Estrada, Ph.D.

_____ Date: _____

Kamal Kumar, Ph.D.

_____ Date: _____

Yanliang Zhang, Ph.D.

Department Administrator:

_____ Date: _____

Steven Beyerlein, Ph.D.

ABSTRACT

Thermoelectric generators are a reliable solid-state energy conversion technology. Furthermore, flexible thermoelectric generators are especially of interest due to their potential to power flexible electronics and sensors using body heat or other ambient heat sources. This research focuses on developing flexible, bismuth telluride thin films utilizing a low-cost and scalable wet chemistry method. An overview of current alternative small energy sources demonstrates the need for flexible thermoelectric generators. Thin films fabricated from bismuth telluride nanocrystals exhibited a peak power factor of 0.35 $mW/m \cdot K^2$ at 433 K, which is among the highest reported values for flexible thermoelectric films. In addition, the change in electrical resistance was 23% after 1000 bending cycles.

Nuclear energy is a large scale energy alternative to fossil fuels which generate minimal environmental emissions. However, the thermal conductivity of nuclear fuel is necessary due to its impact on fuel temperature, the resulting reactor performance, and safety considerations. This research works to overcome this problem by utilizing an in-pile thermal conductivity measurement in order to determine the thermal conductivity under prototypic conditions over a range of burnup. A multilayer quadrupoles analytic model is developed to describe the transient thermal interactions between a line heat source and nuclear fuel for in-pile thermal conductivity measurements. The analytic model was verified using a finite element analysis. Ultimately, the analytic model was used to perform parameter and sensitivity studies to explore the viability of accurately measuring the sample thermal conductivity under various measurement conditions. The analytic model was then compared to experimental measurements of polytetrafluoroethylene and stainless steel 304, which showed good agreement. Using the analytic model, optimization of the needle probe was then performed in order to improve the accuracy of thermal conductivity measurements for UO_2 related to the fuel diameters, various probe diameters, and thermal contact resistance. The standard equation for data reduction using the slope to determine the thermal conductivity is not capable of measuring samples with prototypic diameters. However, the validated analytic model provides the foundation to elucidate a better understanding of in-pile thermal conductivity measurements in samples with a diameter as low as 10 mm.

ACKNOWLEDGEMENTS

I would like to thank Dr. Ralph Budwig for his guidance and encouragement throughout this project. Thank you for your support throughout this process and for being an advocate of mine. Thank you to Dr. David Estrada for your continuous mentorship and for supporting my research. I am extremely grateful for you bringing me into the Advanced Nanomaterials and Manufacturing Laboratory and for the opportunities you presented me. I could not have done this without both Dr. Ralph Budwig and Dr. David Estrada. Thank you to Dr. Kamal Kumar and Dr. Yanliang Zhang for being part of my dissertation committee. I would like to thank the National Science Foundation for their generous support received through the Graduate Research Fellowships Program. Funding for this project has also been supported through the Department of Energy In-Pile Instrumentation program. Thank you to the research team at the Advanced Nanomaterials and Manufacturing Laboratory, in particular Tony Varghese, who helped obtain some of the results presented in this dissertation and co-authored publications. Thank you to the Idaho National Laboratory; especially Dr. Austin Fleming, Kurt Davis, and Dr. Colby Jensen for their assistance throughout the project.

DEDICATION

I am grateful to have the love and support of Khris and Lucy throughout this chapter of my life. I am appreciative of my family as they continuously provide love and guidance throughout my life. Furthermore, I am thankful for the Kohlmeier family and the support they have shown through these years.

TABLE OF CONTENTS

LIST OF TABLES

LIST OF FIGURES

LIST OF ABBREVIATIONS

1-D	One-Dimensional
AFM	Atomic Force Microscopy
AJP	Aerosol Jet Print
Bi_2Te_3	Bismuth Telluride
CO_2	Carbon Dioxide
Cu_2Se	Copper Selenide
EDS	Energy-Dispersive X-Ray Spectroscopy
EFTEM	Energy Filtered Transmission Electron Microscopy
EG	Ethylene Glycol
f-TEGs	Flexible Thermoelectric Generators
HTIR-TC	High Temperature Irradiation Resistant Thermocouple
INL	Idaho National Laboratory
IPA	Isopropyl Alcohol
ITO	Indium Tin Oxide
LFA	Laser Flash Analysis
PTFE	Polytetrafluoroethylene
PVP	Polyvinylpyrrolidone
ROC	Radius of Curvature
TE	Thermoelectric
TEGs	Thermoelectric Generators
TEM	Transmission Electron Microscopy
TDTR	Time-Domain Thermoreflectance

SEM	Scanning Electron Microscopy
STEM	Scanning Transmission Electron Microscopy
SThM	Scanning Thermal Microscope
UO_2	Uranium Dioxide

STATEMENT OF CONTRIBUTION

Multiple chapters of this dissertation draw from previously published work which has been submitted through the peer-review process. The author of this dissertation was the lead author of the publications included in this work. This research was funded through a variety of sources and would not have otherwise been possible.

The work in chapter 3 includes text and figures from "High-Performance Flexible Bismuth Telluride Thin Film from Solution Process Colloidal Nanoplates". In this project, my role was to synthesize and prepare bismuth telluride ink used for spin coating and aerosol jet printing. I also fabricated thin films through spin coating, performed static and dynamic bend tests, as well as prepared samples for transmission electron microscopy (TEM), scanning transmission electron microscopy (STEM), atomic force microscopy (AFM), and energy-dispersive X-ray spectroscopy (EDS). Finally, I measured the thermoelectric properties of various thin films and supplied the initial text of the publication. Co-authors included Zhaoyang Lin, Madhusudan Kongara, Tony Varghese, Chinnathambi Karthik, Jesse Schimpf, Yaqiao Wu, Xiangfeng Duan, Yanliang Zhang, and David Estrada. Zhaoyang Lin synthesized some of the ink and fabricated some of the films used during experiments. Madhusudan Kongara helped me synthesize the initial batches of ink. Tony Varghese aerosol jet printed flexible films. Chinnathambi Karthik performed TEM and EDS of the ink and nanoplates to determine the composition. Jesse Schimpf performed AFM to determine the width and thickness of nanoplates. Yaqiao Wu performed STEM and EDS of the nanoplates and films. Xiangfeng Duan and Yanliang Zhang provided feedback on the publication text. David Estrada provided oversight and guidance of the overall project. All co-authors provided feedback on the publication text. This manuscript has currently been submitted.

The work in chapter 4 includes text and figures from "A Parametric Study for In-Pile use of the Thermal Conductivity Needle Probe using a Transient, Multilayer Analytic Model". This work was supported through the Department of Energy In-Pile Instrumentation program, under DOE Idaho Operations Office Contract DE-AC07-05ID14517. My role in this project was to develop a transient, multilayer analytical model using the quadrupoles

method, conduct and collect experimental data for validation, and perform sensitivity and optimization studies. I supplied the initial text of the publication. Co-authors on this work included Austin Fleming, Kurt Davis, Ralph Budwig, Colby Jensen, and David Estrada. Austin Fleming assisted with development of the analytic model. Kurt Davis helped with the set-up of the needle probe for experiments. Ralph Budwig provided feedback related to the development of the analytic model. Colby Jensen and David Estrada provided oversight and guidance of the overall project. All co-authors provided feedback on the publication text. This manuscript has currently been submitted.

CHAPTER 1: INTRODUCTION

1.1 Overview of Energy Landscape in the United States

There are many energy challenges currently being faced in the United States. According to the Department of Energy's Quadrennial Technology Review, energy technologies in the United States must consider security of supply, cost, environmental impacts, reliability, land and material use[1]. Currently, 82% of the primary energy usage is supplied by fossil fuels[1]. However, it is known that fossil fuels, such as coal and natural gas, produce the largest amount of carbon dioxide. In 2016, the U.S. Energy Information Administration reported that energy consumption through fossil fuels produced 76% of the total anthropogenic greenhouse gas emissions, which also resulted in 94% of the total carbon dioxide emissions in the country (Figure 1.1)[2].

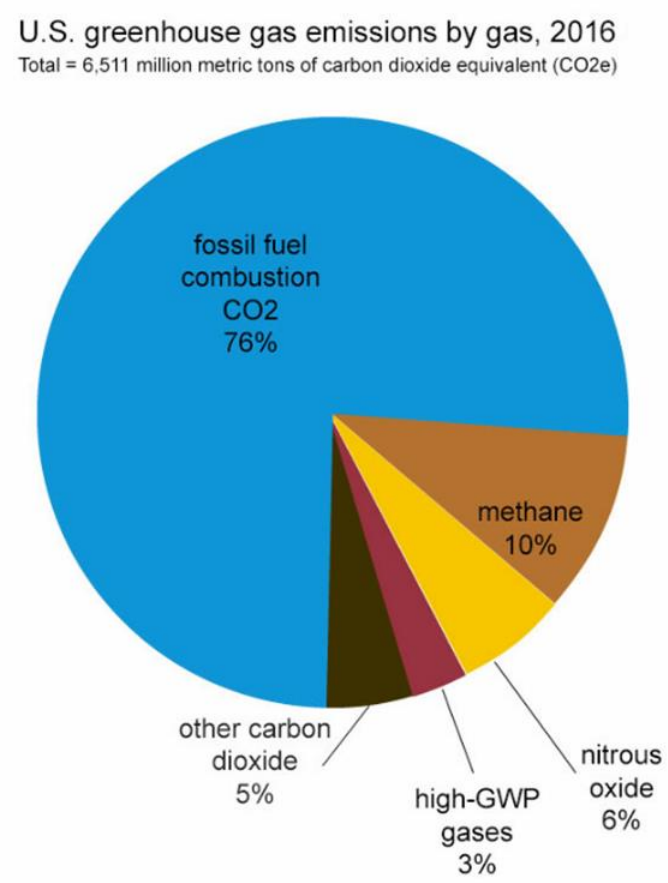

Figure 1.1: U.S. greenhouse gas emissions by gas, 2016[2]

As more and more concern grows, related to the environmental impacts of fossil fuels, long-term sustainability must also be considered. Another challenge is reducing the amount of energy loss.

Figure 1.2 illustrates the various energy resources, the conversion into fuels and electricity, and the different sectors that use energy. The transportation sector uses about 28% of the U.S.'s energy, the industry sector uses 25%, and the commercial sector uses 9%. Since the energy conversion process is not 100% efficient, approximately 40% of the total energy is turned into usable energy while the remaining 60% is rejected energy. One solution to improving the energy efficiency is the utilization of waste heat recovery and thermal storage.

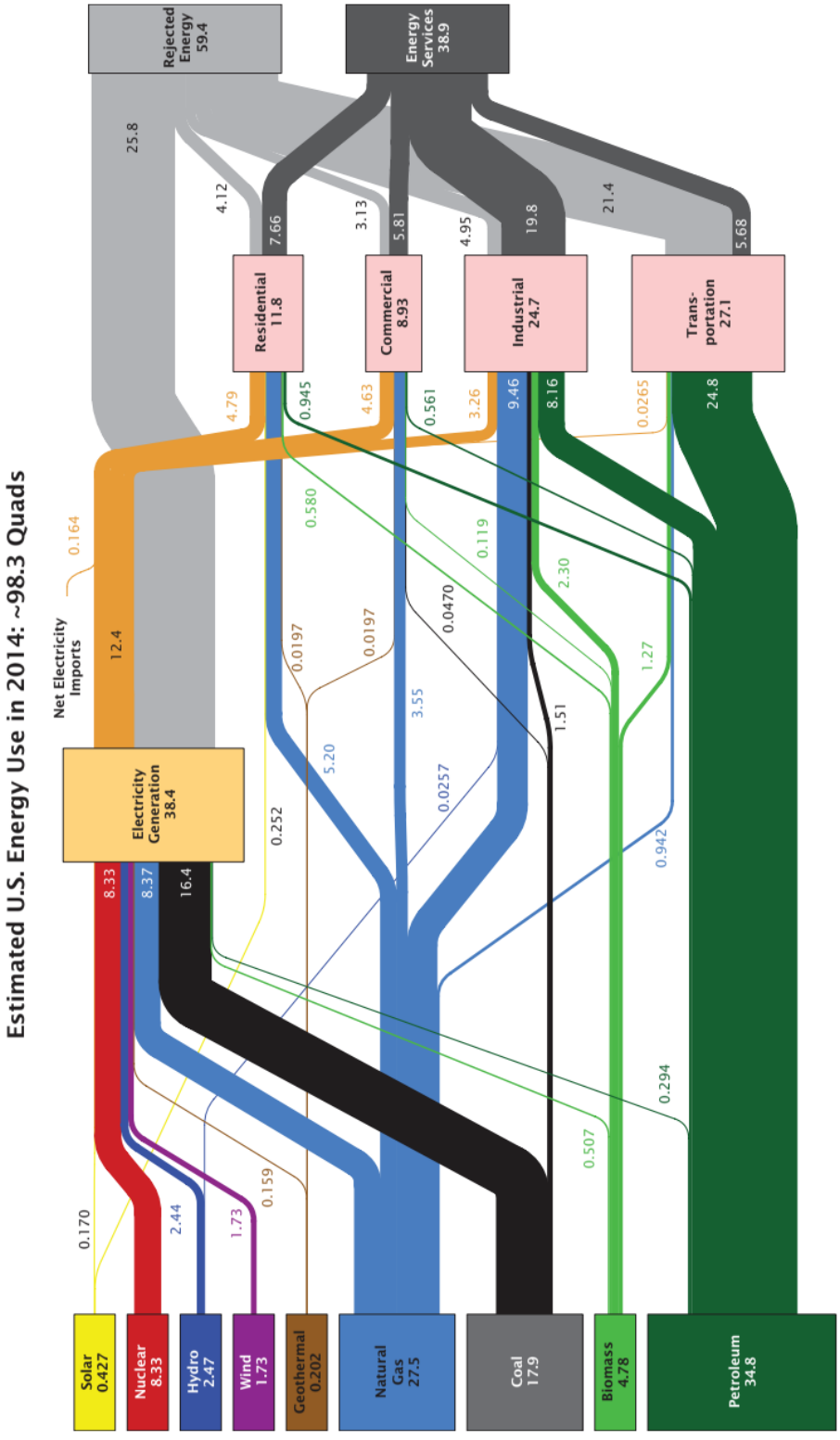

Figure 1.2: U.S. energy resource distribution[1]

1.2 Overview of Existing Energy Sources: Small Scale Energy Sources

As wearable devices, medical instrumentation, and other portable electronics continue to gain popularity, it is necessary to realize the current energy consumption challenges. Energy usage in the United States is currently in excess of 20 GW, which is 5% to 10% of the national electricity budget. Furthermore, energy consumption has doubled in five recent years[3].

With the advancement of wearable devices and sensors, even more data will need to be stored in data centers. Currently, the average data center consumes approximately 25,000 households' worth of energy[4]. The most important factor, which is limiting the performance of data centers, is the need for 50% to 100% additional energy for cooling[3]. Based on the present growth trends, the energy usage for data centers and electronics could reach one third of the total U.S. consumption by 2025. In fact, the amount of equivalent CO_2 emissions generated from data centers is roughly equivalent to 5 million cars[5].

Therefore, it is necessary to consider both low-energy computer devices as well as better heat dissipation. This section will evaluate several small scale energy sources.

Lithium-Ion Polymer Battery

Most small scale energy devices use conventional power sources such as lithium-ion polymer batteries. Since most devices have a longer lifespan than lithium-ion polymer batteries, occasional replacement or recharging is necessary.

In addition, some small scale energy devices require placement on irregularly curved surfaces. Utilizing a rigid lithium-ion polymer battery makes it difficult to achieve a fully flush fit between the device and the curved surface. As a result, the thickness and rigidity of lithium-ion polymer batteries limits the possible device designs.

Lithium-ion polymer batteries have been selected as the main power source for such devices due to their energy density of 2880 J/cm^3, versatility, and reliability[6]. Lithium-ion polymer batteries also use a solid electrolyte for producing power which can result in minimal battery leakage compared to alternative liquid batteries[7]. As of now, lithium-ion polymer batteries have proven to be the mainstay; however other alternatives such as piezoelectric,

electromagnetic, electrostatic, and thermoelectric power sources are currently being researched.

Piezoelectric Power Source

The piezoelectric effect is when an electrical voltage is created that is proportional to the mechanical strain the material undergoes, as seen in Figure 1.3. This effect can be used to convert mechanical motion to electrical energy. Roundy *et al.* demonstrated that a $1cm^3$ piezoelectric power source can produce 200 μW[6]. Since mechanical strain in the material is necessary to create the piezoelectric effect, this means the device must be placed in higher force areas. The placement of the power source determines how much power will be produced. Placing the piezoelectric generator on an object that cannot produce high forces frequently will result in a lack of electrical energy[8].

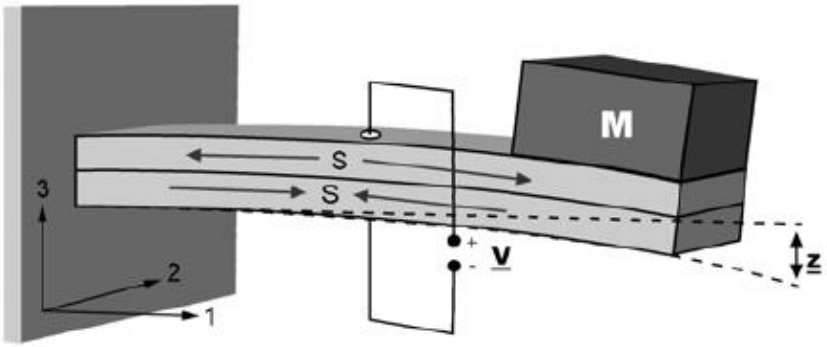

Figure 1.3: Piezoelectric generator[9]

Electromagnetic Power Source

Electromagnetic generators are comprised of a coil of tightly wrapped wires that move through a magnetic field, which generates a voltage. The amount of voltage generated depends on the strength of the magnetic flux between the coil and magnetic field. Electromagnetic generators use the magnetic induction principle in order to convert the mechanical vibrations between a coil and magnet to produce electrical energy[10, 11]. Electromagnetic power sources have the ability to produce 46 μW, this translates into a 307 $\mu W/m^3$ maximum power density[12]. The basic design principle of electromagnetic generators

is to have the magnet or coil move relative to the other, however, there are several types of designs. Figure 1.4 shows an electromagnetic generator that utilizes a cantilever type design.

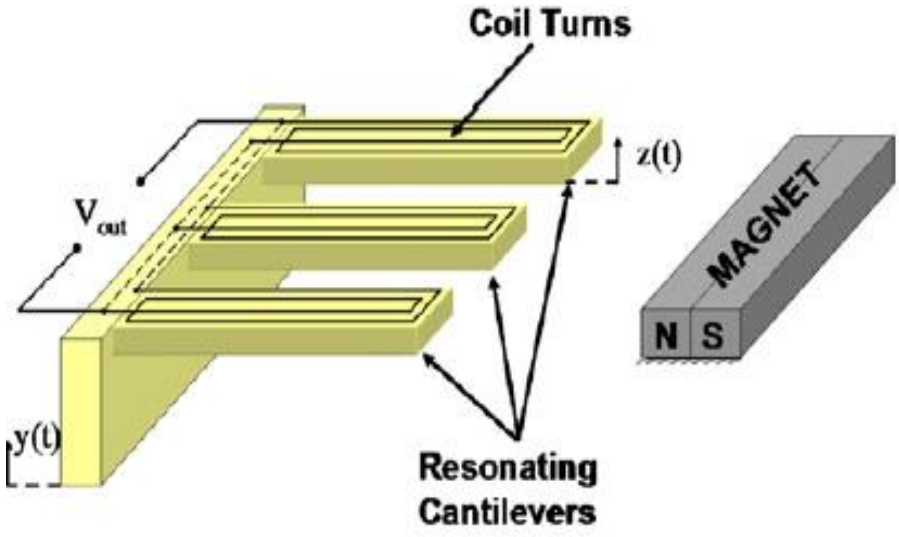

Figure 1.4: Electromagnetic generator[13]

Electrostatic Power Source

Electrostatic generators convert mechanical vibrations into electrical energy by using a transducer that moves against an electrical field. The energy is then harvested based on the charging of capacitor plates. A voltage across the capacitor occurs when vibrations or any other mechanical motion separates the plates of the charged capacitor. This voltage can then be used for different applications. A power density of 58 $\mu W/cm^3$ has been reported by Paracha *et. al.*[14]. Figure 1.5 shows a honeycomb-type capacitor design to convert the mechanical energy into electrical energy[15].

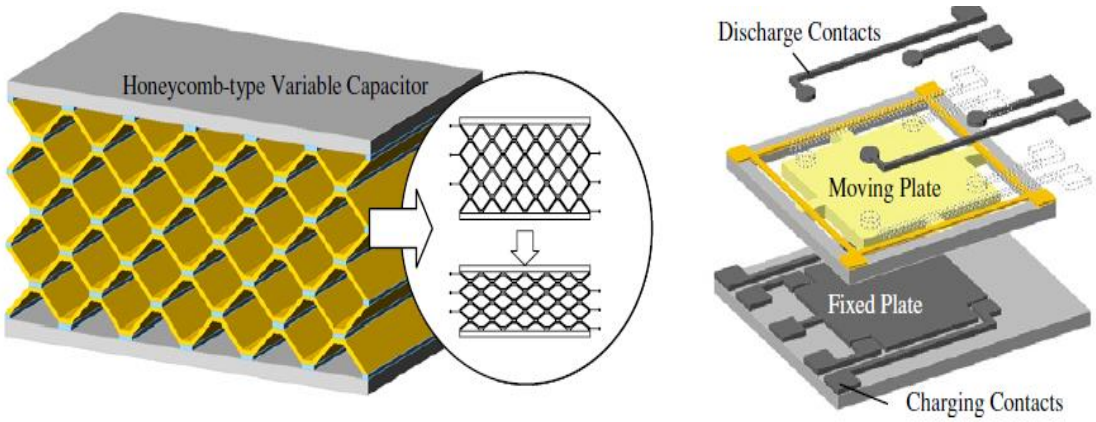

Figure 1.5: Two types of electrostatic generators: (left) variable-capacitance-type capacitor and (right) variable-gap parallel-plate capacitor[15]

Pizeoelectric, electromagnetic, and electrostatic power sources are all examples of small scale energy harvesters. However, these energy harvesters require continual mechanical vibrations in order to create a steady source of electrical energy. Consequently, if the desired location for placing a small scale energy harvester does not offer any consistent movement, the generator required to power the device will no longer work. Therefore, capacitors are incorporated into the final design to help provide a permanent, steady supply of electrical energy to the devices[16, 17].

Developing a power source that can provide a continual supply of energy without the requirement of movement allows for more placement options. Development of a thermoelectric generator that can produce power in the μW range would increase and advance power source options for the energy harvesting field.

Thermoelectric Generators

Thermoelectric generators (TEGs) make for an ideal power source due to their ability to produce power without the need for mechanical vibrations. Most of the previously discussed power sources depended on some kind of movement or exertion of force to generate the necessary electrical energy. Thermoelectric (TE) materials use the Seebeck effect to convert thermal energy into electrical energy. When a temperature gradient is applied across a semiconductor or conductor material, a voltage is generated, also referred to as the Seebeck voltage[18-21]. Figure 1.6 shows two materials, such as a metal and semiconductor, which have formed a junction to create a TEG. The junction is formed between a high electrically

conductive metal, such as silver, and the two TE materials. This allows the TE materials to be connected electrically in series but thermally in parallel. Placing the TE materials in parallel allows for the Seebeck effect to be utilized. The Seebeck effect occurs when the electrical charge carriers travel from the hot side to the cold side. At the hot side, there is increased thermal energy and the charge carrier energy increases while the charge carrier energy at the cold side decreases. In order to reach equilibrium, the charge carriers diffuse from the hot side to the cold side, thus creating a potential difference. This electrochemical potential is referred to as the Seebeck voltage and it occurs as a result of the thermal gradient. Therefore, when a small temperature gradient is applied, the Seebeck voltage is directly proportional to the temperature difference.

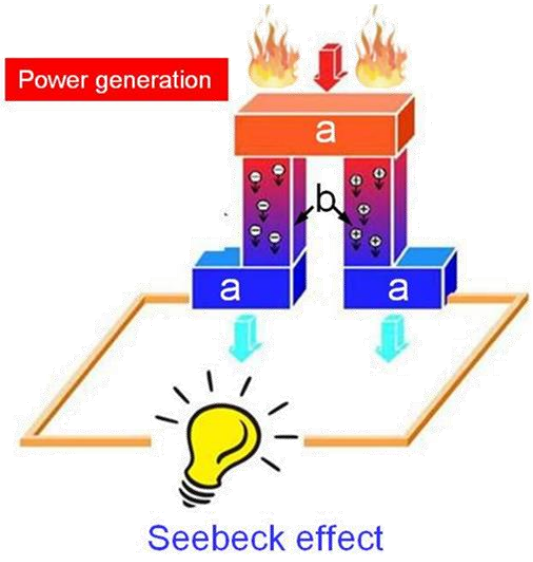

Figure 1.6: Schematic of TEG[22]

The prior mentioned alternative energy sources utilized rigid designs, making it limiting and difficult to use for flexible devices. Recently, utilizing thin film TEGs have gained interest as a potential power solution. The fabrication of flexible TEGs allows for the device to be applied to irregularly curved surfaces and still provide power to the device[23]. TEGs have the ability to produce power in the µW to mW range[23, 24]. For instance, a TEG has been shown to produce 100 µW to 150 µW for a person who has a lower metabolic rate. However, with increased physical activity, a typical TEG can produce between 500 µW to 700 µW[25].

In addition to using TEGs for various waste heat applications, utilizing TEGs on the human body provides an opportunity for small scale energy harvesters to recover the waste body heat. The largest temperature gradient within the human body is between the skin and the air next to it. Wearable devices use the temperature gradient created between the heat of the human skin and the relative cold room temperature. For such wearable sensors, it is possible to achieve a temperature gradient greater than $10^{o}C$[26, 27]. Thus converting human waste heat into electricity may be used to power small devices in addition to advancing the energy harvesting field.

In order for flexible TEGs to be a more mainstream alternative power source for devices, the TEG must have an optimized efficiency. TEGs are comprised of two different TE materials, an n-type and a p-type. Therefore, creating an optimized TEG requires that highly efficient TE materials are used. High efficiency TE materials must exhibit a high Seebeck coefficient and electrical conductivity and low thermal conductivity. This study will focus on the transport properties of TE films.

1.3 Overview of Existing Energy Sources: Large Scale Energy Sources

Fossil Fuels

Energy sources that are deemed "fossil fuels" consist of coal, natural gas, and petroleum. These are nonrenewable energy sources since they do not form or replenish in a short period of time. Most fossil fuels use various types of turbines to generate electricity and continue to be the largest source of energy for electricity generation in the U.S.[28]. For more than 100 years, fossil fuels have provided more than 80% of the electricity for the U.S.[29].

In 2017, natural gas was the largest source used for U.S. electricity generation, which made up about 32% of the energy used[28]. Natural gas uses steam turbines and gas turbines to convert the burning of natural gas to electricity. The U.S. has been the largest gas producer in the world since 2009 and is expected to increase production in the next five years[29, 30].

Coal is the next largest energy source for the U.S., making up about 30% of the energy used in 2017[28]. Most coal-fired power plants use steam turbines, while fewer plants use gas turbines. As of 2016, the world produced approximately 6.5 billion tons of coal[31].

Petroleum made up less than 1% of U.S. electricity in 2017[28]. Depending on the type of petroleum, steam turbines, diesel-engine generators, or gas turbines will be used for electricity generation. Petroleum is the main source of energy consumption for transportation, homes, businesses, and industries[32]. Consumption of petroleum has increased in each of the past four years[32]. The U.S. has been the top producer of petroleum since 2013[33].

The burning of all forms of fossil fuels result in the emission of CO_2 from carbon that had previously been sequestered underground. There is more and more concern about the environmental impacts of using coal as an energy source. In 2015, coal consumption in the U.S. dropped by 13%[29]. The U.S. Energy Information Administration expects the percentage of fossil fuel usage to decline to 76.6% by 2040[29]. In addition, this projection could significantly change based on policy changes and technological advancements. Figure 1.7 shows the projected energy usage for the U.S.[29].

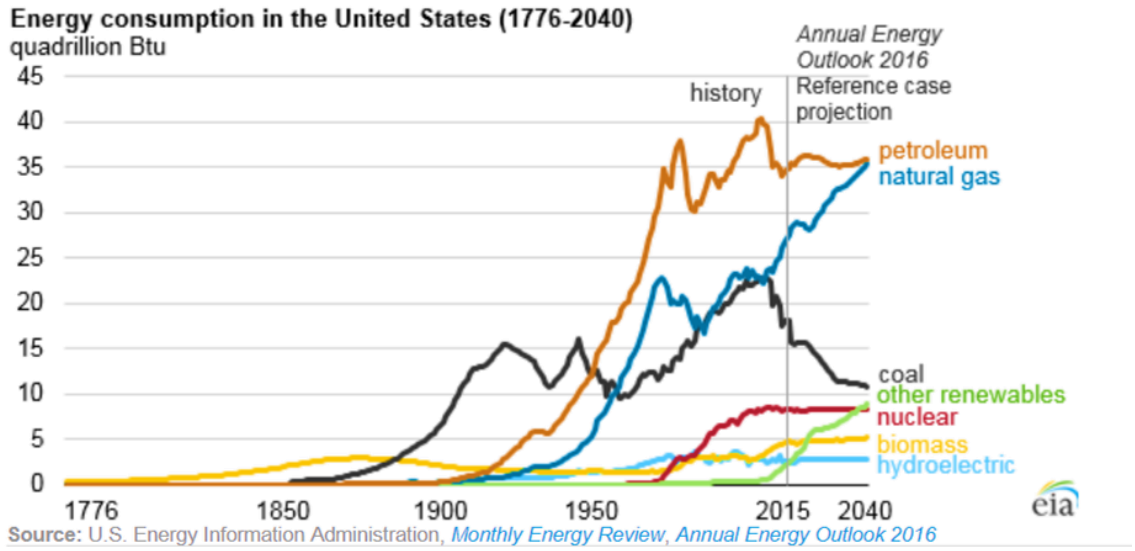

Figure 1.7: Annual energy consumption in the U.S.[29]

Solar

There are several types of solar energy. The main types of energy sources are photovoltaic and solar-thermal. Photovoltaic solar energy converts the sunlight directly into electricity using photovoltaic cells. Solar-thermal power systems use steam turbines to convert sunlight into electricity. In 2017, solar energy provided about 1% of the electricity in the U.S. or 4.58 GW[28]. From 2020 to 2050, it is expected that solar photovoltaic capacity will

grow by 127 GW, as can be seen in Figure 1.8[34]. In addition, technological advancements in storage systems are working on providing several hours of storage and to supply electricity at peak demand times[34].

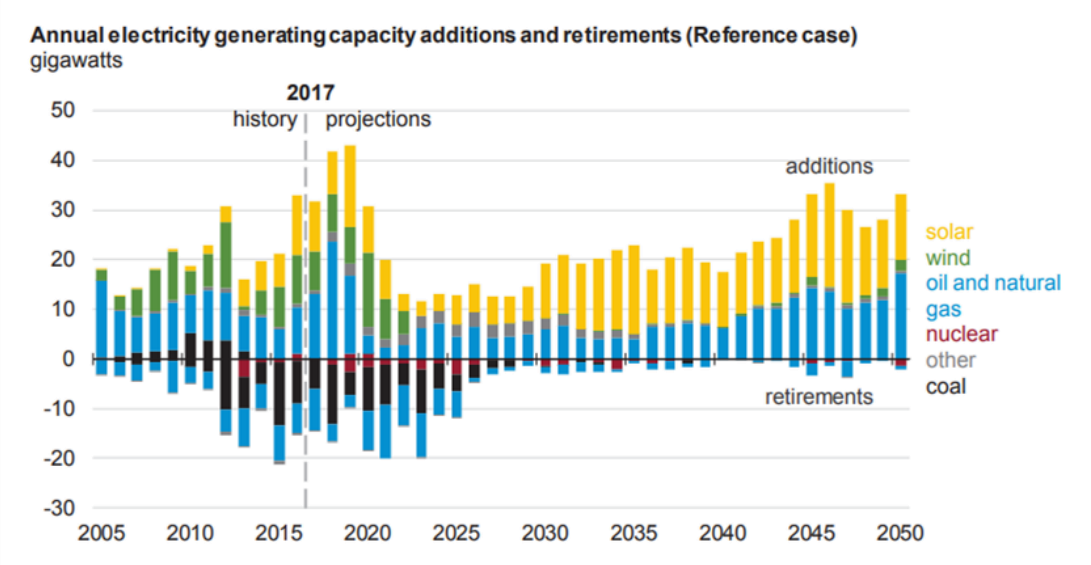

Figure 1.8: Projected electricity generating capacity additions and retirements[34]

Nuclear

Unlike solar energy, nuclear energy continuously produces electricity regardless of external environmental factors such as cloud coverage. Furthermore, nuclear power plants can be located in any region, while solar energy needs to be deployed in optimal locations in order to maximize power output.

Nuclear energy converts a nuclear chain reaction to electricity by producing a desired amount of heat. Most nuclear power plants use a relatively rare type of uranium, U-235, due to the atoms relative ease of splitting apart[35]. Nuclear reactors depend upon large cooling towers in order to transfer heat from the reactor core to the steam turbines and also to remove surplus heat from the steam circuit. In 2017, nuclear energy provided about 20% of the electricity to the U.S.[28]. The Nuclear Energy Institute reports that nuclear energy produces 62% of all emission-free electricity in the U.S.

Nuclear energy has been a significant part of global electricity generation due to the high energy density and long asset lifetime and reliability. In addition, nuclear reactors contribute to the security of electricity while generating minimal environmental emissions

such as greenhouse gasses[36]. It is predicted that oil, coal, and gas will be depleted in 35, 107, and 37 years, respectively. Furthermore, coal reserves will be available up until 2112, making this the only remaining fossil fuel after 2042[37]. Meanwhile, the Nuclear Energy Agency has estimated the world's uranium resources to run nuclear reactors for approximately 230 years[38].

One concern that is especially related to my research is the need for a stable grid in order for nuclear energy to be a larger producer of the U.S. energy needs. Currently, the electric grid consists of a series of networks that are defined by geography. This means if one place is experiencing failure, the surrounding system is dependent— which may lead to a cascade of the entire system failing. Since nuclear energy relies on the production of heat by using a nuclear chain reaction, the temperature of the nuclear material remains hot for a very long time. Therefore, if the electric grid suddenly shuts off and back-up generators are not working, the nuclear plant will continue to produce heat due to the radioactive decay that was generated[39]. Thus, a more stable grid must be implemented before nuclear energy can be more widely used.

The excess heat that nuclear power plants produce also presents the possibility for thermal energy storage. In some cases, the heat produced by the nuclear plant may exceed the grid demand. In this case, heat storage should be considered as a way to store the energy to be used during peak energy demand times.

In order for nuclear energy to be considered a more primary energy source, there needs to be a better understanding of nuclear fuel. Thermal properties of nuclear materials aid in the proper design, testing, and application of new fuels, and structural materials of nuclear reactors[40]. During irradiation, the physical structure and chemical composition of nuclear fuels changes based on time and the location within the rod. Currently, there is minimal thermal property data available for such fuels. In addition, this information is necessary to develop the simulation design codes of next generation reactors.

Post-irradiation examinations are used to determine the thermal conductivity of nuclear fuels[41]. This is a costly technique that only provides a time-frame by time-frame understanding of the fuel's thermal conductivity. This approach also risks damaging the fuel each time it is taken in and out of the reactor for thermal conductivity testing. This study will

focus on the development of an in-situ technique to measure the thermal conductivity of nuclear fuels.

CHAPTER 2: REVIEW OF TRANSPORT PROPERTY MEASUREMENTS AND MODELING METHODS

2.1 Characterization Methods for Transport Property Measurements of Thermoelectric Materials

In order to determine the efficiency of TE materials, the dimensionless figure of merit (Equation 2-1) is used.

$$ZT = \frac{\alpha^2 \sigma}{\kappa} T \qquad [2\text{-}1]$$

where α, σ, κ, and T are the Seebeck coefficient, electrical conductivity, thermal conductivity, and absolute temperature, respectively[42, 43]. Many studies focus on measuring the power factor, $\alpha^2\sigma$, due to the difficulty to accurately measure the thermal conductivity of thin film TE materials.

The figure of merit is an important equation that provides a way to compare the material's overall TE properties. Maximizing the figure of merit indicates that the material has the ability to efficiently produce TE power. TEGs that utilize TE materials with a low figure of merit will be less efficient. In order to maximize the figure of merit of a TE material, the Seebeck coefficient and electrical conductivity must be large while the thermal conductivity is minimized[44]. A low thermal conductivity is able to maintain a large temperature gradient while minimizing heat flow from the hot and cold side. The electrical conductivity needs to be high in order to efficiently conduct electrical current. It is also important the Joule heating is minimized, which can affect the thermal conductivity. Materials that have a large Seebeck coefficient will generate a large Seebeck voltage when a temperature gradient is present.

It is difficult to maximize the electrical conductivity and Seebeck coefficient while minimizing the thermal conductivity. This is because these material properties are a result of the material's electronic structure and the scattering of charge carriers, which make it difficult to isolate and independently control one property[45].

Seebeck Coefficient

The Seebeck coefficient is a thermoelectric property that is independent of sample dimension. Equation 2-2 shows that the Seebeck coefficient requires a temperature gradient to be applied while the induced voltage is measured.

$$S = -\frac{V}{\Delta T} \qquad [2\text{-}2]$$

where V and ΔT are the voltage induced by the sample and the temperature difference between two points, respectively.

In order to measure the in-plane Seebeck coefficient, a temperature gradient needs to be applied across the surface of the sample. This is typically achieved by suspending the sample across two isothermal blocks, as shown in Figure 2.1. Generally, a large copper block is used as the heat sink while a strain gage or cartridge heater serves as the heat source[46, 47]. While the sample maintains a steady temperature gradient, the sample will begin to generate a voltage. The voltage is measured using two electrical probes while thermocouples are placed at the same location to determine the magnitude of the temperature difference. A negative Seebeck coefficient indicates an n-type material while a positive Seebeck coefficient indicates a p-type material.

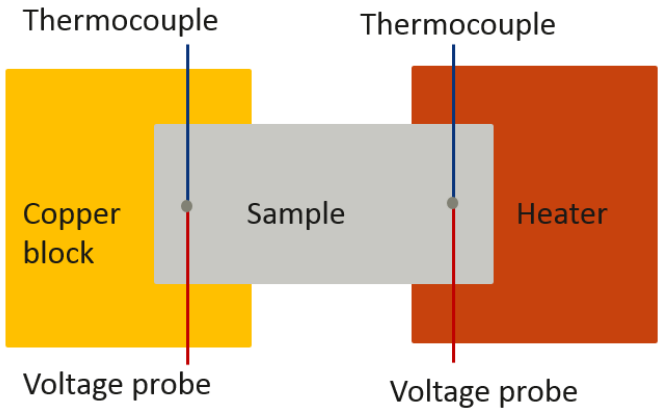

Figure 2.1: In-plane differential Seebeck measurement set-up[48]

The differential Seebeck measurement approach is the most common method that applies a small thermal gradient along the sample. Multiple data points with varying temperature differences are collected. The linear slope of the voltage v. temperature gradient results in the Seebeck coefficient. Waiting for thermal equilibrium will result in improved

accuracy and high linearity. Achieving good thermal contact can also affect the accuracy of the results. This can be difficult for many thin and thick films without damaging the film surface.

Electrical Conductivity

This section will discuss two main measurement methods used to characterize the electrical conductivity of thin and thick film materials.

Linear Four-Point Probe

The linear four-point probe method is the most common characterization approach to determine the electrical conductivity of thin and thick films[47]. A constant current source is applied to the two outer electrodes while the floating potential is measured along the two inner electrodes. Figure 2.2 shows a schematic of the collinear four-point probes that are equally spaced on the sample surface.

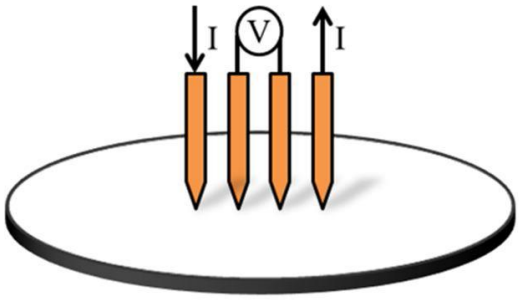

Figure 2.2: Linear four-point probe measurement set-up[47]

Equation 2-3 can be used if the film sample size is larger than the probe spacing and the film thickness is less than half the probe spacing.

$$\sigma = \frac{ln2}{\pi d}\frac{I}{V} \qquad [2\text{-}3]$$

where *d*, *I*, and *V* are the probe spacing distance, current, and voltage, respectively[47, 49]. This formula is based on the sample geometry and probe spacing.

The diameter of the probe, boundaries, and film thickness are other constraints that must be taken into consideration. For the probe distance, the diameter of the probe must be small. Furthermore, the boundary between the probes and sample surface need to be small and

hemispherical. In certain film thickness and small sample size cases, a correction factor must be applied[50-52].

Van der Pauw

The van der Pauw method is an alternative electrical conductivity measurement that can be used for film samples of an arbitrary shape[47]. Figure 2.3 shows a schematic of the van der Pauw method where the probe placement is at the corner of the samples. However, for samples of an arbitrary shape, the probes are placed along the perimeter of the sample.

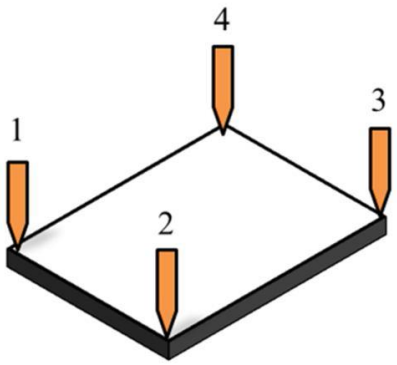

Figure 2.3: Van der Pauw measurement set-up[47]

Obtaining good electrical contact is necessary to achieve accurate results. This can be accomplished by placing indium at each probe tip or depositing metal contact by sputtering deposition. It is important that the size of the contacts are smaller than the sample size, the sample is homogeneous, and the sample thickness is uniform[53].

The van der Pauw method consists of two resistance measurements[54]. A constant current is applied between probes 1 and 2 (Figure 2.3) while the voltage is measured between probes 3 and 4 for the first measurement. The first resistance is calculated using Ohm's law: $R_{12,34}=V_{34}/I_{12}$. For the second resistance measurement, the constant current is applied between probes 2 and 3 while the voltage is measured between probes 1 and 4. Using these two resistance measurements, the sample sheet resistance R_s is calculated with equation 2-4.

$$e^{-\pi \cdot R_{12,34}/R_s} + e^{-\pi \cdot R_{23,14}/R_s} = 1 \qquad [2\text{-}4]$$

where $R_{12,34}$ is the resistance when current is passed through probes 1 and 2 and the voltage is measured through probes 3 and 4.

After the sheet resistance has been calculated, the in-plane electrical conductivity of the thin film is calculated using equation 2-5.

$$\sigma = \frac{1}{(R_S \cdot L)} \qquad [2\text{-}5]$$

where L and R_s are the sample thickness and sheet resistance, respectively.

Measurement of the Seebeck coefficient and electrical conductivity are typically straight forward and can be measured using either a custom set-up or a commercial instrument[55-58]. On the other hand, thermal conductivity measurements are the most difficult property to accurately determine. There are many losses that must be accounted for, such as convection, radiation, power loss, and thermal contacts. In addition, thermoelectric films may exhibit anisotropic thermal conductivity depending on the fabrication method. In this study, the Seebeck coefficient and electrical conductivity measurements were performed in-plane. As a result, it was necessary to determine the in-plane thermal conductivity. However, many in-plane measurement methods require thicker films, no substrates, or a high in-plane thermal conductivity. The next section discusses several thermal conductivity measurement methods used for thin films.

Thermal Conductivity

Steady-State

The steady-state method measures the thermal resistance of a sample. This can be done by measuring the temperature difference across the sample when a temperature gradient is created by a powered heater[59]. Equation 2-6 shows the calculation for the thermal conductivity k of the sample.

$$k = \frac{P}{\Delta T} \cdot \frac{L}{A} \qquad [2\text{-}6]$$

where P, ΔT, L, and A are the power supplied to the heater, temperature difference, length between the thermocouples, and cross-sectional area of the sample.

The main difficulty associated with this method is the ability to accurately determine the amount of power going through the sample. There are many power losses that are difficult to account for, such as radiation, heat conduction, and convection. As a result, the power input does not always equal the power flowing through the sample. Although it is extremely

difficult to completely eliminate all heat losses, it is possible to try and minimize the overall loss. One way to do that is by performing the experiments in a vacuum chamber with a radiation shield to reduce the convection and radiation losses. Typically, calibration samples are measured in order to account for the total heat losses.

Parallel Thermal Conductance

The parallel thermal conductance method is a variation of the steady state technique[58, 60]. The measurement is performed in a cryostat vacuum chamber with a radiation shield placed around the sample. This helps to minimize the convection and radiation losses. Supplying power to a strain gage heater is used to create the required temperature gradient.

The thermocouples are placed a predetermined distance by using a plastic sample holder typically made using a polyimide substrate. Selecting a substrate with a low thermal conductivity helps to support the strain gage heater and thermocouples without transferring too much heat from the hot side to the cold side. A baseline thermal conductance measurement is initially taken in order to account for all background thermal conduction losses. The thermal conductance is calculated using equation 2-7.

$$C = \frac{I^2 R}{\Delta T} \qquad [2\text{-}7]$$

where I, R, and ΔT are the current supplied to the heater, the resistance of the heater, and the temperature difference between the two thermocouples. From there the baseline thermal conductance is measured, the sample is attached with silver paste to create a good thermal contact, and the total thermal conductance is measured (Figure 2.4).

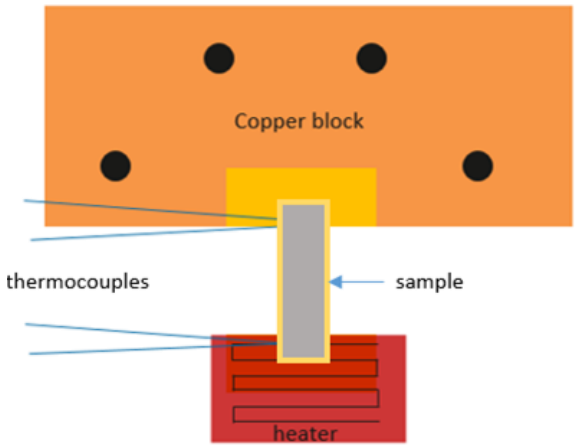

Figure 2.4: Schematic of total thermal conductance measurement set-up[48]

To determine the thermal conductance of just the sample, the baseline thermal conductance is subtracted from the total thermal conductance. After input of the sample's cross-sectional area and the length between the thermocouples, equation 2-8 is used to determine the in-plane thermal conductivity of the sample.

$$k = (C_{total} - C_{baseline}) \cdot \frac{L}{A} \qquad [2\text{-}8]$$

where C_{total}, $C_{baseline}$, L and A are the total thermal conductance, baseline thermal conductance, distance between the thermocouples, and sample cross-sectional area, respectively.

The simple sample preparation and measurement set-up requirement makes the parallel thermal conductance method the desired method to try initially. However, it should be noted that it can be more difficult to accurately measure supported films due to the heat loss through the substrate. In addition, the difficulties discussed for the steady-state method applies to the parallel thermal conductance method.

Variable-Linewidth 3ω

It can be very difficult to measure suspended thin films due to the fragility of the film. Rather than try to create suspended films, the variable line-width 3ω method can be used to measure supported films[61]. This method requires one wide thin metallic 3ω heater and one narrow thin metallic 3ω heater to be deposited onto the sample surface (Figure 2.5). The metal heaters are used as temperature sensors based on the temperature-dependent change in electrical resistance. The narrow heater creates a thermal resistance that is sensitive to the in-

plane (k_x) thermal conductivity while the wide heater provides a uniform distribution of heat through the cross-plane (k_z) thermal conductivity.

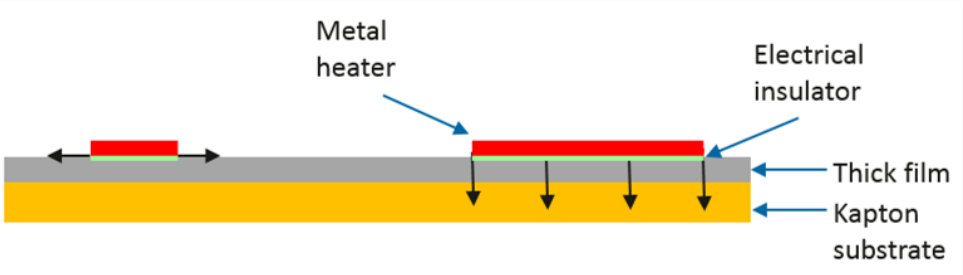

Figure 2.5: Schematic of variable-linewidth 3ω method[48]

An AC current with a modulation frequency ω is passed through the heater strip. This causes the heating power and temperature oscillation with a frequency of 2ω to be generated within the sample. Due to the temperature coefficient of electrical resistance of the heater, the temperature oscillation results in the change of the heater resistance with a frequency of 2ω. Once the current and heater resistance has been determined, the voltage with a frequency of 3ω can be calculated[62, 63]. The temperature response of the heater is measured using equation 2-9.

$$T_{2\omega} = \frac{2V_{3\omega}}{TCR \cdot V_{1\omega}} \qquad [2\text{-}9]$$

where $V_{3\omega}$, TCR, and $V_{1\omega}$ is the 3ω voltage, temperature coefficient of electrical resistance, and the amplitude of the voltage applied across the heater, respectively. Accurate measurement of the sample requires a calibration to be performed to determine the temperature coefficient of electrical resistance.

This method requires a more complicated measurement set-up than the parallel thermal conductance method; however the use of the 3ω heaters can better confine the heating region. This helps to reduce the radiation losses. However, there are still heat losses through the substrate, making the variable-linewidth 3ω in-plane thermal conductivity measurement method less sensitive than alternate suspended methods.

Transient Thermoreflectance

The transient thermoreflectance method is ideal for measuring the cross-plane thermal conductivity using an optical approach, although it is possible to perform in-plane thermal

conductivity measurements. This method utilizes a laser system that sends a known laser pulse to heat the sample. These are short optical heating pulses, which have a diameter of approximately 20 μm. By pulsing for only a few picoseconds, the heat travels to a minimum depth of 20 nm. This prevents lateral spreading of the heat or any substrate effects. The power of the pulsing laser is known and the change in surface temperature is measured using a probing laser. It is important to increase the signal-to-noise ratio; this can be done by displaying the reflected laser on a two-channel fast photodiode. The entire set-up is shown in Figure 2.6[64].

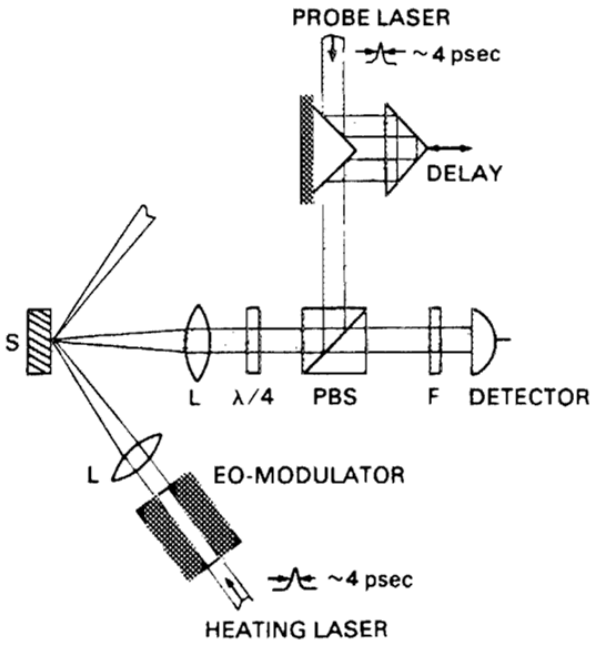

Figure 2.6: Transient thermoreflectance method[64]

The temperature is determined based on the temperature dependence of the reflectivity using equation 2-10.

$$\frac{1}{r}\frac{dr}{dT} \qquad [2\text{-}10]$$

where *r* and *T* are the reflectivity and temperature of the sample surface, respectively. Typically, 10^{-7} is the limit of systems[64, 65]. A metal coating can be applied to the sample in order to improve surface heating.

The transient thermoreflectance method is ideal for cross-plane thermal conductivity measurements, but can be more difficult in obtaining an accurate in-plane thermal conductivity value.

As can be seen, it is difficult to measure the thermal conductivity of thick and thin films. Therefore, the power factor of flexible TE films is usually published rather than the figure of merit.

2.2 Characterization Methods for Thermal Conductivity of Nuclear Materials

There are a variety of methods that can be used for measuring the thermal conductivity of nuclear materials. The process of measuring the thermal conductivity of nuclear fuels out-of-pile is less challenging. However, measuring nuclear fuels in-pile requires measurement methods that can withstand a high temperature and high radiation environment. This section discusses several thermal conductivity measurements, ranging from the bulk thermal conductivity to the local thermal conductivity.

Steady State Method

The steady state method can also be used to determine the thermal conductivity of nuclear materials. This method was previously discussed in Section 2.1.

In order to measure nuclear materials using the steady state method, a heater with a constant power must be applied to the material. In addition, it is important to know the exact distance between the thermocouples to accurately determine the temperature gradient. The main difficulty associated with this method is being able to account for power losses such as radiation, heat conduction, convection, and thermal contact resistance.

Time-Domain Thermoreflectance

Time-domain thermoreflectance (TDTR) is another pump-probe optical method that can measure the thermal conductivity. This technique is very similar to the transient thermoreflectance method. A pump pulse is used to heat the sample, however, now a time-delayed probe pulse is used to measure the temperature[66-69]. Figure 2.7 shows the typical experimental set-up.

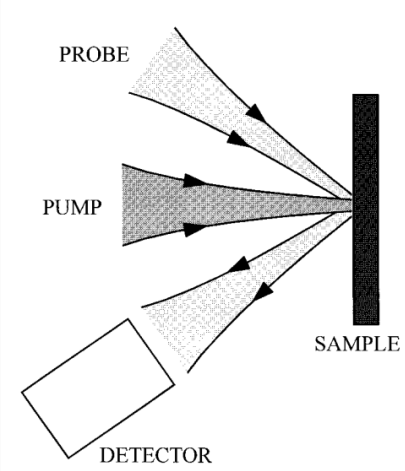

Figure 2.7: Time-domain thermoreflectance method[66]

The pump pulse heats up the sample at a small location. The optical path length from the laser source to the sample is kept constant throughout the experiment. The optical path length for the probe pulse is altered using a mechanical delay stage in order to ensure that there is a time delay between the pump and probe. A detector is used to determine the reflection coefficient based on the time delay relative to the pump pulse. The strength of the signal depends on the excitation and the amount of probe light that overlapped with the excited region. Traditional pump-and-probe techniques make it very difficult for this to be achieved since a small misalignment with the optics could completely change the location of the probe laser on the same surface. Overall, one of the biggest challenges associated with the TDTR technique is having a strong enough signal-to-noise ratio to accurately determine the thermal conductivity.

Laser Flash Analysis

Laser flash analysis (LFA) uses a laser to supply a uniform pulse of heat that is a relatively short duration compared to the amount of time the heat travels through the sample. The light pulse is absorbed by the front surface of the sample and a temperature rise occurs throughout the sample. The temperature of the rear face of the sample is recorded[70, 71]. From there, equation 2-11 can be used to determine the thermal diffusivity.

$$\alpha = 0.48L^2/\pi^2 t_{1/2} \qquad [2\text{-}11]$$

where L and t are the length of the sample and time, respectively. Once the thermal diffusivity and sample density is determined, equation 2-12 is used to calculate the thermal conductivity.

$$k = \alpha \rho c_p \qquad [2\text{-}12]$$

Where k, α, ρ, and c_p are the thermal conductivity, thermal diffusivity, density, and specific heat, respectively. Figure 2.8 shows a commercial LFA instrument. One of the issues with this technique is trying to measure reflective samples. Samples that have a high reflectivity do not absorb enough of the laser to sufficiently heat the sample. As a result, there is a minimal temperature rise detected on the rear surface of the sample.

Figure 2.8: Linseis LFA 1000[72]

Scanning Thermal Microscope

The scanning thermal microscope (SThM) technique can be used to determine the thermal conductivity and other thermal properties locally. This is done by bringing a sharp temperature-sensing tip close to the sample's surface, as shown in Figure 2.9[73]. When the tip is brought into contact with the solid sample's surface, localized heat transfer occurs, thus changing the temperature of the tip. The tip is heated by passing an electrical current through the tip, thus causing Joule heating.

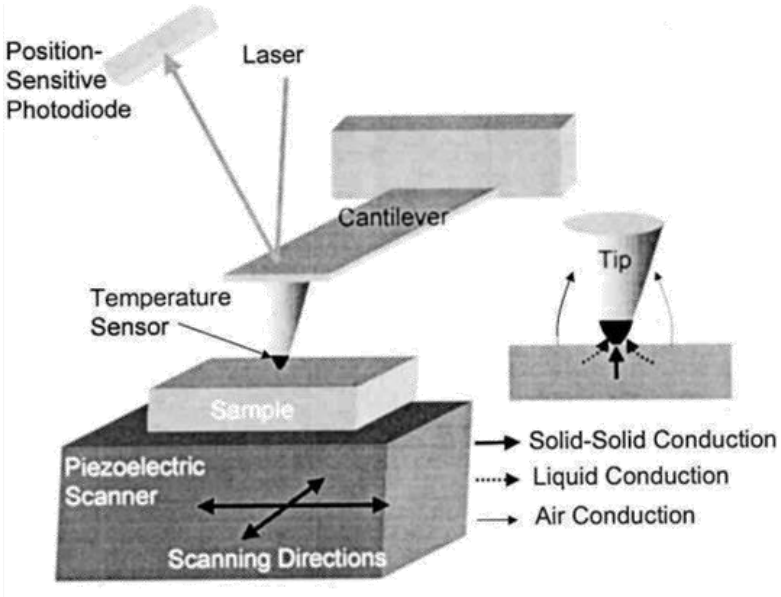

Figure 2.9: Scanning thermal microscope method[73]

The steady state heat transfer between the tip and sample can be modelled using a thermal resistance network, as shown in Figure 2.10. This thermal resistance network uses three temperatures, the temperature of the probe T_{tip}, the temperature of the sample's surface $T_{s,}$ and the temperature of the sample bulk T_{∞}. R_c is the thermal contact resistance between the tip and sample and R_s is the thermal resistance through the sample.

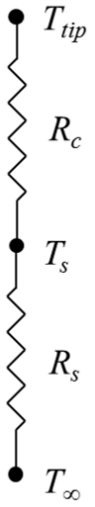

Figure 2.10: Resistor network of scanning thermal microscope method

The tip's temperature coefficient of resistance is known. This is used to relate the tip's temperature based on the electrical resistance measurement. A model or a calibration curve

that uses reference samples with known thermal conductivities can be used in order to determine the sample's thermal conductivity.

This is an ideal measurement method for samples that have nanoscale features, such as carbon nanotubes. Rather than focus on the global thermal conductivity values of a sample, the local thermal conductivity values are determined.

Transient Needle Probe

The transient needle probe method utilizes a line heat source that is embedded into the sample in order to determine the thermal conductivity, as shown in Figure 2.11. The probe consists of a heater and a thermocouple. When the sample is at thermal equilibrium, constant power is supplied to the heater and the thermocouple records the sample's temperature response[40, 74-77].

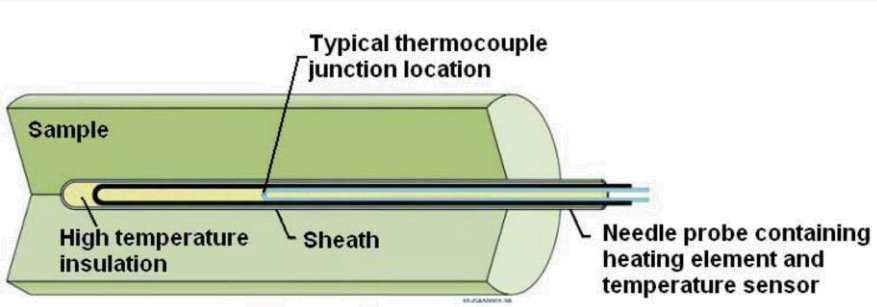

Figure 2.11: Schematic of needle probe measurement[40]

From there, the thermal conductivity is calculated from the transient temperature rise of the sample based on the linear slope of the temperature versus natural logarithm of time and equation 2-13.

$$k = \frac{CQ}{4\pi LS} \qquad [2\text{-}13]$$

where *k*, *C*, *Q*, *L*, and *S* are the thermal conductivity, calibration factor, power dissipated by the heater, heater length, and slope of the linear portion of the transient response. Since this is a transient method, the accuracy of the thermal conductivity is dependent on the linearity of the slope.

In order to perform in-pile measurements, the needle probe must be able to withstand a high temperature and high radiation environment. Commercially-available thermocouples

drift due to high temperature degradation (above 1100^{o}C). The Idaho National Laboratory (INL) has developed a High Temperature Irradiation Resistant Thermocouple (HTIR-TC) which consists of commercially-available doped molybdenum paired with a niobium alloy[77]. HTIR-TCs have demonstrated long duration performance and long-term testing at 1200^{o}C to 1800^{o}C temperatures for up to 6 months. While Type K and N thermocouples drifted by over 100^{o}C or 8%, INL's HTIR-TCs demonstrated a much smaller drift of 20^{o}C or 2%[77]. As a result, INL has developed a custom needle probe utilizing a HTIR-TC.

This method is based on the theory of an infinite line heat source embedded within a semi-infinite solid. However, nuclear samples have a radius of 5 mm. Therefore, for the semi-infinite solid assumption to remain true, the heat from the probe cannot travel all the way to the outer surface of the nuclear sample. Otherwise, boundary effects begin to reduce the accuracy in the thermal conductivity measurements.

Initial experiments indicate that the heat begins to reach the outer surface within 20 seconds. This creates an issue since the accuracy of thermal conductivity measurements rely on the linearity of the transient response. Typically, the longer the heater is powered, the more linear the transient response will be. With the limitation of 20 seconds, it is necessary to gain a better understanding of the needle probe's sensitivity to various parameters. This study will focus on understanding the needle probe parameters that influence the accuracy of the thermal conductivity.

2.3 Modelling the Needle Probe Method

In order to better understand the influence of various needle probe parameters, a model must be created. This section will include a literature review and the development of the model.

Literature Review

The needle probe measurement method consists of a line heat source. In order to create an analytical model, the problem must be defined and the assumptions must be identified.

The purpose of the model is to compare the results to experimental results. The experimental set-up will consist of the needle probe inserted into the centerline of a

cylindrical sample with a radius of 5 mm. Thermal grease may be applied at times to minimize the thermal contact resistance between the probe and sample. Figure 2.12 shows a schematic of the needle probe, thermal cement, and sample.

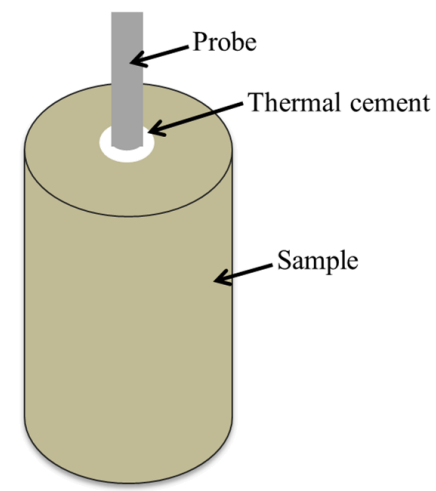

Figure 2.12: Schematic of needle probe-thermal cement-sample system

It is desired to calculate the thermal conductivity of the sample material. It is assumed that the heat flow will be transient and one-dimensional in the radial direction. The boundary conditions are a constant heat flux at the centerline and a known temperature at the outer surface. The initial condition is that everything is at thermal equilibrium when time is at 0 seconds.

A literature review was performed to determine if models have already been developed for this 1-D radial, transient heat problem. It was found that ground heat exchangers from the geoscience field apply closely to this problem. The ground heat exchanger has excess heat that it is trying to dissipate into the soil. Since ground heat exchangers are cylindrical pipes, these can be thought of as the needle probe. The soil is essentially the nuclear sample. In some cases, backfill is used to provide good thermal contact between the pipe and soil, which is similar to the thermal grease.

Ground heat exchangers are designed to be used for several decades. Therefore, a lot of literature works to develop the change in temperature for much longer times. Some of the shortest time responses that were modelled were a number of days or a few minutes[78-80]. Other models only focus on the temperature distribution of just the probe or just the thermal

cement[81-83]. Overall, most publications addressed the difficulty of solving this problem due to the transient restriction and complexity of the boundary conditions. As a result, they turned to finite difference and numerical solutions[78, 80, 84].

There was one publication, written by Gu, that modelled the same situation and boundary conditions as this dissertation study[85]. The purpose of this publication was to develop a dimensionless solution for a constant cylindrical heat source for a medium composed of backfill and soil. The basic heat conduction equation was put into non-dimensional form. The orthogonal expansion technique consisting of eigenvalues and eigenfunctions was used to solve for the temperature distribution. Bandyopadhyay *et al* state that Gu's approach has experienced disagreement in the community of heat conduction researchers[86-88].

Time was spent during this dissertation study in developing Gu's model using MATLAB. I found Gu's approach to be troublesome and to have errors. Bandyopadhyay also developed a MATLAB program and found "Gu and O'Neal's approach problematic"[86]. As a result, an alternative approach using the thermal quadrupoles method was used for this study.

Quadrupoles Method

The thermal quadrupoles method is an exact explicit method that represents a linear system. This method can be used to determine the temperature field in multilayered materials using direct solutions to the heat diffusion equation. Essentially, 2x2 matrices are used to relate the transform of temperature and flux on one surface of a medium to the other surface[89]. In order to use this method, the temperature and flux are converted into a Laplace transform into the transient 1-D case. The formulation using the thermal quadrupoles method for a double layer, 1-D, transient, plane wall case will first be presented. From there, the quadrupoles method will be applied to a double layer, 1-D, transient, cylinder.

The temperature field in a double layer, opaque, isotropic, homogeneous plane wall that is 1-D in the z direction is derived from the heat equation with a constant heat source at the inner surface (Figure 2.13). In addition, there is a thermal contact resistance between the two material layers and convection on the outer surface of layer 2.

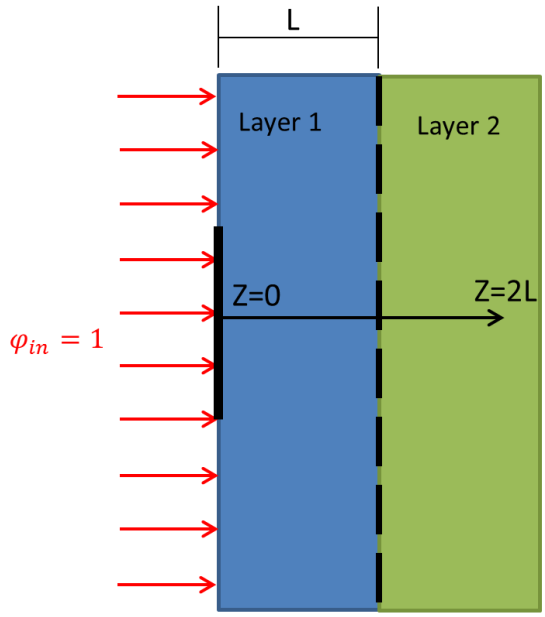

Figure 2.13: Schematic of double layer, opaque, isotropic, homogenous plane wall with heat flux in z direction

The quadrupoles derivation begins with the general solution shown in equation 2-14.

$$\frac{\partial^2 T}{\partial z^2} = \frac{1}{\alpha}\frac{\partial T}{\partial t} \qquad [2\text{-}14]$$

where *T*, *z*, *α*, and *t* are temperature, depth, thermal diffusivity, and time, respectively. A Laplace transformation is performed on the above equation and yields equation 2-15.

$$\frac{d^2\theta}{dz^2} = \frac{s}{\alpha}\theta \qquad [2\text{-}15]$$

where Θ and *s* are the Laplace transformation of temperature and the Laplace parameter, respectively.

The Laplace transformation of temperature is shown in equation 2-16.

$$\theta = K_1 \sinh(\beta z) + K_2 \cosh(\beta z) \qquad [2\text{-}16]$$

Additionally, Fourier's law relates the flux to the temperature gradient as seen in equation 2-17.

$$q'' = -k\frac{\partial T}{\partial z} \qquad [2\text{-}17]$$

where *q"* and *k* are the thermal flux and thermal conductivity, respectively. Next, a Laplace transformation must be performed on the above equation to produce equation 2-18.

$$\varphi = -k\frac{d\theta}{dz} \qquad [2\text{-}18]$$

where φ is the Laplace transformation of *q"*. From here, a derivation is performed with respect to *z* on equation 2-16 and then substituting into equation 2-18 yields:

$$\varphi = -k\beta(K_1\cosh(\beta z) + K_2\sinh(\beta z)) \qquad [2\text{-}19]$$

Θ_1 and φ_1 are then assigned as the temperature and flux boundary condition when z=0, while Θ_2 and φ_2 are the temperature and flux boundary conditions when z=L. Equation 2-19 can then be used to solve for K_1 and K_2 in terms of the boundary conditions. This results in $K_2 = \theta_1$ and $K_1 = -\frac{\varphi_1}{k\beta}$, which are then substituted into equation 2-16 and 2-19 to yield:

$$\theta = -\frac{\varphi_1}{k\beta}\sinh(\beta z) + \theta_1\cosh(\beta z) \qquad [2\text{-}20]$$

$$\varphi = -k\beta(-\frac{\varphi_1}{k\beta}\cosh(\beta z) + \theta_1\sinh(\beta z)) \qquad [2\text{-}21]$$

Next, equations 2-22 and 2-23 evaluate the Laplace transform of the temperature and heat flux at z=L:

$$\theta_2 = \theta_1\cosh(\beta L) - \frac{\varphi_1}{k\beta}\sinh(\beta L) \qquad [2\text{-}22]$$

$$\varphi_2 = -k\beta(\theta_1\sinh(\beta L) - \frac{\varphi_1}{k\beta}\cosh(\beta L)) \qquad [2\text{-}23]$$

At this point, equations 2-22 and 2-23 can be separated into inputs at surface 1 (z=0) and outputs at surface 2 (z=L) and written in matrix form:

$$\begin{bmatrix}\theta_2\\ \varphi_2\end{bmatrix} = \begin{bmatrix}\cosh(\beta L) & -\frac{\sinh(\beta L)}{k\beta}\\ -k\beta\sinh(\beta L) & \cosh(\beta L)\end{bmatrix}\begin{bmatrix}\theta_1\\ \varphi_1\end{bmatrix} \qquad [2\text{-}24]$$

The matrix can also be inverted to yield:

$$\begin{bmatrix}\theta_1\\ \varphi_1\end{bmatrix} = \begin{bmatrix}\cosh(\beta L) & \frac{\sinh(\beta L)}{k\beta}\\ k\beta\sinh(\beta L) & \cosh(\beta L)\end{bmatrix}\begin{bmatrix}\theta_2\\ \varphi_2\end{bmatrix} \qquad [2\text{-}25]$$

The following definitions are made:

$$A = D = \cosh(\beta L) \qquad [2\text{-}26]$$

$$B = \frac{\sinh(\beta L)}{k\beta} \qquad [2\text{-}27]$$

$$C = k\beta \sinh(\beta L) \qquad [2\text{-}28]$$

As a result, the following is the simplified matrix for a single layer:

$$\begin{bmatrix} \theta_1 \\ \varphi_1 \end{bmatrix} = \begin{bmatrix} A & B \\ C & D \end{bmatrix} \begin{bmatrix} \theta_2 \\ \varphi_2 \end{bmatrix} \qquad [2\text{-}29]$$

As can be seen from this process, the thermal response on the backside of a conduction layer can be found based on the boundary conditions of the front side. In addition, only two of the four boundary conditions need to be known in order to solve the system.

The same process can be applied to the second layer. This is because the backside of the first layer is the front side of the second layer. This procedure continues depending on the final number of layers. Therefore, the two layer system is represented by equation 2-30.

$$\begin{bmatrix} \theta_1 \\ \varphi_1 \end{bmatrix} = \begin{bmatrix} A & B \\ C & D \end{bmatrix}_1 \begin{bmatrix} A & B \\ C & D \end{bmatrix}_2 \begin{bmatrix} \theta_2 \\ \varphi_2 \end{bmatrix} \qquad [2\text{-}30]$$

where the subscripts represent the respective layers.

As of now, both layers have been represented with their own matrix. However, the thermal contact resistance must still be determined. Typically, the thermal contact resistance is modeled as:

$$T_1 - T_2 = R_c q'' \qquad [2\text{-}31]$$

Where R_c is the contact resistance. By performing a Laplace transformation, the above equation becomes:

$$\theta_1 - \theta_2 = R_c \varphi \qquad [2\text{-}32]$$

Placing this into matrix form:

$$\begin{bmatrix} \theta_1 \\ \varphi_1 \end{bmatrix} = \begin{bmatrix} 1 & R_c \\ 0 & 1 \end{bmatrix} \begin{bmatrix} \theta_2 \\ \varphi_2 \end{bmatrix} \qquad [2\text{-}33]$$

Finally, a matrix must be developed for the convection experienced by the outer surface of layer 2. The matrix for this situation has been discussed by Jensen and is represented by equation 2-34[90].

$$\begin{bmatrix}\theta_1\\ \varphi_1\end{bmatrix} = \begin{bmatrix}1 & 0\\ hArea & 1\end{bmatrix}\begin{bmatrix}\theta_2\\ \varphi_2\end{bmatrix} \qquad [2\text{-}34]$$

where *Area* is the surface area that is exposed to convection.

Now that matrices have been developed for the two layers, the thermal contact resistance, and convection, the entire system can be formulated. The solution to this system can be easily compiled by multiplying the matrix of each layer. Therefore, the entire system is represented by equation 2-35.

$$\begin{bmatrix}\theta_1\\ \varphi_1\end{bmatrix} = \begin{bmatrix}A & B\\ C & D\end{bmatrix}_1\begin{bmatrix}1 & R_c\\ 0 & 1\end{bmatrix}\begin{bmatrix}A & B\\ C & D\end{bmatrix}_2\begin{bmatrix}1 & 0\\ hArea & 1\end{bmatrix}\begin{bmatrix}\theta_2\\ \varphi_2\end{bmatrix} \qquad [2\text{-}35]$$

Development of Multiple-Layered Cylindrical Model

In the case of cylindrical shaped materials, the same approach as outlined above is used; however the definitions for coefficients *A, B, C,* and *D* are now different. Referring to *Thermal Quadrupoles: Solving the Heat Equation through Integral Transforms*[89] and Figure 2.14, the coefficients now become:

$$A = \alpha_2[I_0(\alpha_1)K_1(\alpha_2) + I_1(\alpha_2)K_0(\alpha_1)] \qquad [2\text{-}36]$$

$$B = \frac{1}{2\pi\lambda l}[I_0(\alpha_2)K_0(\alpha_1) - I_0(\alpha_1)K_0(\alpha_2)] \qquad [2\text{-}37]$$

$$C = 2\pi\lambda l\alpha_1\alpha_2[I_1(\alpha_2)K_1(\alpha_1) - I_1(\alpha_1)K_1(\alpha_2)] \qquad [2\text{-}38]$$

$$D = \alpha_1[I_0(\alpha_2)K_1(\alpha_1) + I_1(\alpha_1)K_0(\alpha_2)] \qquad [2\text{-}39]$$

where λ is the thermal conductivity, *l* is the length of the cylinder, *a* is the thermal diffusivity, and *p* is the Laplace parameter.

Quadrupole associated with a passive layer for three geometries. Notation: $s = e\sqrt{p/a}$; $\alpha_1 = R_1\sqrt{p/a}$; $\alpha_2 = R_2\sqrt{p/a}$; $k = \sqrt{p/a}$; $e = z_2 - z_1$ or $e = R_2 - R_1$; S: area of the plane layer; l: length of the cylindrical layer

Geometry	Rectangular	Cylindrical	Spherical
A	$cosh(s)$	$\alpha_2[I_0(\alpha_1)K_1(\alpha_2) + I_1(\alpha_2)K_0(\alpha_1)]$	$\frac{R_2}{R_1}\cosh(s) - \frac{\sinh(s)}{kR_1}$
B	$\frac{\sinh(s)}{\lambda kS}$	$\frac{1}{2\pi\lambda l}[I_0(\alpha_2)K_0(\alpha_1) - I_0(\alpha_1)K_0(\alpha_2)]$	$\frac{\sinh(s)}{4\pi\lambda k R_1 R_2}$
C	$\lambda kSsinh(s)$	$2\pi\lambda l\alpha_1\alpha_2[I_1(\alpha_2)K_1(\alpha_1) - I_1(\alpha_1)K_1(\alpha_2)]$	$4\pi\lambda R_2[\left(1 - \frac{R_1}{R_2}\right)\cosh(s) + \left(kR_1 - \frac{1}{kR_2}\right)\sinh(s)]$
D	$\cosh(s)$	$\alpha_1[I_0(\alpha_2)K_1(\alpha_1) + I_1(\alpha_1)K_0(\alpha_2)]$	$\frac{R_1}{R_2}\cosh(s) + \frac{\sinh(s)}{kR_2}$

Figure 2.14: Quadrupoles cylindrical coefficients

This study consists of a heating probe inserted into the centerline of a cylindrical sample. Figure 2.15 is a schematic of the problem. There is a thermal contact resistance between the outer surface of the needle probe and inner surface of the sample that must be considered. In addition, the outer surface of the sample is exposed to convection and should experience no heat flux. Constant power is supplied to the probe, resulting in a constant heat flux. In this case, a constant heat flux of 1 W/m^2 will be used. In addition, the heat flux occurs somewhere within the needle probe at a certain radius that is not zero.

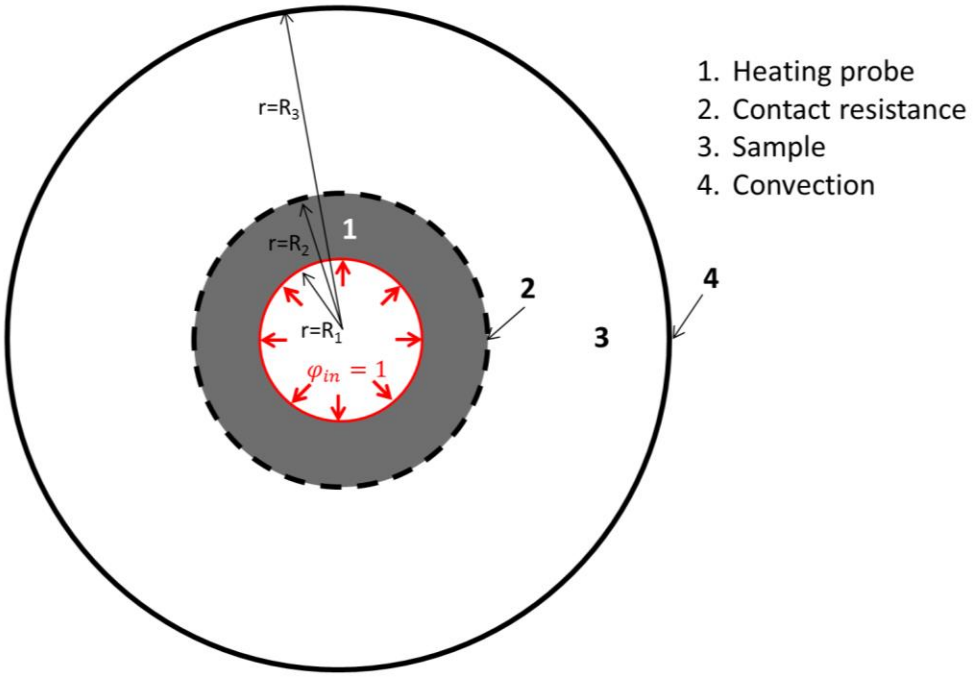

Figure 2.15: Schematic of needle probe-contact resistance-sample-convection system

Based on equations 2-36 through 2-39, a linear system can then be developed for a multiple-layered cylinder. The final matrix for the entire system becomes:

$$\begin{bmatrix}\theta_1\\ \varphi_1\end{bmatrix} = \begin{bmatrix}A & B\\ C & D\end{bmatrix}_1 \begin{bmatrix}1 & R_c\\ 0 & 1\end{bmatrix} \begin{bmatrix}A & B\\ C & D\end{bmatrix}_2 \begin{bmatrix}1 & 0\\ hArea & 1\end{bmatrix} \begin{bmatrix}\theta_2\\ \varphi_2\end{bmatrix} \qquad [2\text{-}40]$$

where the first layer, represented by the probe, uses $\alpha_1 = R_1\sqrt{p/a_1}$, $\alpha_2 = R_2\sqrt{p/a_1}$; and the second layer, represented by the sample uses $\alpha_1 = R_2\sqrt{p/a_2}$, $\alpha_2 = R_3\sqrt{p/a_2}$.

From here, equation 2-40 can be simplified to yield:

$$\begin{bmatrix}\theta_1\\ \varphi_1\end{bmatrix} = \begin{bmatrix}A & B\\ C & D\end{bmatrix} \begin{bmatrix}\theta_2\\ \varphi_2\end{bmatrix} \qquad [2\text{-}41]$$

Recognizing that φ_2=0 since there is no heat flux at the outer surface, equation 2-41 yields equations 2-42 and 2-43.

$$\theta_1 = A\theta_2 \qquad [2\text{-}42]$$

$$\theta_2 = \frac{1}{Cp} \qquad [2\text{-}43]$$

Therefore $\theta_1 = \frac{A}{Cp}$. Coefficients *A* and *C* are then expanded and a Laplace inversion is performed in order to calculate T_1. This step can be performed in MATLAB.

2.4 Results for Modelling Thermal Conductivity of Nuclear Materials

Based on the quadrupoles method, the model can be used to better understand the inner temperature v. time results of the needle probe when thermal properties and dimensions are changed for both the needle probe and sample.

Table 2-1 lists the geometries and thermal properties to model a 10 mm diameter uranium dioxide (UO_2) fuel pellet using the custom built INL needle probe.

Table 2-1: Material properties corresponding to Figure 2.16

$Radius_1$ (mm)	0.447
$Radius_2$ (mm)	1
$Radius_3$ (mm)	5
Thermal $diffusivity_1$ (m^2/s)	1.37e-05
Thermal $diffusivity_2$ (m^2/s)	6.2e-07
Thermal $conductivity_1$ (W/m·K)	42
Thermal $conductivity_2$ (W/m·K)	2.5
Probe length (m)	0.2
Contact resistance (m^2·K/W)	0.7
Convection coefficient (W/m^2·K)	13

Figure 2.16 shows that the temperature of the needle probe begins to change once the heater has been turned on. After approximately 200 seconds, the convection affects begin to dominate.

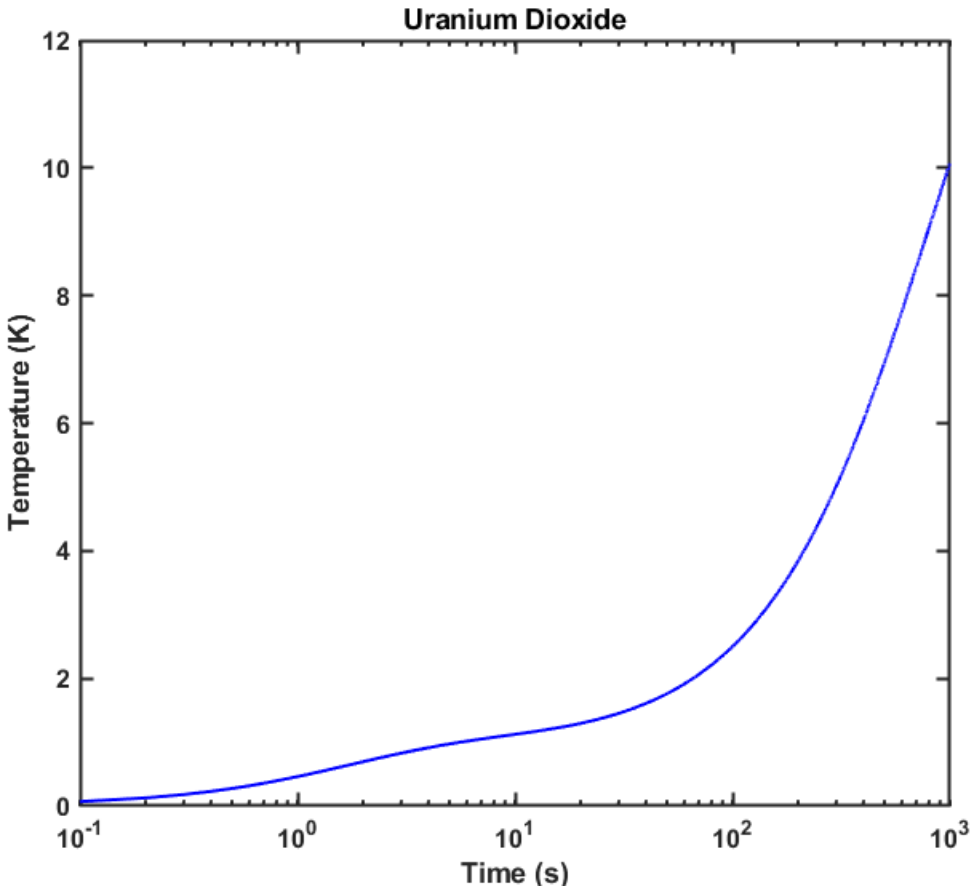

Figure 2.16: Temperature v. time plot of prototypic uranium dioxide

In addition to determining the inner temperature v. time, the quadrupoles method can also be used to determine the temperature at each interface. Figure 2.17 shows a schematic of each layer and its corresponding matrix. It is important to recognize that φ_1 is represented as a step function with a constant heat flux of 1 W/m^2. Also, the experiment is designed so no heat flux occurs at the outer surface, φ_2=0.

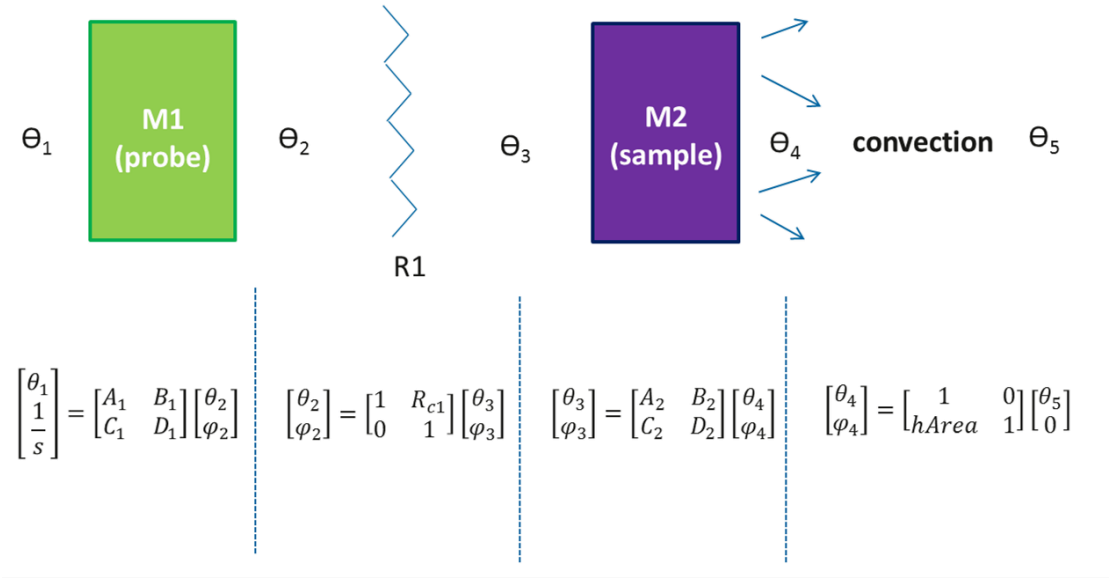

Figure 2.17: Schematic of temperature and flux at each interface

Based on these conditions, equation 2-44 is used to solve for the two unknowns, Θ_1 and Θ_5.

$$\begin{bmatrix}\theta_1\\ \frac{1}{s}\end{bmatrix} = \begin{bmatrix}A_1 & B_1\\ C_1 & D_1\end{bmatrix}\begin{bmatrix}1 & R_c\\ 0 & 1\end{bmatrix}\begin{bmatrix}A_2 & B_2\\ C_2 & D_2\end{bmatrix}\begin{bmatrix}1 & 0\\ hArea & 1\end{bmatrix}\begin{bmatrix}\theta_5\\ 0\end{bmatrix} \qquad [2\text{-}44]$$

Once Θ_1 and Θ_5 are known, the temperature and flux of any layer can be calculated. For example, to determine Θ_2 and φ_2, equation 2-45 is used.

$$\begin{bmatrix}\theta_2\\ \varphi_2\end{bmatrix} = \begin{bmatrix}1 & R_c\\ 0 & 1\end{bmatrix}\begin{bmatrix}A_2 & B_2\\ C_2 & D_2\end{bmatrix}\begin{bmatrix}1 & 0\\ hArea & 1\end{bmatrix}\begin{bmatrix}\theta_5\\ 0\end{bmatrix} \qquad [2\text{-}45]$$

This calculation process continues layer by layer until Θ_1, Θ_2, Θ_3, Θ_4, and Θ_5 are determined. From there, the temperature v. radial distance can be plotted using the geometry and thermal properties listed in Table 2-2.

.

Table 2-2: Material properties corresponding to Figure 2.18

$Radius_1$ (mm)	0.447
$Radius_2$ (mm)	1
$Radius_3$ (mm)	5
$Radius_4$ (mm)	7
Thermal $diffusivity_1$ (m^2/s)	1.37e-05
Thermal $diffusivity_2$ (m^2/s)	6.2e-07
Thermal $conductivity_1$ (W/m·K)	42
Thermal $conductivity_2$ (W/m·K)	2.5
Probe length (m)	0.2
Contact resistance (m^2·K/W)	0.7
Convection coefficient (W/m^2·K)	13

As can be seen in the temperature v. radial distance plot of Figure 2.18, there is a minimal temperature drop within the needle probe and the largest temperature drop occurs within the sample.

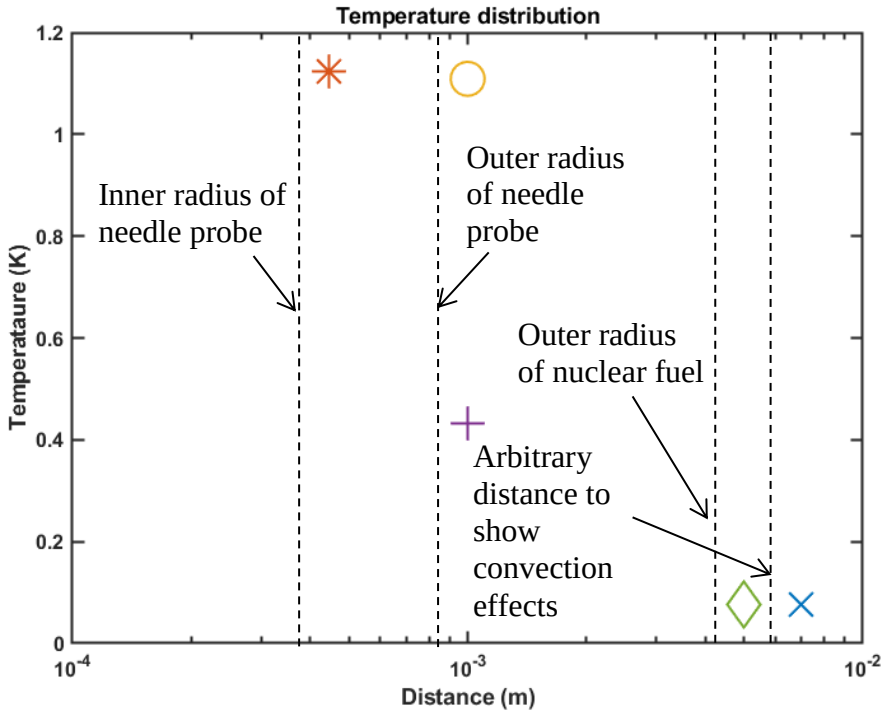

Figure 2.18: Temperature distribution through needle probe and prototypic uranium dioxide

In order to compare the MATLAB code developed using the quadrupoles method, INL created a finite element model. Figure 2.19 shows that there is good agreement between both models, further helping to validate that the MATLAB code was successfully developed.

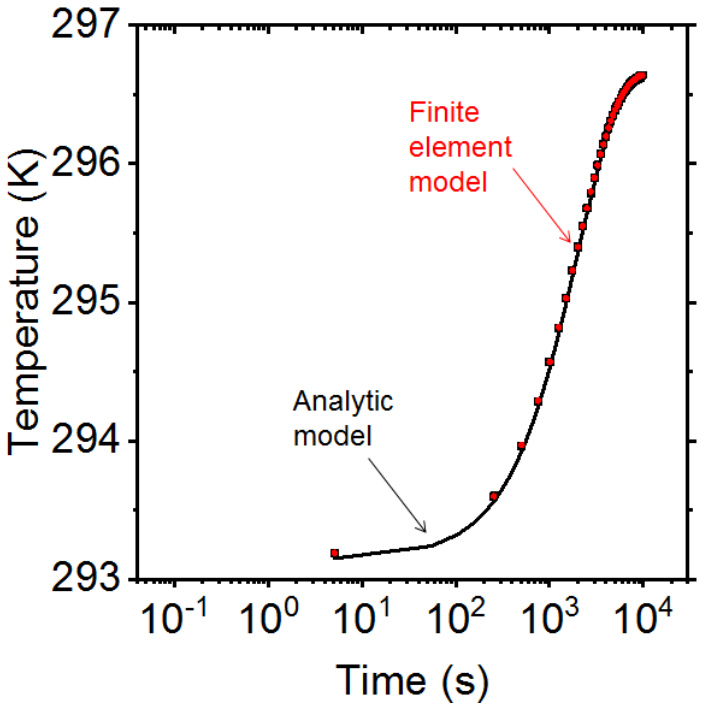

Figure 2.19: Comparison of analytic model and finite element model

The finite element models were performed using COMSOL Multiphysics. In this model, the boundary conditions and properties were defined to be the same as in the analytic quadrupoles model. The mesh was user defined with a maximum element size of 3.7e-4 m, a maximum growth rate of 1.25, and a predefined COMSOL setting of "finer" [91].

CHAPTER 3: FLEXIBLE BISMUTH TELLURIDE THIN FILM HIGH-PERFORMANCE FLEXIBLE BISMUTH TELLURIDE THIN FILM FROM SOLUTION PROCESSED COLLOIDAL NANOPLATES

Courtney Hollar, Zhaoyang Lin, Madhusudan Kongara, Tony Varghese, Chinnathambi Karthik, Jesse Schimpf, Paul H. Davis, Yaqiao Wu, Xiangfeng Duan, Yanliang Zhang, and David Estrada

3.1 Abstract

Thermoelectric generators are an environmentally-friendly and reliable solid-state energy conversion technology. Flexible and low-cost thermoelectric generators are especially attractive to power flexible electronics and sensors using body heat or other ambient heat sources. Bismuth telluride based thermoelectric materials exhibit their best performance near room temperature and are an ideal candidate to power wearable electronics and sensors using low-temperature heat sources such as body heat. Here, we report Bi_2Te_3 thin films deposited on a flexible polyimide substrate using low-cost and scalable manufacturing methods. The synthesized Bi_2Te_3 nanocrystals have a thickness of 35 ± 15 nm and a lateral dimension of 692 ± 186 nm. Thin films fabricated from these nanocrystals exhibit a peak power factor of 0.35 $mW/m \cdot K^2$ at 433 K, which is among the highest reported values for flexible thermoelectric films. In order to evaluate the flexibility of the thin films, static and dynamic bend tests were performed while monitoring the change in electrical resistivity. After 1000 bending cycles, the change in electrical resistance of the film was 23%. We also demonstrated the aerosol jet printing of our Bi_2Te_3 solutions, highlighting the potential of using additive manufacturing techniques for printing flexible thermoelectric thin films.

3.2 Introduction

The explosive market growth for self-powered wearable electronics has amplified attention on thermoelectric generators[92]. In a Markets and Markets report, it is estimated that the wearable electronic market will reach $51.6 billion by the year 2022[93]. A particularly interesting application is utilizing wearable biomedical devices to monitor physiological

signals and transmit data wirelessly, such as electrocardiograms, blood pressure, heart rate, and oxygen saturation[94-96], all of which require external power sources for efficient operation. Lithium ion batteries, which have an energy density of 2.88×10^9 J/m^3, are a traditional power source used for wearable biomedical devices[97]. However, frequent charging is necessary and the thickness of the rigid lithium battery can limit the design and the comfort associated with a wearable and flexible device. Recent progress in flexible lithium ion batteries includes the use of carbon nanotubes, graphene, carbon cloth, and conductive paper[98] as electrode materials. Flexible lithium batteries[99] have demonstrated an energy density of 388.8 J/g. Alternative power sources include electromagnetic and electrostatic sources. Both electromagnetic and electrostatic power sources convert mechanical vibrations to electrical energy[10, 11, 15, 100]. A power density of 307 μW/m^3 has been reported for electromagnetic sources[12] while 5.8×10^7 μW/m^3 can be produced for electrostatic sources[101]. However, continual mechanical vibrations are required to create a steady source of energy, thus when the user stops moving, the power source is no longer generating power.

Thermoelectric generators (TEGs) have received attention as an alternative power source due to the solid-state conversion between heat and electricity. As a result, TEGs can be powered independently of movement, making them ideal for power generation during limited mobility applications. Recently, TEGs have been used for biological applications and shown to produce power in the 14.4 μW to 11.4 mW range[23, 102], with up to 500 μW to 700 μW during an increase in physical activity[25, 103, 104]. TEGs can also be manufactured in a flexible form factor (f-TEGs) and used independently or in combination with flexible lithium-ion batteries in order to prolong battery life. Flexible TEGs can be applied to irregular surfaces and conform to skin in order to take advantage of the highest temperature gradient within the human body[23]. Therefore, f-TEGs could provide an ideal power source to address the fast growing market for wearable devices[92, 105].

The thermoelectric material efficiency is determined by the figure of merit, $ZT = S^2\sigma T/k$, where S, σ, k, and T are the Seebeck coefficient, electrical conductivity, thermal conductivity, and absolute temperature, respectively[106, 107]. The numerator, $S^2\sigma$, is referred to as the power factor. In order to obtain a high efficiency thermoelectric material, the Seebeck coefficient and electrical conductivity can be increased while the thermal conductivity is

minimized. Recently, nanostructured thermoelectric materials have exhibited superior ZT as compared to their bulk counterparts. The mean free path of electrons is typically smaller than that of phonons, allowing particle size and grain boundary scattering to be used as a mechanism to engineer the σ/κ ratio in ZT[108, 109]. Despite significant ZT improvement in nanostructured thermoelectric materials, the expensive preparation and fabrication of high-performance thermoelectric materials limits their large-scale commercialization[110-112]. While extensive studies have focused on traditional rigid bulk materials, flexible thermoelectric materials that are cost effective need to be developed in order to keep up with the growing market of sensors and flexible electronics[23, 55, 92].

Bi_2Te_3-based alloys are reported to have the best thermoelectric performance near room temperature[113]. As a result, flexible thermoelectric Bi_2Te_3 devices have the potential to power wearable electronics and sensors utilizing body heat. Physical vapor deposition methods, including sputtering[114, 115], evaporation[116, 117], and electrodeposition[118-120] are common methods to fabricate flexible thermoelectric films. An alternative approach to flexible film fabrication involves wet chemistry methods such as microwave-assisted flash combustion[121-123] and solution reaction[124, 125]. Although the physical vapor deposition approach has increased in popularity, the fabrication process is time consuming and expensive. Therefore, wet chemical methods are being explored as an alternative synthesis technique that is low-cost and commercially scalable. Previous work has shown that microwave-assisted wet chemical techniques can be used to create Bi_2Te_3 nanopowders and high performance rigid TEGs[122, 123]. A power factor of 0.45 $mW/m\cdot K^2$ was demonstrated for bulk Bi_2Te_3 TEGs fabricated using the microwave-assisted wet chemical technique[121]. However, utilizing the solution reaction wet chemical technique, power factor values between 1.2 $mW/m\cdot K^2$ and 1.9 $mW/m\cdot K^2$ were achieved for bulk Bi_2Te_3[124, 125]. Although bulk Bi_2Te_3 pellets using the solution reaction wet chemical technique results in a higher power factor than the microwave-assisted technique, there is still a need for improving thin film performance. Current solution reaction thin films demonstrate 0.686 $\mu W/m\cdot K^2$ as a power factor[126].

Here, we report a high-performance flexible Bi_2Te_3 thin film prepared from a colloidal nanoplate ink, synthesized using a scalable solution reaction wet chemical technique. We

produce Bi_2Te_3 nanoplates in an ethylene glycol (EG) solvent with poly(vinyl pyrrolidone) (PVP) as the capping agent which provides considerable solubility in various solvents[127, 128] for further solution based processing and ink development. The obtained nanoplates were dispersed in isopropyl alcohol (IPA) to form an easy-to-handle solution which could be subsequently used as the ink for wet deposition techniques, such as spin coating or aerosol jet printing (AJP). Flexible Bi_2Te_3 thin films were constructed by spin coating the ink solution on a polyimide substrate, followed by thermal annealing. The peak power factor of our spin-coated flexible film was 0.35 $mW/m \cdot K^2$ at 433K, three orders of magnitude greater than previous solution reaction based thin films[126]. We also demonstrate the compatibility of our ink with AJP, a technique adopted by the aerospace[129, 130] and electronics industries[131, 132].

3.3 Results and Discussion

We have previously demonstrated that PVP and EG do not form a compact layer on the Bi_2Te_3 nanoplate, which promises a relatively clean surface and eventually leads to improved electrical properties[133]. After growth of the nanoplates in an EG solution using PVP as the surfactant and capping agent (Figure 3.1a), the nanoplates were dispersed in IPA to form an easy-to-handle and stable ink solution, which can be used to spin coat or print thin films on various substrates such as flexible polyimide. The thickness of the final thin film could be easily tuned by adjusting the ink concentration and deposition conditions.

The smooth surface of the thin film is achieved due to the compaction of small nanoplates during the spin coating process as shown in the photograph and scanning electron microscopic (SEM) image in Figure 3.1b and Figure 3.1c, respectively. The continuous film has been well sintered due to the nanoplate's geometry of a large lateral width and small thickness. The combination of the large aspect ratio and spin coating process to create the thin films results in the close compaction of nanoplates during the spin coating process[133]. From atomic force microscopy (AFM) measurements, the average thickness and width of the individual nanoplates is 35 ± 15 nm and 692 ± 186 nm, respectively. An AFM image of a representative flake is shown in Figure 3.1d with corresponding height (thickness) and width measurements indicated. Figure 3.1e and Figure 3.1f present histograms of the nanoplate height and width distributions, respectively. Interestingly, our process results in nanoplates as

thin as ~6 nm, indicating a route towards 2-dimensional Bi_2Te_3 synthesis. Individual nanoplates exhibit different morphologies, including a pristine flat morphology, a screw – dislocation in the center of the flake as indicated by a triangular growth region, and a coarse morphology with rough edges and pores (Figure A.1, Supporting Information).

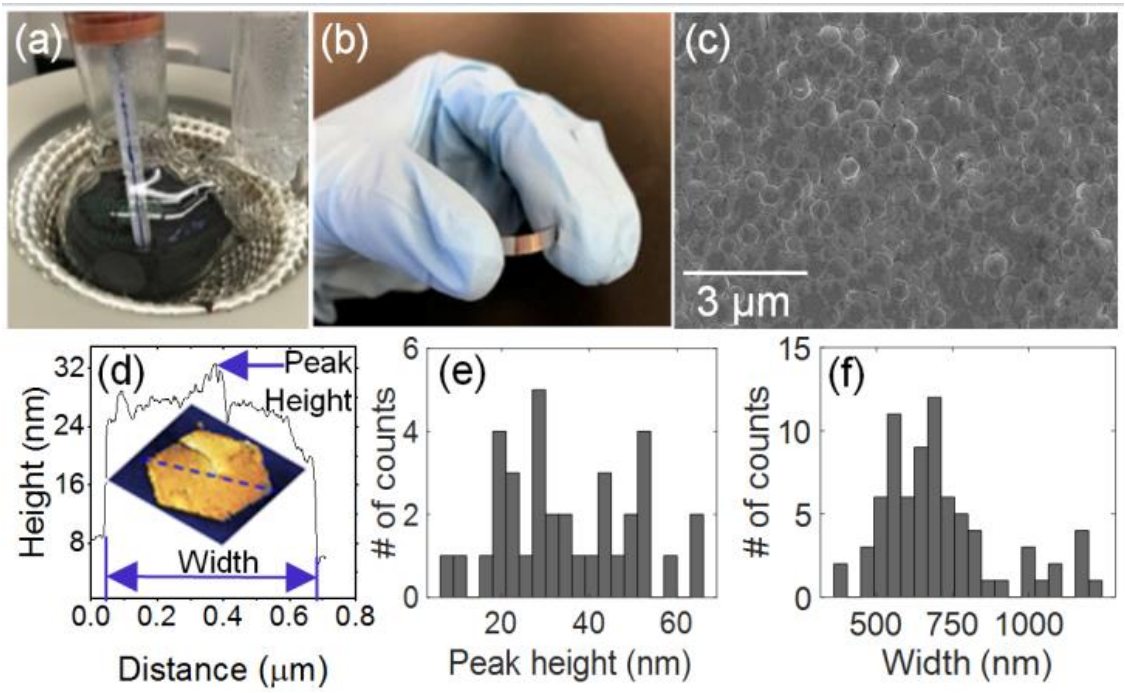

Figure 3.1: (a) Optical image of wet chemistry ink synthesis, (b) optical of spin coated Bi_2Te_3 thin film on polyimide substrate, (c) SEM image of compaction of Bi_2Te_3 nanoplates resulting from the spin coating process, (d) height v. distance plot of a representative Bi_2Te_3 nanoplate and AFM image of corresponding hexagonal nanoplate with blue dotted line indicating the cross-section measured across, (e) histogram of nanoplate peak height distribution, (f) histogram of nanoplate width distribution.

Layered Bi_2Te_3 has a rhombohedral crystal structure in the space group of D_{3d}^5 – R(-3)m with a large unit cell (~ 3 nm along *c* axis) consisting of 15 layers of atoms, which are divided into three quintuple layers[134, 135]. Transmission electron microscopy (TEM) was used to study the size, morphology and crystal structure of our Bi_2Te_3 nanoplates. Figure 3.2a andFigure 3.2b show the hexagonal shape of these nanoplates with edge to edge dimensions ranging from a few hundred nanometers to the micrometer scale, in good agreement with our AFM data. Figure 3.2b shows the bright-field image of an individual nanoplate and the corresponding [0001] zone-axis selected area diffraction pattern is shown as an inset to Figure 3.2c. Electron diffraction studies indicate that these nanoplates are single crystalline and grow

preferentially along the (0001) basal planes. The orientation of the bounding edges of the nanoplate obtained from the diffraction pattern is indicated with arrows in Figure 3.2b. The lattice image shown in Figure 3.2c further confirms the highly single crystalline nature of these nanoplates. The compositional homogeneity of these nanoplates was confirmed with energy-dispersive X-ray spectroscopy (EDS) line scans (Figure A.2 and Figure A.3, Supporting Information). Figure 3.2d and Figure 3.2e show the energy filtered TEM (EFTEM) mapping of Bi-M and Te-M. This depicts the uniform distribution of these elements without any preferential segregation which is further validated by the EDS line scan performed from the center of a nanoplate to the edge as shown in Figure 3.2f. The large spikes in the Bi profile are attributed to noise during the measurement.

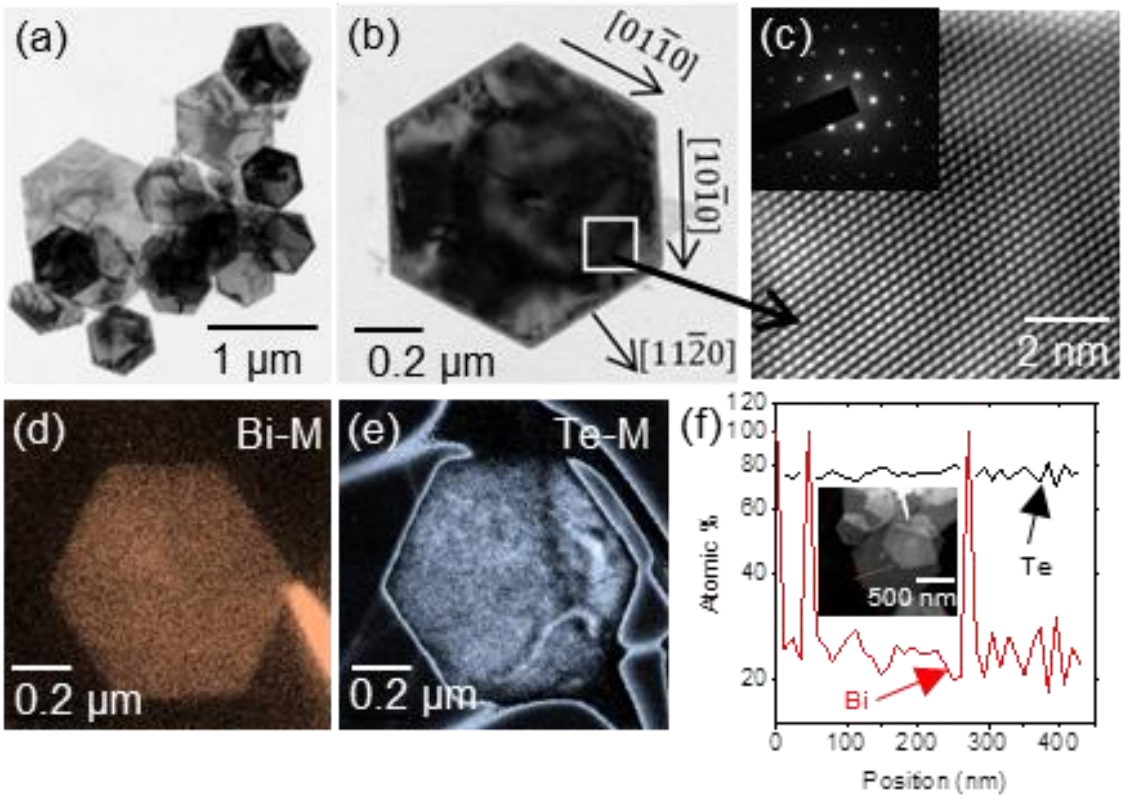

Figure 3.2: (a) Low magnification bright-field TEM micrograph of the Bi2Te3 nanoplates showing their hexagonal shape, (b) bright-field TEM image of an individual nanoplate with crystallographic orientation of the edges marked, (c) a high-resolution lattice image recorded from the nanoplate shown in (b) and the inset shows the [0001] zone axis selected area electron diffraction pattern obtained from the same nanoplate, (d) and (e) show the EFTEM imaging of Bi-M and Te-M respectively indicating their uniform distribution, (f) shows a EDS line scan of Bi and Te performed from the center of a nanoplate (inset) to the edge.

The in-plane Seebeck coefficient and electrical conductivity of spin-coated Bi_2Te_3 thin films were measured at elevated temperatures using a commercial Linseis Seebeck and resistivity instrument. Various samples with annealing temperatures ranging from 573 K to 673 K were characterized in order to determine the optimal annealing temperature. The maximum annealing temperature was limited by the melting temperature of the substrate. All samples were measured from room temperature up to 483 K in order to prevent additional annealing and undesired structural changes (Figure A.4, Supporting Information). The Seebeck coefficient first increases and then decreases with temperature, reaching a peak value at approximately 410 K. However, the electrical conductivity continues to increase with

temperature, resulting in a maximum value at 483 K. Figure 3.3a demonstrates that as the annealing temperature increases, the room-temperature electrical conductivity increases from 1.8 x 10^4 S/m to 2.9 x 10^4 S/m. The higher annealing temperature is beneficial for removing any residual PVP on the surface and enhancing the interaction between nanoplates resulting in a higher electrical conductivity for the thin film[133, 136]. Figure 3.3b shows the Seebeck coefficient first increases and then decreases with annealing temperature, and the thin film annealed at 623 K exhibits the highest Seebeck coefficient. The power factor curve shown in Figure 3.3c demonstrates an increasing trend as the temperature increases until at least 433 K due to the temperature dependence of the electrical conductivity and Seebeck coefficient. A peak power factor of 0.35 mW/m·K^2 at 433 K is obtained in the film with an optimal annealing temperature of 623 K, indicating that the thermoelectric properties can be optimized by controlling the annealing temperature. In comparison, the peak power factor of 1.9 mW/m·K^2 for a nanostructured bulk Bi_2Te_3 pellet occurs at 375 K[125] while a room temperature power factor of 0.686 μW/m·K^2 is exhibited for a Bi_2Te_3 thin film annealed at 523 K[126].

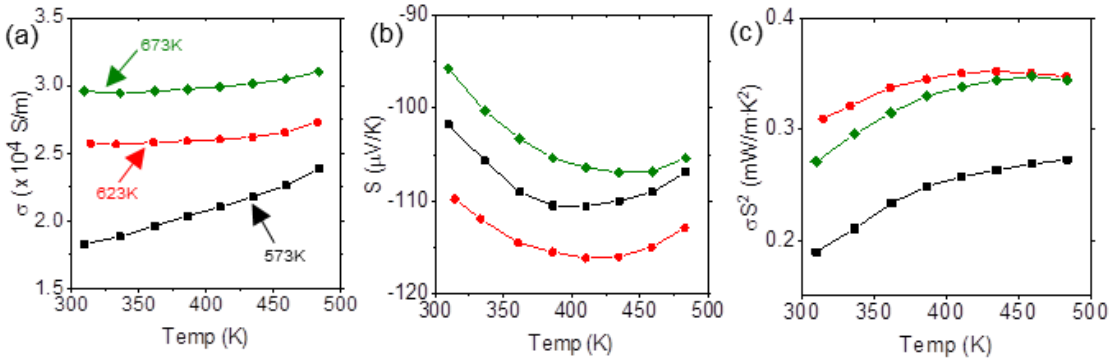

Figure 3.3: Thermoelectric performance of solution processed Bi_2Te_3 films spin coated onto a flexible polyimide substrate and annealed at various temperatures. (a) electrical conductivity *σ*, (b) Seebeck coefficient *S*, and (c) power factor σS^2.

In addition to creating thin films through spin coating, it is also possible to use AJP for thin film deposition of our colloidal inks. Figure 3.4a shows a schematic of the AJP process. During this process, Bi_2Te_3 ink is aerosolized and deposited on a polyimide substrate (Figure 3.4b). The spin coated and AJP films were evaluated for flexibility by performing room-temperature electrical resistance measurements using the van der Pauw method. The electrical

resistance was selected as the property to evaluate flexibility since cracking of the film can greatly affect the electrical resistance. Static bend tests were performed on five different radii of curvature (ROC): 10 mm, 20 mm, 30 mm, 40 mm, and 50 mm. Bending Bi_2Te_3 thin films around a 10 mm ROC resulted in the highest change in resistance of 17%, while the 50 mm ROC showed the lowest change in resistance of 5% (Figure 3.4c inset). A dynamic bend test was then performed over a 50 mm ROC (Figure 3.4c). After 100 cycles the electrical resistance of the film showed less than a 13% increase and a 23% increase after 1000 cycles. By comparison, sputtered indium tin oxide (ITO) thin films exhibited an increase in resistance of 518% after 1000 bending cycles[133]. ITO thin films are a common transparent conductor used in diverse optoelectronic devices. Bi_2Te_3 films that were screen-printed had an increase in resistance of 4.5% during a 150 bend cycles while aerosol jet printed Bi_2Te_3 showed an increased resistance of 7% for 1000 bending cycles. The smaller resistance increase for screen-printed and aerosol jet printed Bi_2Te_3 as compared to the spin coated film can be attributed to a higher film thickness. As a result, the film is more robust and is less sensitive to electrical resistance changes during bending tests. Furthermore, it is important to remember that the durability of the film may be compromised due to the relatively rough surface of the polyimide substrate and the electrode breaking during the bending tests. The flexibility performance of the Bi_2Te_3 thin films could potentially be improved with a smoother flexible substrate[137].

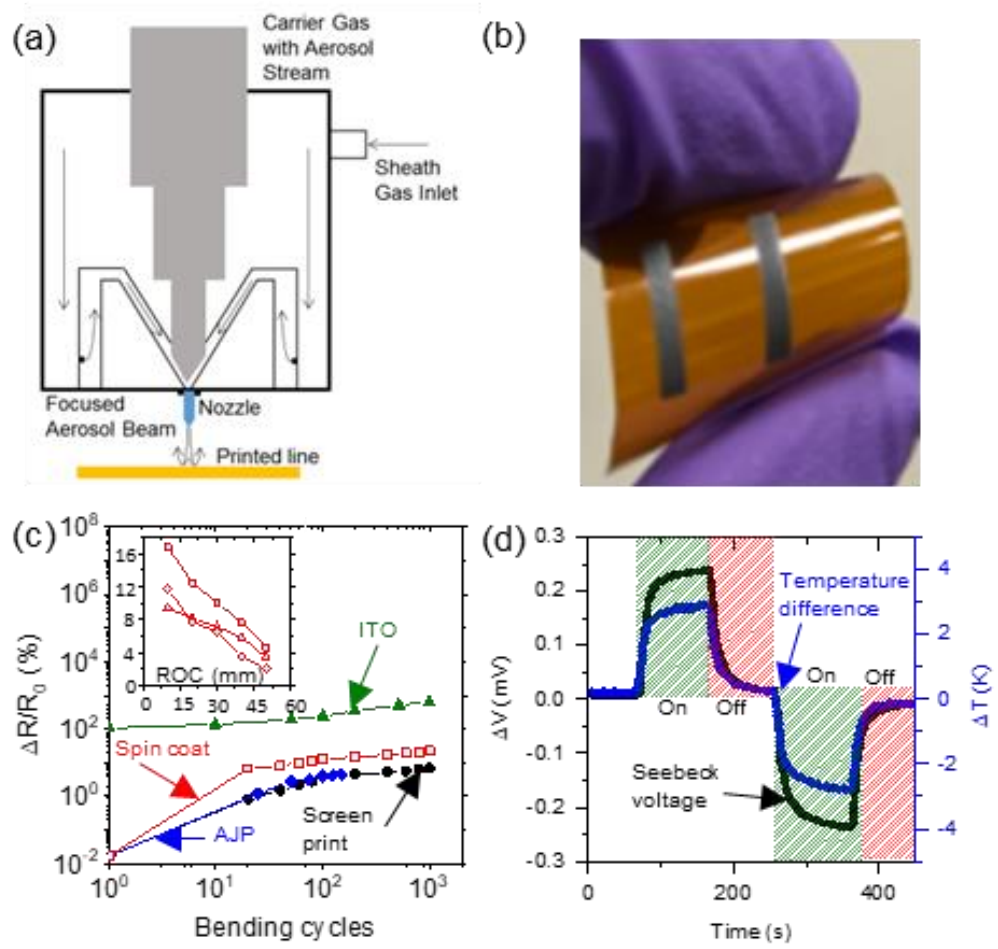

Figure 3.4: (a) Schematic of AJP process, (b) photograph of 2 mm × 10 mm AJP Bi_2Te_3 flexible films on polyimide substrate, (c) inset graph is the resistance change of several flexible films as a function of various bending radii. Resistance change of flexible film as a function of bending cycles as compared to sputtered ITO, screen printed Bi_2Te_3, and AJP Bi_2Te_3 literature values, and (d) voltage produced by a one leg AJP device using a Peltier device to mimic changes in body temperature.

The electrical conductivity of an aerosol jet printed Bi_2Te_3 film was 939.64 S/m. Meanwhile, the Seebeck coefficient was -64 μV/K. One 2 mm × 10 mm AJP film produced 0.238 mV using a Peltier device to mimic changes in human body temperature (Figure 3.4d). The decrease in electrical conductivity of aerosol jet printed films can be attributed to the increase in porosity[138], which also impacts the Seebeck coefficient. Figure 3.5a and Figure 3.5b compare the cross-sectional STEM of spin coated and AJP films, respectively (Figure A.5, Supporting Information). Spin coated films show a more layered nature to the flakes as compared to the more porous surface of AJP films. Furthermore, Figure 3.5c and Figure 3.5d

show the flake orientation for spin coated and AJP films, respectively. Due to the high aspect ratio of lateral dimensions to thickness of the nanoplates, spin coated thin films form well stacked nanoplates. This creates a large contact area which results in a reduced interface resistance and less porous film. However, similar to graphene films, AJP results in an increase in porosity due to the random stacking of nanoplates as they adhere to the polyimide substrate[138], as well as potentially trapping solvents within the printed features. The solvents evaporate leaving behind pores, thus resulting in a larger electrical resistivity. Due to the random arrangements of nanoplates and high amount of porosity, this hinders the interaction between the nanoparticles which results in a low electrical conductivity and poor Seebeck voltage. In order to further enhance the thermoelectric properties of the aerosol jet printed films, an improvement in the ink particle concentration and a compaction method is necessary to densify the film which will help reduce contact resistance and porosity.

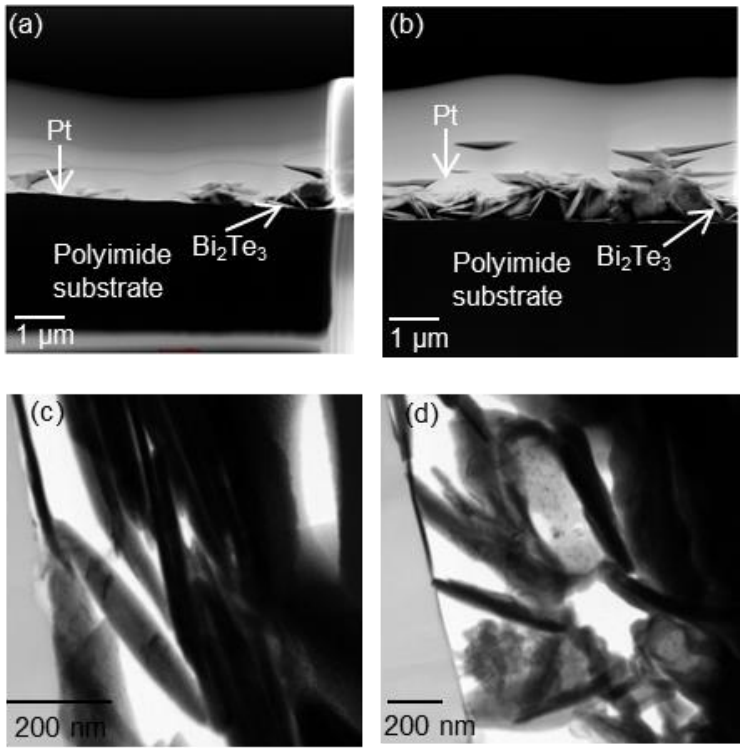

Figure 3.5: (a) cross-sectional STEM of spin coated Bi_2Te_3 film, (b) cross-sectional STEM of AJP Bi_2Te_3 film, (c) cross-sectional TEM of spin coated Bi_2Te_3 film showing flake orientation, and (d) cross-sectional TEM of AJP Bi_2Te_3 film showing flake orientation.

3.4 Conclusions

In conclusion, we have reported the high-performance flexible Bi_2Te_3 thin films fabricated from a facile ink solution obtained using a low-cost and scalable solution reaction process. The ink solution is formulated by the Bi_2Te_3 nanoplates dispersion in proper solvent, which exhibits a great potential for the practical large-scale production compared with the conventional CVD approaches or high-temperature flux methods. Bi_2Te_3 thin films annealed at 623 K exhibit a power factor of 0.35 $mW/m \cdot K^2$ at 433 K. The samples exhibited a 23% increase in electrical resistance after 1000 bending cycles. The low-cost and scalable fabrication process of Bi_2Te_3 films demonstrates the potential to power flexible electronics, sensors, and medical devices as compared to their bulk counterparts.

3.5 References

1. Bahk, J. H.; Fang, H. Y.; Yazawa, K.; Shakouri, A., Flexible thermoelectric materials and device optimization for wearable energy harvesting. *Journal of Materials Chemistry C* **2015,** *3* (40), 10362-10374.

2. Wearable technology market worth 51.60 Billion USD by 2022. https://www.marketsandmarkets.com/PressReleases/wearable-electronics.asp.

3. Haahr, R. G.; Duun, S.; Thomsen, E. V.; Hoppe, K.; Branebjerg, J. In *A wearable "electronic patch" for wireless continuous monitoring of chronically diseased patients*, 2008 5th International Summer School and Symposium on Medical Devices and Biosensors, 1-3 June 2008; 2008; pp 66-70.

4. Son, D.; Lee, J.; Qiao, S.; Ghaffari, R.; Kim, J.; Lee, J. E.; Song, C.; Kim, S. J.; Lee, D. J.; Jun, S. W.; Yang, S.; Park, M.; Shin, J.; Do, K.; Lee, M.; Kang, K.; Hwang, C. S.; Lu, N. S.; Hyeon, T.; Kim, D. H., Multifunctional wearable devices for diagnosis and therapy of movement disorders. *Nature Nanotechnology* **2014,** *9* (5), 397-404.

5. Sun, M. G.; Fernstrom, J. D.; Jia, W. Y.; Hackworth, S. A.; Yao, N.; Li, Y. C.; Li, C. L.; Fernstrom, M. H.; Sclabassi, R. J., A wearable electronic system for objective dietary assessment. *Journal of the American Dietetic Association* **2010,** *110* (1), 45-47.

6. Roundy, S.; Steingart, D.; Frechette, L.; Wright, P.; Rabaey, J. *Power Sources for Wireless Sensor Networks*, Springer Berlin Heidelberg: Berlin, Heidelberg, 2004; pp 1-17.

7. Zhou, G.; Li, F.; Cheng, H.-M., Progress in flexible lithium batteries and future prospects. *Energy & Environmental Science* **2014,** *7* (4), 1307-1338.

8. Hu, L.; Wu, H.; La Mantia, F.; Yang, Y.; Cui, Y., Thin, flexible secondary Li-ion paper batteries. *ACS Nano* **2010,** *4* (10), 5843-5848.

9. Rasouli, M.; Phee, L. S. J., Energy sources and their development for application in medical devices. *Expert Review of Medical Devices* **2010,** *7* (5), 693-709.

10. Williams, C. B.; Shearwood, C.; Harradine, M. A.; Mellor, P. H.; Birch, T. S.; Yates, R. B., Development of an electromagnetic micro-generator. *IEEE Proceedings-Circuits Devices and Systems* **2001,** *148* (6), 337-342.

11. Romero, E.; Warrington, R. O.; Neuman, M. R., Energy scavenging sources for biomedical sensors. *Physiological Measurement* **2009,** *30* (9), R35-R62.

12. Meninger, S.; Mur-Miranda, J. O.; Amirtharajah, R.; Chandrakasan, A. P.; Lang, J. H., Vibration-to-electric energy conversion. *IEEE Transactions on Very Large Scale Integration (VLSI) Systems* **2001,** *9* (1), 64-76.

13. Beeby, S. P.; Torah, R. N.; Tudor, M. J.; Glynne-Jones, P.; O'Donnell, T.; Saha, C. R.; Roy, S., A micro electromagnetic generator for vibration energy harvesting. *Journal of Micromechanics and Microengineering* **2007,** *17* (7), 1257.

14. Paracha, A. M.; Basset, P.; Marty, F.; Vaisman Chasin, A.; Poulichet, P.; Bourouina, T., A high power density electrostatic vibration-to-electric energy converter based on an in-plane overlap plate (IPOP) mechanism. DTIP 2007, Apr 2007, Stresa, lago Maggiore, Italy. TIMA Editions, pp.290-296, 2007.

15. Yang, Y.; Wei, X.-J.; Liu, J., Suitability of a thermoelectric power generator for implantable medical electronic devices. *Journal of Physics D: Applied Physics* **2007,** *40* (18), 5790.

16. Kim, S. J.; We, J. H.; Cho, B. J., A wearable thermoelectric generator fabricated on a glass fabric. *Energy & Environmental Science* **2014,** *7* (6), 1959-1965.

17. Karami, M. A.; Inman, D. J., Powering pacemakers from heartbeat vibrations using linear and nonlinear energy harvesters. *Applied Physics Letters* **2012,** *100* (4).

18. Wong, L. S. Y.; Hossain, S.; Ta, A.; Edvinsson, J.; Rivas, D. H.; Naas, H., A very low-power CMOS mixed-signal IC for implantable pacemaker applications. *IEEE Journal of Solid-State Circuits* **2004,** *39* (12), 2446-2456.

19. Leonov, V., Energy harvesting for self-powered wearable devices. *Wearable Monitoring Systems*, Springer US: Boston, MA, 2011; pp 27-49.

20. MacKenzie, J. D.; Ho, C., Perspectives on Energy Storage for Flexible Electronic Systems. *Proceedings of the IEEE* **2015,** *103* (4), 535-553.

21. Rowe, D. M., *CRC Handbook of Thermoelectrics*. CRC press: **1995**.

22. Goldsmid, H. J., *Thermoelectric Refrigeration*. Springer: **1964**.

23. Khitun, A.; Balandin, A.; Liu, J. L.; Wang, K. L., In-plane lattice thermal conductivity of a quantum-dot superlattice. *Journal of Applied Physics* **2000,** *88* (2), 696-699.

24. Scheele, M.; Oeschler, N.; Meier, K.; Kornowski, A.; Klinke, C.; Weller, H., Synthesis and thermoelectric characterization of Bi_2Te_3 nanoparticles. *Advanced Functional Materials* **2009,** *19* (21), 3476-3483.

25. Poudel, B.; Hao, Q.; Ma, Y.; Lan, Y.; Minnich, A.; Yu, B.; Yan, X.; Wang, D.; Muto, A.; Vashaee, D., High-thermoelectric performance of nanostructured bismuth antimony telluride bulk alloys. *Science* **2008,** *320* (5876), 634-638.

26. Biswas, K.; He, J.; Blum, I. D.; Wu, C.-I.; Hogan, T. P.; Seidman, D. N.; Dravid, V. P.; Kanatzidis, M. G., High-performance bulk thermoelectrics with all-scale hierarchical architectures. *Nature* **2012,** *489* (7416), 414-418.

27. Li, J.-F.; Liu, W.-S.; Zhao, L.-D.; Zhou, M., High-performance nanostructured thermoelectric materials. *NPG Asia Materials* **2010,** *2* (4), 152-158.

28. Lu, Z.; Layani, M.; Zhao, X.; Tan, L. P.; Sun, T.; Fan, S.; Yan, Q.; Magdassi, S.; Hng, H. H., Fabrication of flexible thermoelectric thin film devices by inkjet printing. *Small* **2014,** *10* (17), 3551-3554.

29. Ashalley, E.; Chen, H.; Tong, X.; Li, H.; Wang, Z. M., Bismuth telluride nanostructures: preparation, thermoelectric properties and topological insulating effect. *Frontiers of Materials Science* **2015,** *9* (2), 103-125.

30. Kusagaya, K.; Hagino, H.; Tanaka, S.; Miyazaki, K.; Takashiri, M., Structural and Thermoelectric properties of nanocrystalline bismuth telluride thin films under compressive and tensile strain. *Journal of Electronic Materials* **2015,** *44* (6), 1632-1636.

31. Zhang, J. X.; Li, Q.; Niu, P. J.; Yang, Q. X.; Tan, B. M.; Niu, X. H.; Gao, B. H., Effect of annealing temperature on microstructure and thermoelectric properties of bismuth–telluride multilayer thin films prepared by magnetron sputtering. *Materials Research Innovations* **2015,** *19* (sup10), S10-408.

32. Takashiri, M.; Kurita, K.; Hagino, H.; Tanaka, S.; Miyazaki, K., Enhanced thermoelectric properties of phase-separating bismuth selenium telluride thin films via a two-step method. *Journal of Applied Physics* **2015,** *118* (6), 065301.

33. Lin, J.-M.; Chen, Y.-C.; Lin, C.-P.; Chien, H.-C.; Wen, C.-Y.; Chang, J.-Y.; Zhan, Z.-Y., Annealing effects on the thermoelectric properties of silver-doped bismuth telluride thin films. *Microelectronic Engineering* **2015,** *148*, 51-54.

34. Kato, K.; Hatasako, Y.; Kashiwagi, M.; Hagino, H.; Adachi, C.; Miyazaki, K., Fabrication of a Flexible Bismuth Telluride Power Generation Module Using Microporous Polyimide Films as Substrates. *Journal of Electronic Materials* **2014,** *43* (6), 1733-1739.

35. Manzano, C. V.; Abad, B.; Rojo, M. M.; Koh, Y. R.; Hodson, S. L.; Martinez, A. M. L.; Xu, X.; Shakouri, A.; Sands, T. D.; Borca-Tasciuc, T., Anisotropic effects on the thermoelectric properties of highly oriented electrodeposited Bi_2Te_3 films. *Scientific Reports* **2016,** *6*, 19129.

36. Yamaguchi, M.; Yamamuro, H.; Takashiri, M., Characteristics of electrodeposited bismuth telluride thin films with different crystal growth by adjusting electrolyte temperature and concentration. *Current Applied Physics* **2018,** *18* (12), 1513-1522.

37. Kaur, H.; Sharma, L.; Singh, S.; Sivaiah, B.; Reddy, G. B.; Senguttuvan, T. D., Enhancement in figure of merit (ZT) by annealing of BiTe nanostructures synthesized by microwave-assisted flash combustion. *Journal of Electronic Materials* **2014,** *43* (6), 1782-1789.

38. Du, Y.; Cai, K. F.; Chen, S.; Cizek, P.; Lin, T., Facile preparation and thermoelectric properties of Bi_2Te_3 based alloy nanosheet/PEDOT: PSS composite films. *ACS Applied Materials & Interfaces* **2014,** *6* (8), 5735-5743.

39. Cao, Z.; Koukharenko, E.; Tudor, M. J.; Torah, R. N.; Beeby, S. P., Flexible screen printed thermoelectric generator with enhanced processes and materials. *Sensors and Actuators A: Physical* **2016,** *238*, 196-206.

40. Son, J. S.; Choi, M. K.; Han, M.-K.; Park, K.; Kim, J.-Y.; Lim, S. J.; Oh, M.; Kuk, Y.; Park, C.; Kim, S.-J., n-Type nanostructured thermoelectric materials prepared from chemically synthesized ultrathin Bi_2Te_3 nanoplates. *Nano Letters* **2012,** *12* (2), 640-647.

41. Hong, M.; Chen, Z.-G.; Yang, L.; Zou, J., Enhancing thermoelectric performance of Bi_2Te_3-based nanostructures through rational structure design. *Nanoscale* **2016,** *8* (16), 8681-8686.

42. Wang, T.; Mehta, R.; Karthik, C.; Ganesan, P. G.; Singh, B.; Jiang, W.; Ravishankar, N.; Borca-Tasciuc, T.; Ramanath, G., Microsphere bouquets of bismuth telluride nanoplates: room-temperature synthesis and thermoelectric properties. *The Journal of Physical Chemistry C* **2010,** *114* (4), 1796-1799.

43. Zhang, Y.; Hu, L. P.; Zhu, T. J.; Xie, J.; Zhao, X. B., High yield Bi2Te3 single crystal nanosheets with uniform morphology via a solvothermal synthesis. *Crystal Growth & Design* **2013,** *13* (2), 645-651.

44. Rashad, M. M.; El-Dissouky, A.; Soliman, H. M.; Elseman, A. M.; Refaat, H. M.; Ebrahim, A., Structure evaluation of bismuth telluride (Bi_2Te_3) nanoparticles with enhanced Seebeck coefficient and low thermal conductivity. *Materials Research Innovations* **2018,** *22* (6), 315-323.

45. Paulsen, J. A.; Renn, M.; Christenson, K.; Plourde, R. Printing conformal electronics on 3D structures with Aerosol Jet technology, *IEEE Proceedings of the 2012 Future of Instrumentation International Workshop (FIIW)*. **2012**, pp.1-4.

46. Noor, A. K., *Structures technology for future aerospace systems*. American Institute of Aeronautics and Astronautics: **2000**.

47. Hoey, J. M.; Reich, M. T.; Halvorsen, A.; Vaselaar, D.; Braaten, K.; Maassel, M.; Akhatov, I. S.; Ghandour, O.; Drzaic, P.; Schulz, D. L., Rapid prototyping RFID antennas using direct-write. *IEEE Transactions on Advanced Packaging* **2009,** *32* (4), 809-815.

48. Goth, C.; Putzo, S.; Franke, J. Aerosol Jet printing on rapid prototyping materials for fine pitch electronic applications, Proceedings of the IEEE 61st Electronic Components and Technology Conference (ECTC). **2011**, pp. 1211-1216.

49. Lin, Z. Y.; Chen, Y.; Yin, A. D.; He, Q. Y.; Huang, X. Q.; Xu, Y. X.; Liu, Y. A.; Zhong, X.; Huang, Y.; Duan, X. F., Solution processable colloidal nanoplates as building blocks for high-performance electronic thin films on flexible substrates. *Nano Letters* **2014,** *14* (11), 6547-6553.

50. Kong, D.; Dang, W.; Cha, J. J.; Li, H.; Meister, S.; Peng, H.; Liu, Z.; Cui, Y., Few-layer nanoplates of Bi_2Se_3 and Bi_2Te_3 with highly tunable chemical potential. *Nano Letters* **2010,** *10* (6), 2245-2250.

51. Zhang, G.; Kirk, B.; Jauregui, L. A.; Yang, H.; Xu, X.; Chen, Y. P.; Wu, Y., Rational synthesis of ultrathin n-type Bi_2Te_3 nanowires with enhanced thermoelectric properties. *Nano Letters* **2011,** *12* (1), 56-60.

52. Lin, Z.; Hollar, C.; Kang, J. S.; Yin, A.; Wang, Y.; Shiu, H. Y.; Huang, Y.; Hu, Y.; Zhang, Y.; Duan, X., A solution processable high-performance thermoelectric copper selenide thin film. *Advanced Materials* **2017,** *29* (21) 1606662.

53. Guo, Y.; Aisijiang, M.; Zhang, K.; Jiang, W.; Chen, Y.; Zheng, W.; Song, Z.; Cao, J.; Liu, Z.; Peng, H., Selective-area van der Waals epitaxy of topological insulator grid nanostructures for broadband transparent flexible electrodes. *Advanced Materials* **2013,** *25* (41), 5959-5964.

54. Pandhi, T.; Kreit, E.; Aga, R.; Fujimoto, K.; Sharbati, M. T.; Khademi, S.; Chang, A. N.; Xiong, F.; Koehne, J.; Heckman, E. M.; Estrada, D., Electrical transport and power dissipation in aerosol-jet-printed graphene interconnects. *Scientific Reports* **2018,** *8* (1), 10842.

CHAPTER 4: A PARAMETRIC STUDY FOR IN-PILE USE OF THE THERMAL CONDUCTIVITY NEEDLE PROBE USING A TRANSIENT, MULTILAYERED ANALYTIC MODEL

Courtney Hollar, Austin Fleming, Kurt Davis, Ralph Budwig, Colby Jensen, and David Estrada

4.1 Abstract

The thermal conductivity of UO_2 nuclear fuel is of high interest because of its impact on fuel temperature and the resulting reactor performance and safety considerations. The thermal conductivity of UO_2 undergoes significant changes with irradiation, and as a result is a strong function of burnup. Additionally, accurate fuel thermal conductivity measurements are of interest to aid in the development and validation of simulation codes used to predict the thermophysical properties of UO_2 under various conditions. Thermal conductivity measurements are typically made during post irradiation examination, which represents a final state of the fuel, different than exists in the test reactor due to temperature and active irradiation effects. By utilizing an in-pile measurement, thermal conductivity can be determined under prototypic conditions over a range of burnup. In this work we develop a multilayer quadrupoles analytic model to describe the transient thermal interactions between a line heat source (i.e. needle probe) and cylindrical nuclear fuel geometry for in-pile thermal conductivity measurements. A finite element analysis of the detailed needle probe geometry was compared to results from the analytic model to verify the assumptions made in the analytic model. Using the analytic model, a parameter and sensitivity study was conducted to explore the viability of accurately measuring the sample thermal conductivity under various measurement conditions. Experimentally, the needle probe was used to measure the thermal properties of polytetrafluoroethylene (PTFE) and stainless steel 304 with three different diameters (10 mm, 20 mm, and 30 mm). The analytic model was compared to the experimental measurements, which showed good agreement within 9%. Using the analytic model, three different parameters were studied for optimization: various UO_2 diameters, various probe diameters, and thermal contact resistance. The validated model and results provide the foundation to elucidate a better understanding of in-pile thermal conductivity

measurements and informs future needle probe designs to measure samples with diameters as low as 10 mm.

4.2 Introduction

Knowing the thermal conductivity of nuclear fuels can be used to increase the understanding of fuel behavior, support simulation design codes, and to develop advanced fuels. During irradiation, nuclear fuels experience a change in physical structure and chemical composition. Current thermal conductivity measurement approaches for irradiated fuels rely on post irradiation examination (PIE) approaches are challenging and are believed to not be fully representative of the state of the fuel while under irradiation in a reactor.

Most PIE methods use the laser-flash technique to determine the thermal conductivity[139-142]. In addition, some studies measure the thermal conductivity using laser-flash at elevated temperatures. However, this approach does not account for a high radiation environment. The Halden Boiling Water Reactor has performed in-pile thermal conductivity measurements by measuring the centerline temperature[143]. Although, several required assumptions to extract thermal conductivity are not always satisfied including uniform fuel composition, uniform fuel density, minimal thermal contact resistance effects, and uniform heat generation within the fuel rod. In addition, well-known heat flux and thermal hydraulic conditions are required.

The transient line source method is an alternative approach to measuring the thermal conductivity which was previously been adapted for in-pile applications[74, 75]. However, there are also challenges associated with this method. In the standard technique, the sample is assumed to be semi-infinite. Yet, prototypic light water fuels consisting of uranium dioxide (UO_2), have a diameter of approximately 10 mm. In addition, the standard technique assumes that thermal contact resistance is negligible and that the probe is infinitely thin.

Based on the transient line source method, the Idaho National Laboratory (INL) has developed an in-pile transient needle probe which can produce a temperature gradient while measuring the centerline temperature. The needle probe, based on the transient line source method, is a commonly used technique for thermal conductivity measurements. The needle probe developed by Idaho National Laboratory was adapted for high temperature operation, allowing it to be used in nuclear fuels.

This paper establishes a transient, multilayer analytic model that accurately represents the heat transfer between the needle probe, sample, and surrounding environment. This analytic model is compared to a detailed finite element model to demonstrate that the simplified geometry is representative of the needle probe. In addition, experimental results for a variety of sample materials are compared to the analytic model, all within good agreement. Using the analytic model, a sensitivity study is conducted in order to determine the influence of each parameter during the thermal conductivity measurement using the needle probe. From here, recommendations are made in order to optimize the needle probe for measurement of prototypic light water fuels.

4.3 Theory

The transient needle probe consists of a heater and a thermocouple. The probe utilizes a line heat source that is embedded into the sample in order to determine the thermal conductivity. When the sample is at thermal equilibrium, a step-function in power is supplied to the heater and the thermocouple records the sample's temperature response. The temperature response of the sample is dependent on the thermal properties and geometry. As a result, the thermal conductivity can be calculated from the temperature rise within the sample. This transient measurement method traditionally utilizes the linear region of the temperature versus the natural logarithm of time in order to determine the thermal conductivity. The linear region corresponds to a time scale in which the sample appears to be semi-infinite, thereby eliminating the dependence on sample geometry.

The needle probe method uses the theory of an infinite line heat source that is embedded in a semi-infinite solid. As a result, the thermal response is detected by a thermocouple that is located a finite distance from the heater. In this case, INL developed a probe that houses both the heater and thermocouple within one probe. The thermal conductivity is then derived using the equation according to the ASTM needle probe testing standard[144]:

$$k = \frac{Q_0}{4\pi LS}, \qquad [4.1]$$

where k, Q_o, L, and S are the thermal conductivity, power dissipated by the heater, heater length, and slope of the linear portion of the transient response, respectively. The slope of the linear region of the temperature versus the natural logarithm of time is defined as:

$$S = \frac{\partial T}{\partial\, ln(t)}, \qquad [4.2]$$

where T and t are the temperature and time, respectively.

In addition, use of the needle probe method requires an understanding of the probe and sample's Fourier number. The Fourier number is defined as:

$$Fo = \frac{\alpha t}{R^2} \qquad [4.3]$$

where α, t, and R is the thermal diffusivity, time, and characteristic length, respectively.

The probe's Fourier number was calculated based on the probe's effective thermal diffusivity, the time at which the temperature v. time curves enter the 5% linear region, and the outer radius of the probe. Based upon these calculations, the probe's Fourier number must be greater than 327 in order to allow for enough time for the heat to move out of the probe.

Furthermore, the sample's Fourier number was calculated based on the sample's thermal diffusivity, the time at which the temperature v. time curves left the 5% linear region, and the outer radius of the sample. The Fourier number of various samples including PTFE and UO_2 validates that the Fourier number is independent of individual material properties. As a result, the sample's Fourier number needs to be smaller than 0.18 in order to prevent the heat from reaching the outer surface.

This needle probe method uses the assumption of a semi-infinite sample; however nuclear fuel samples of interest are about 10 mm in diameter. A model is needed that will facilitate understanding of the impact of a finite specimen boundary condition as well as the effects of a potentially significant thermal contact resistance between the probe and sample.

A literature review was performed to determine if a 1-D radial, transient analytic model has already been developed for this scenario. One publication used the Jaeger theory to develop an analytic model, however differences between experimental data and the analytic model were observed before 500 seconds[145]. It was then discovered that ground heat

exchangers used in the geoscience field applied closely to this problem. Ground heat exchangers are cylindrical pipes that dissipate excess heat into the soil. This is analogous to the needle probe. In addition, the soil is essentially the nuclear sample while the backfill is the thermal grease. Since ground heat exchangers are designed to be used for several decades, a lot of publications developed models for much longer amounts of time. As a result, the shortest time responses were modelled for a few days or minutes[78-80]. Alternative models focused on understanding the 2-D influence[146] while others had interest in only determining the temperature distribution within the probe or within the thermal cement[81-83]. Several publications have acknowledged the difficulty of solving this problem as a result of the transient state and complex boundary conditions. Therefore, they turned to finite difference and numerical solutions[78, 80, 84].

One publication, written by Gu, developed a dimensionless solution for a constant cylindrical heat source for a medium composed of backfill and soil[85]. The basic heat conduction equation was put into non-dimensional form while the orthogonal expansion technique consisting of eigenvalues and eigenfunctions was used to solve for the temperature distribution. Bandyopadhyay *et al* stated that Gu's approach has experienced disagreement in the community of heat conduction researchers[86-88]. In this paper, the method of thermal quadrupoles was used to derive a flexible model of the needle probe and sample system.

4.4 Calculation

The theoretical model derived here is based on a two layer system, though adding additional layers is quite simple. The first layer represents probe properties and the second represents the sample with a contact resistance between the layers. Figure 4.1a shows a schematic cross-section of the needle probe inserted into the centerline of a sample. Various parts of the needle probe are included such as the outer sheath, insulation, thermocouple wires, and the heater wires. This analytic model serves as a tool to understand each parameter and its influence on the thermal conductivity accuracy. Figure 4.1b shows the geometry chosen to represent the needle probe geometry in the analytic model.

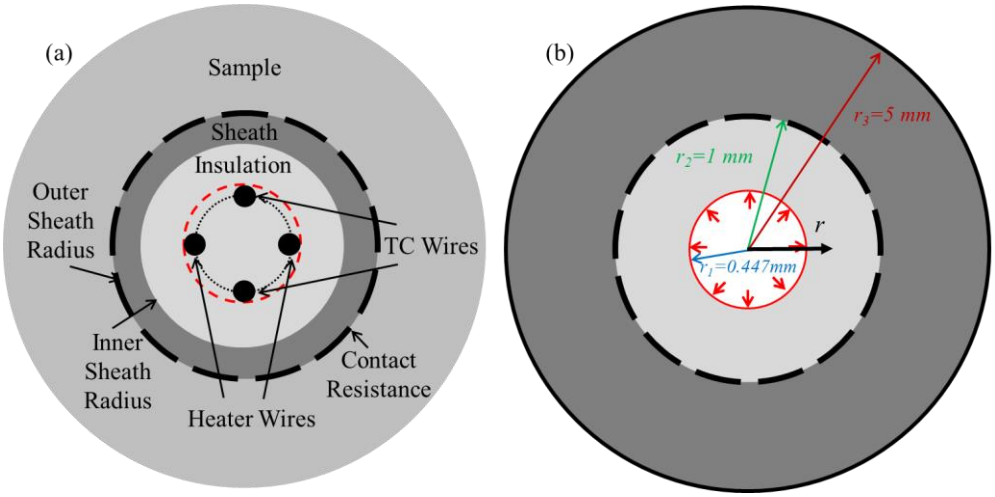

Figure 4.1: (a) Diagram of the needle probe geometry inserted into a cylindrical sample. (b) diagram of the equivalent heat transfer geometry.

To account for the influence of the sheath, insulation, thermocouple wires, and heater wires, the effective thermal capacity and thermal conductivity of the probe are accounted for using equations (4.4) and (4.5)

$$\left(\rho c_p\right)_{eff} = \frac{A_{wires}\left(\rho c_p\right)_{wires} + A_{ins}\left(\rho c_p\right)_{ins} + A_{sheath}\left(\rho c_p\right)_{sheath}}{A_{probe}} \quad [4.4]$$

$$k_{eff} = \frac{ln\left(\frac{r_1}{r_3}\right)}{\frac{ln\left(\frac{r_2}{r_1}\right)}{\left(k_{ins}\right)} + \frac{ln\left(\frac{r_3}{r_2}\right)}{\left(k_{sheath}\right)}} \quad [4.5]$$

where ρ, c_p, A, k, R_T, L, r_1, r_2, and r_3 are the density, specific heat, cross-sectional area, thermal conductivity, thermal contact resistance, length, inner radius of the probe/outer radius of the heater wires, outer radius of the probe, and outer radius of the sample, respectively.

Using these effective thermal properties, an analytical solution can be developed to model the needle probe when inserted into the centerline of a cylindrical nuclear fuel pellet. The quadrupoles method is an exact explicit method that represents a linear system[89]. This method can be used to determine the temperature field in multilayered materials using direct solutions to the heat diffusion equation. A matrix is developed for the probe, thermal contact resistance, sample, and convection. Using matrix multiplication, a solution can be easily constructed for the multilayered system. Equations (4.6) and (4.7) were used to develop the matrix system in cylindrical coordinates[89]

$$q_{1,i} = r_i\sqrt{p/\alpha_i} \qquad q_{2,i+1} = r_{i+1}\sqrt{p/\alpha_i} \tag{4.6}$$

$$A_i = q_{2,i}[I_0(q_{1,i})K_1(q_{2,i}) + I_1(q_{2,i})K_0(q_{1,i})] \tag{4.7a}$$

$$B_i = \frac{1}{2\pi kL}[I_0(q_{2,i})K_0(q_{1,i}) - I_0(q_{1,i})K_0(q_{2,i})] \tag{4.7b}$$

$$C_i = 2\pi kLq_{1,i}q_{2,i}[I_1(q_{2,1})K_1(q_{1,i}) - I_1(q_{1,i})K_1(q_{2,i})] \tag{4.7c}$$

$$D_i = q_{1,i}[I_0(q_{2,i})K_1(q_{1,i}) + I_1(q_{1,i})K_0(q_{2,i})] \tag{4.7d}$$

where *r*, *p*,*α*, *k,* and *L* are the radius of each layer, Laplace parameter, thermal diffusivity, thermal conductivity, and length of the cylinder. The subscript *i* corresponds to the layer in the model (1 being the probe, 2 being the sample).

Equation (4.8) shows the matrix representation of a one-layered cylindrical material

$$\begin{bmatrix}\theta_1\\ \phi_1\end{bmatrix} = \begin{bmatrix}A_1 & B_1\\ C_1 & D_1\end{bmatrix}\begin{bmatrix}\theta_2\\ \phi_2\end{bmatrix} \tag{4.8}$$

where Θ and φ are the Laplace temperature and Laplace heat flux, respectively.

Equation (4.9) shows the matrix representation of a thermal contact interface

$$\begin{bmatrix}\theta_1\\ \phi_1\end{bmatrix} = \begin{bmatrix}1 & R_{th}\\ 0 & 1\end{bmatrix}\begin{bmatrix}\theta_2\\ \phi_2\end{bmatrix} \tag{4.9}$$

where R_{th} is the thermal contact resistance.

Equation (4.10) represents the entire multilayered system of the needle probe-thermal contact resistance-nuclear fuel.

$$\begin{bmatrix}\theta_1\\ \phi_1\end{bmatrix} = \begin{bmatrix}A_1 & B_1\\ C_1 & D_1\end{bmatrix}\begin{bmatrix}1 & R_{th}\\ 0 & 1\end{bmatrix}\begin{bmatrix}A_2 & B_2\\ C_2 & D_2\end{bmatrix}\begin{bmatrix}1 & 0\\ h & 1\end{bmatrix}\begin{bmatrix}\theta_3\\ \phi_3\end{bmatrix} \tag{4.10}$$

The temperature response of the probe, Θ_1, can then be calculated by expanding the matrix into equation form since there are two unknowns and two equations. A Laplace inversion is then performed to transform the temperature response of the probe Θ_1 into T_1. The quadrupoles analytical solution model, hereafter called the analytic model, was compared to a finite element software model where both used the equivalent heat transfer

geometry for the probe as well as the thermal properties and geometry of a 10 mm diameter UO_2 sample. As can be seen in Figure 4.2a and Figure 4.2b, good agreement, with a standard error of 0.0039 K, was achieved which provides verification of the solution.

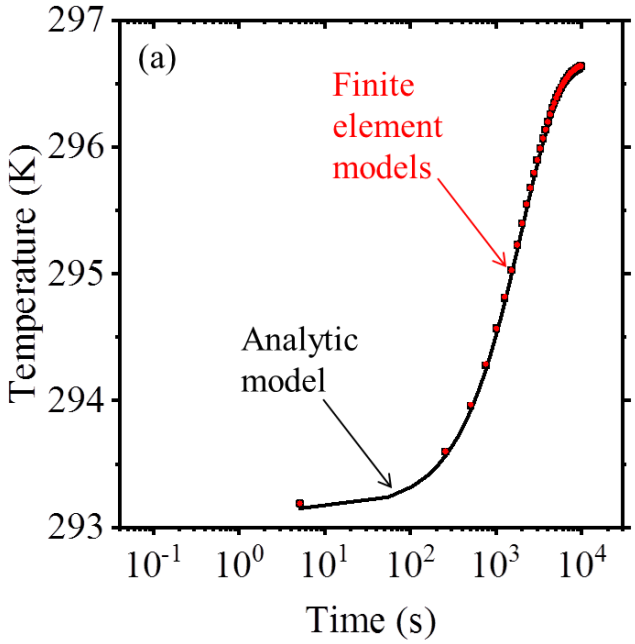

(b)

Inner probe radius (mm)	0.447
Outer probe radius (mm)	1
Sample radius (mm)	5
α_{probe} (m^2/s)	1.37e-5
k_{probe} (W/m·K)	42
α_{UO2} (m^2/s)	6.2e-7
k_{UO2} (W/m·K)	2.5
Length (m)	0.2
Contact resistance ($K \cdot m^2/W$)	1
h ($W/m^2 \cdot K$)	10
Q (W)	10

Figure 4.2: (a) Temperature v. time plot for the analytic solution based on the equivalent heat transfer geometry and finite element model using both the detailed geometry and the equivalent heat transfer geometry and thermal properties. The finite element models are dotted while the analytical model is the line. (b) Table of thermal properties and geometry of probe inserted into the centerline of a UO_2 sample.

4.5 Results and Discussion

Experimental validation of the analytical model was performed using a custom-built needle probe. The effective thermal diffusivity and thermal conductivity of the probe were calculated to be 1.37e-5 m^2/s and 42 W/m·K, respectively. The individual thermal diffusivity of the thermocouple wires, heater wires, insulation, and sheath were weighted based on volume and then summed together to result in the effective thermal diffusivity of the probe. Furthermore, the effective thermal conductivity of the probe was calculated using the thermal resistor analogy, as defined in equations 3 & 4. The uncertainty of the thermocouple within the probe was 2.2°C or 0.75%, whichever was greater. Cylindrical polytetrafluoroethylene (PTFE) and stainless steel 304 were selected as the test materials to provide a broad thermal

conductivity range of 0.25 W/m·K to 14.8 W/m·K. Furthermore, various outer diameters of 10 mm, 20 mm, and 30 mm were selected to determine the influence of the samples' outer boundaries.

A hole of 2.06 mm was pre-drilled into the centerline of the calibration materials in order for a 2.01 mm diameter needle probe to be easily inserted. Since the probe and sample were not pressure fit, the thermal contact resistance between the probe and medium were relatively large (i.e. 0.6 $K \cdot m^2/W$ to 2 $K \cdot m^2/W$). These thermal contact resistance values were adjusted to match the experimental results. Figure 4.3a shows that all three PTFE samples exhibited the same trend for the first 20 seconds. Afterwards, the boundary conditions begin to affect the 10 mm diameter sample. At approximately 200 seconds, the heat has travelled through the entire 20 mm diameter sample. The analytic model and experimental results show good agreement while the heat is travelling through the sample. Once the heat meets the outer boundary, convection begins to dominate the temperature change. Using the model to match the experimental data, the thermal diffusivity and thermal conductivity of PTFE were determined to be 1.24e-7 m^2/s and 0.25 W/m·K, respectively. This demonstrates good agreement with the literature values for PTFE, where thermal conductivity is 0.25 W/ m·K[147] and thermal diffusivity is 1.24e-7 m^2/s[148]. If the thermal conductivity were to be calculated using the slope of the linear region of the temperature versus the natural logarithm of time the 10 mm, 20 mm, and 30 mm diameter samples would exhibit linearity from 16s to 38s, 26s to161s, and 29s to 354s, respectively. This was determined by graphing the derivative of the temperature v. log(time) plot versus time (Figure 4.3b**)**. The known thermal conductivity of PTFE was then graphed which included a 5% thermal conductivity range. The 5% thermal conductivity range are the two black dashed lines within the plot that indicate $\pm$5% of the known thermal conductivity value while the solid black line is the known thermal conductivity value. The linear region of the temperature versus the natural logarithm of time was then found to be when the curve was within the 5% thermal conductivity range.

Figure 4.3a can be used to calculate the Fourier number of both the needle probe and sample. For example, at 10s, the probe's Fourier number is 137 while the Fourier number of a 30 mm diameter PTFE sample is 0.0055. Since the probe's Fourier number is not yet large enough, this indicates that the heat is still within the needle probe. However, at 30s, the Fourier number of the probe is now 411 while the 30 mm diameter PTFE sample's Fourier

number is 0.017. This indicates that the 30 mm diameter curve in Figure 4.3b is now within the linear region.

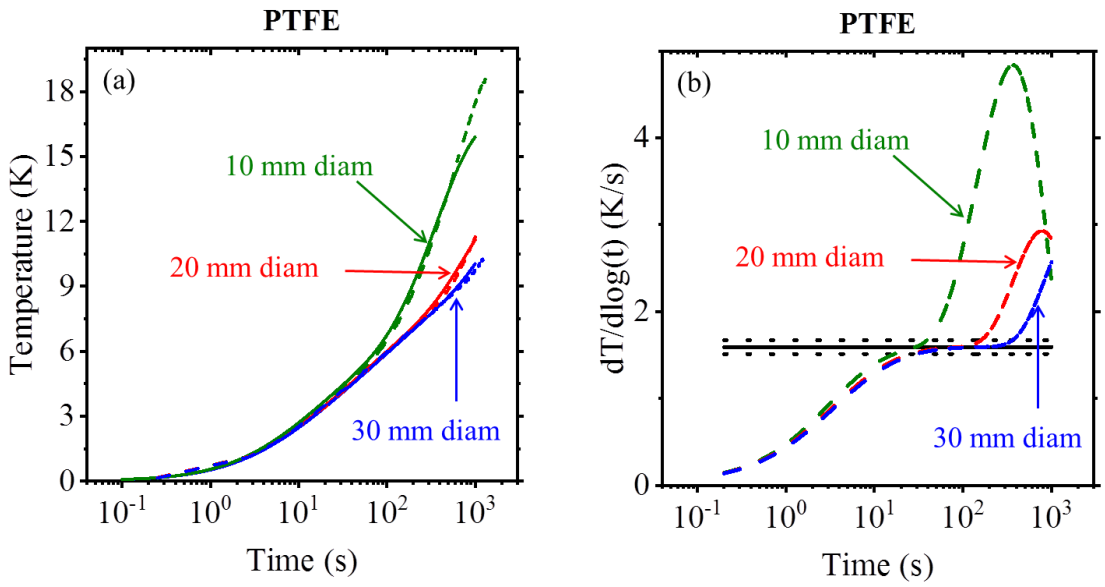

Figure 4.3: (a) Temperature v. time plot of PTFE samples with various diameters of 10 mm, 20 mm, and 30 mm. Dashed lines indicate analytical model and dotted lines indicate experimental data. (b) derivative of the temperature v. log(t) plot versus time. The ±5% of the known thermal conductivity value are the two black dashed lines while the known thermal conductivity value according to literature is the solid black line.

Using equations 4.1 and 4.2, the linear region of the transient response was given a logarithmic fit (Figure 4.4). Based on the slope of the regressed line, the thermal conductivity for the 30 mm diameter PTFE sample was calculated to be 0.26 W/ m·K, with a standard deviation of 0.0075 W/ m·K. This provides an additional validation of the quadrupole model approach.

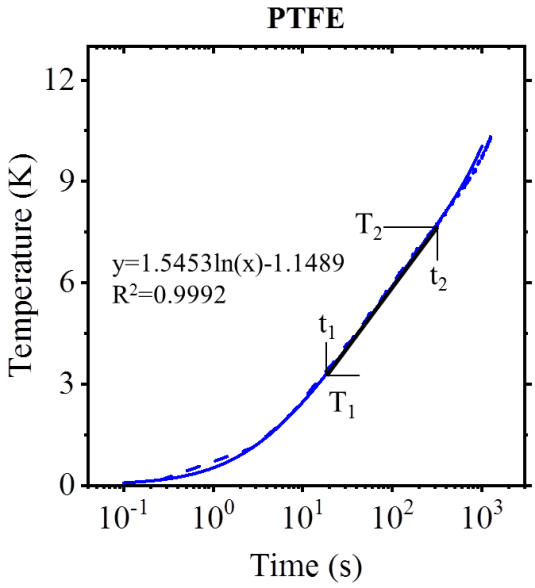

Figure 4.4: Temperature v. time plot of 30 mm diameter PTFE sample including linear regression to determine thermal conductivity

Similar experiments were also performed on stainless steel 304 samples, as shown in Figure 4.5. As a result of the higher thermal conductivity as compared to the PTFE, the heat travelled faster to the outer surface. Furthermore, the thermal contact resistance for the stainless steel 304 samples ranged between 1.35 K·m^2/W to 2 K·m^2/W. As a result of the relatively large thermal contact resistance, it can be seen that from 3s to 10s there is an additional curve which does not occur in the PTFE measurements. Regardless, the analytical model is able to exhibit good agreement with the experimental results. The thermal diffusivity and thermal conductivity as determined using the analytical model was 3.8e-6 m^2/s and 14.8 W/m·K, respectively. This shows good agreement with stainless steel 304 literature values for a thermal conductivity of 14.34 W/m·K[149] and a thermal diffusivity of 3.75e-6 m^2/s[150]. In this case, trying to determine the thermal conductivity using the slope of the linear region of the temperature versus the natural logarithm of time would not be possible as none of these curves enter the 5% thermal conductivity region (Figure 4.5b). Therefore, this demonstrates the quadrupoles model can be used to determine the thermal conductivity of samples that would not typically be accurately measured using the traditional transient line source method. In addition to accurately extracting the correct thermal properties for the sample, the model accurately predicts the temperature response in the time scales in which the sample is not

semi-infinite. Specifically, in the short time scales, which is dominated by the probe properties, and the long time scales which is influenced by the boundary conditions and sample radius.

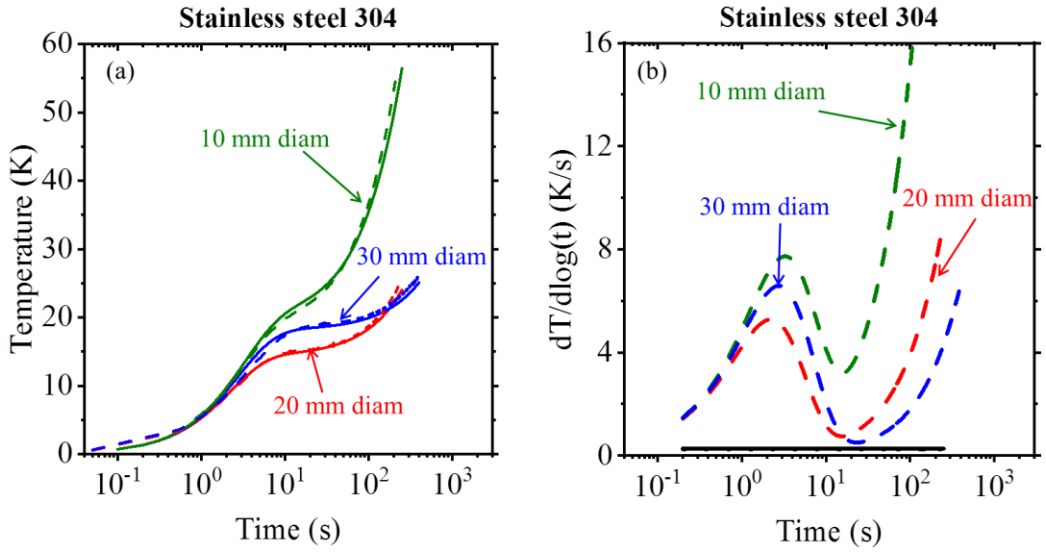

Figure 4.5: Temperature v. time plot of stainless steel 304 samples with various diameters of 10 mm, 20 mm, and 30 mm. Dashed lines indicate analytical model and dotted lines indicate experimental data. (b) derivative of the temperature v. log(t) plot versus time.

In order to further understand the influence of the thermal contact resistance, experiments were performed on the stainless steel 304 samples with thermal grease. Figure 4.6 shows the influence of the thermal contact resistance on 10 mm, 20 mm, and 30 mm diameter stainless steel 304 samples. The use of thermal grease significantly reduced the thermal contact resistance from an average of 1.68 $K \cdot m^2/W$ to 0.53 $K \cdot m^2/W$. Furthermore, this demonstrates that the quadrupoles model shows good agreement with the experimental results for a range of thermal conductivity values and thermal contact resistances.

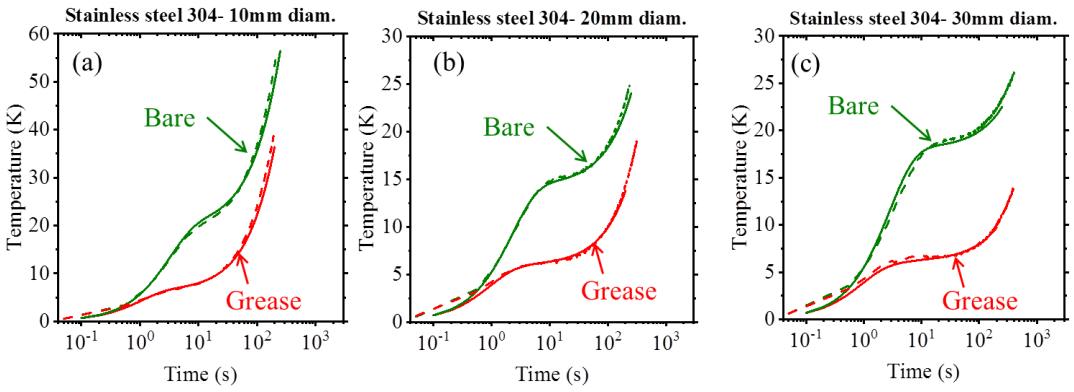

Figure 4.6: Temperature v. time plot comparing bare needle probe and thermal greased needle probe for stainless steel 304 samples with a diameter of (a) 10 mm, (b) 20 mm, and (c) 30 mm. Dashed lines indicate analytical model and dotted lines indicate experimental data.

The convection coefficient used in the model was experimentally determined for the stainless steel 304 samples and calculated using the lumped capacitance equation:

$$h = -\frac{\rho V c t}{A_s} \ln\left(\frac{T - T_\infty}{T_i - T_\infty}\right) \qquad [4.11]$$

Where h, ρ, V, c, t, A_s, T, T_∞, and T_i are the convection coefficient, density, volume, specific heat, time, surface area, temperature, ambient temperature, and initial temperature. Good agreement between the convection coefficient and experimental results further validated the use of 10 $W/m^{2}K$.

Based on the verification and validation, a sensitivity parameter study using the analytic model was then performed in order to determine how each parameter influenced the thermal conductivity measurement using the needle probe. As a baseline condition, sample properties for UO_2 were used. The parameters that were varied in this study include thermal contact resistance, probe radius, sample radius, probe thermal conductivity, sample thermal conductivity, convection, and various combinations of the probe's thermal properties. The data reduction technique to determine the thermal conductivity using the needle probe relies on the slope of the T v. log(t) plot, therefore the sensitivity of this slope is of more interest rather than the sensitivity of the temperature. Each parameter was adjusted by 5% of its original value and the percentage of relative change of dT/dlog(t) was used to determine the sensitivity.

Figure 4.7 shows for the measurement of a UO_2 sample with a 10 mm diameter, the probe thermal conductivity and probe radius are initially the most sensitive. For example, at 0.3 s, there is a relative slope change of 9.7% and 4.0% for the probe radius and probe thermal conductivity, respectively. This can be attributed to the thermal response of the probe. However, change in the heat capacity results in a negligible relative slope change. Shortly after the heat begins to travel from the probe to the sample, the thermal contact resistance becomes more sensitive. From there, the sample's radius and thermal conductivity dominate after 10 seconds until the convective losses influence the result.

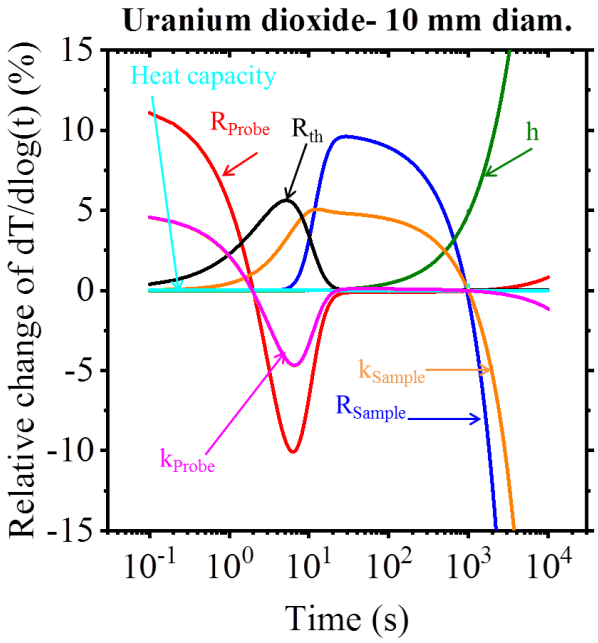

Figure 4.7: Relative change v. time plot for 10 mm diameter UO_2 sample comparing probe radius (R_{probe}), thermal conductivity of probe (k_{probe}), thermal contact resistance (R_{th}), sample radius (R_{sample}), thermal conductivity of sample (k_{sample}), convection (h), and various probe thermal properties.

The UO_2 diameter was then increased to 40 mm to see if the sample's thermal conductivity could be isolated to enhance sensitivity during measurements. Figure 4.8 shows the probe's thermal response is still the most sensitive initially. As the heat begins to move outward from the probe to the sample the thermal contact resistance increases in sensitivity. The heat continues to travel through the sample and the sample's radius and thermal conductivity become more sensitive between 10 to 2000 seconds. This becomes the ideal measurement region because the response of the sample's thermal conductivity and radius are

more sensitive compared to other parameters. Furthermore, the sample's radius can be accurately determined, which allows for calculation of the sample's thermal conductivity. Therefore, a sample with a diameter greater than 40 mm is sufficient in order to optimize the measurement region by isolating the sample's thermal conductivity sensitivity while other parameters exhibit a low sensitivity.

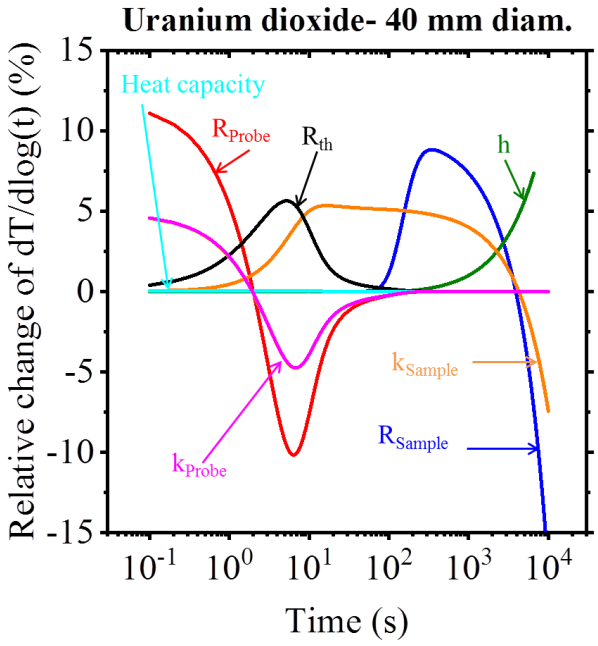

Figure 4.8: Relative change v. time plot for 40 mm diameter UO_2 sample comparing probe radius (R_{probe}), thermal conductivity of probe (k_{probe}), thermal contact resistance (R_{th}), sample radius (R_{sample}), thermal conductivity of sample (k_{sample}), convection (h), and various probe thermal properties.

Using the thermal contact resistance and convection coefficients determined experimentally, the analytic model will be used to simulate experiments on UO_2 samples of various diameters. These results will inform the expected quality of experimental results that can be obtained from UO_2 samples. Additionally, these results can be used to aid in the design of an experiment to ensure good thermal conductivity measurements. Figure 4.9a shows the simulated temperature v. time plot for a varying diameter of 20 mm, 40 mm, and 60 mm. Figure 4.9b shows the dT/dlog(t) v. time graph, where the solid black line is the slope that corresponds to the thermal conductivity of UO_2 and the two dashed black lines are the slopes that correspond to $\pm$5% of the UO_2 thermal conductivity. For a 20 mm diameter, the dT/dlog(t) curve never enters the 5% thermal conductivity range. If the standard data

reduction technique of fitting the linear region for the slope was used for this data, it would not have obtained an accurate measurement because the semi-infinite assumption was not satisfied. However, a 40 mm diameter remains within the 5% thermal conductivity range from 37 seconds to 124 seconds. This indicates that UO_2 can have a minimum diameter of 40 mm while still remaining within the 5% thermal conductivity range for a sufficient amount of time. This further confirms the previous sensitivity parameter plots that a 40 mm diameter of UO_2 is the sufficient sample size for the current needle probe being used, if the standard data reduction procedure is used. The derived analytic model could be used to fit the thermal properties of the sample to the experimental data without using the standard data reduction technique. This technique is a standard method to determine properties through the inverse problem, and is routinely performed with thermal wave techniques[151, 152].

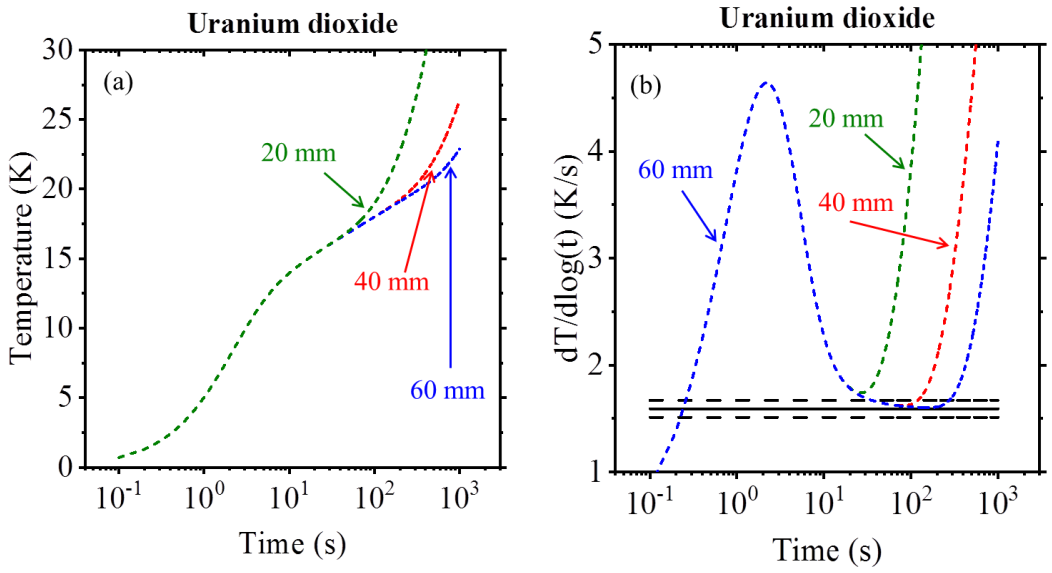

Figure 4.9: (a) Temperature v. time plot and (b) dT/dlog(t) plot comparing the minimum diameter of UO_2 samples.

The influence of thermal contact resistance between the needle probe and UO_2 was also investigated using the analytic model. Figure 4.10a shows the thermal contact resistances of 0.01, 0.1, and 1 $K \cdot m^2/W$. Thermal contact resistance of 0.01 $K \cdot m^2/W$ and 0.1 $K \cdot m^2/W$ stay within the 5% thermal conductivity range for approximately the same amount of time. Meanwhile 1 $K \cdot m^2/W$ does not stay within the 5% thermal conductivity range for a sufficient

amount of time (Figure 4.10b). Therefore, any contact resistance less than 0.1 K·m^2/W can be considered negligible for this set of geometry and material properties.

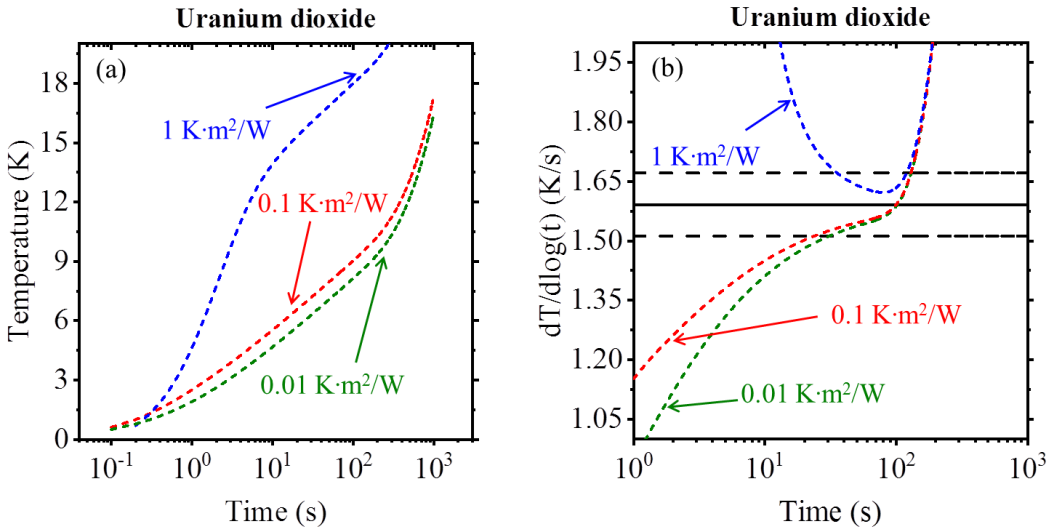

Figure 4.10: (a) Temperature v. time plot and (b) dT/dlog(t) plot comparing the smallest thermal contact resistance for a 40 mm diameter UO_2 sample.

Another approach to improving the thermal conductivity measurement method is to use a smaller needle probe diameter. Figure 4.11a shows that for a 40 mm diameter UO_2 sample, a probe diameter of 0.2 mm allows for the measurement to remain within the 5% thermal conductivity range for the longest time period (Figure 4.11b). This indicates that the smaller the probe becomes, it begins to more closely model a true line heat source and will remain within the 5% thermal conductivity range for a longer amount of time. This indicates that, if the needle probe could be miniaturized, it could be used on smaller diameter samples.

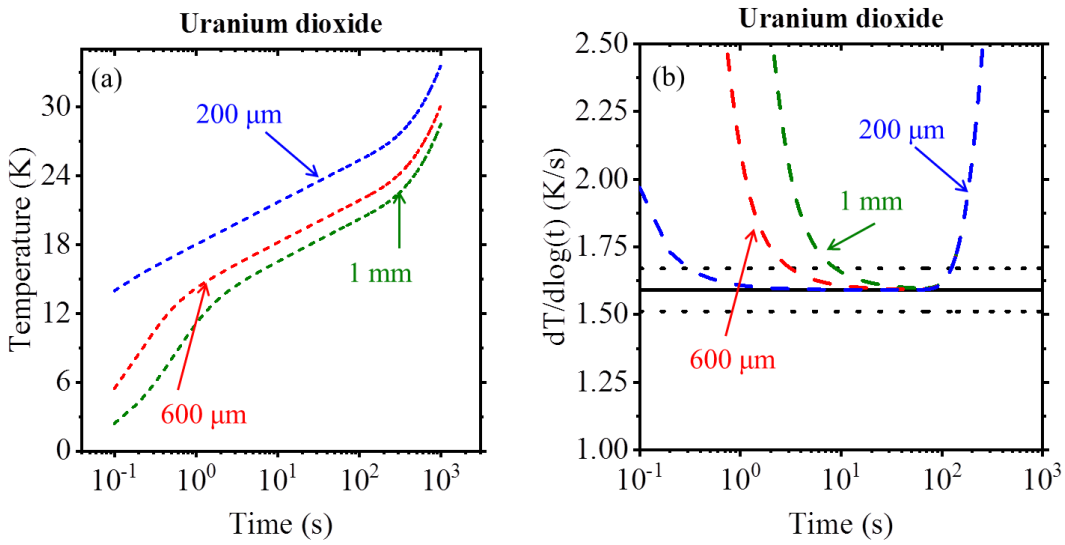

Figure 4.11: (a) Temperature v. time plot and (b) dT/dlog(t) plot comparing smaller needle probe diameters for a 40 mm diameter UO_2 sample.

4.6 Conclusions

This study has developed a quadrupoles model that can be used to predict the needle probe measurement process for materials of various thermal conductivities. The model is especially important for applications to multilayered systems with thermal contact resistance and finite size. This analytic model was verified with a finite element software model. Validation was performed using a custom built probe and cylindrical PTFE and stainless steel 304 samples of varying diameters. The analytic model was used to fit the experimental data to determine the thermal conductivity, showing a good agreement within 9% for reference samples. A sensitivity parameter study was then performed to understand how each parameter influences the thermal conductivity measurement when using the needle probe. It has also shown potential to help optimize the current needle probe thermal conductivity measurement configuration.

For prototypic UO_2 nuclear fuel, the semi-infinite assumption typically required for the standard line source technique is quickly violated during a measurement. However, using a more complex data reduction with the developed analytic model, the thermal conductivity may be determined, though care must be taken to ensure unique fitting solutions for thermal conductivity. The sensitivity studies on various parameters shows a large region of time when the sample's radius and thermal conductivity have a high sensitivity. Therefore, it is possible

to determine the thermal conductivity of samples that have a known diameter by fitting the thermal response. The results indicate promise for measuring samples that have a diameter of approximately 10 mm.

Experimental and analytical studies with the current needle probe geometry show that the thermal contact resistance and probe size are the most limiting factors to improving measurements. It has been shown that the thermal contact resistance should be no larger than 0.1 $K \cdot m^2/W$ to have a negligible influence on the thermal conductivity measurements. In addition, using a smaller probe diameter could increase the amount of time spent within the 5% thermal conductivity range.

4.7 References

1. C. Ronchi, M. Sheindlin, D. Staicu, and M. Kinoshita, "Effect of burn-up on the thermal conductivity of uranium dioxide up to 100.000 MWdt−1," *Journal of Nuclear Materials,* vol. 327, no. 1, pp. 58-76, 2004, doi: https://doi.org/10.1016/j.jnucmat.2004.01.018.

2. S. Ishimoto, M. Hirai, K. Ito, and Y. Korei, "Effects of soluble fission products on thermal conductivities of nuclear fuel pellets," *Journal of Nuclear Science and Technology,* vol. 31, no. 8, pp. 796-802, 1994, doi: 10.1080/18811248.1994.9735225.

3. M. Hirai, "Thermal diffusivity of UO2-Gd2O3 pellets," *Journal of Nuclear Materials,* vol. 173, no. 3, pp. 247-254, 1990, doi: https://doi.org/10.1016/0022-3115(90)90392-Z.

4. M. J. Welland, R. Böhler, L. Vlahovic, K. Boboridis, and D. Manara, "Co-development of experimental and simulation methods for the laser flash heating and melting technique: the thermoelastic effects of UO2," *International Journal of Thermal Sciences,* vol. 132, pp. 174-185, 2018, doi: https://doi.org/10.1016/j.ijthermalsci.2018.05.035.

5. W. Wiesenack and T. Tverberg, "The OECD Halden reactor project fuels testing programme: methods, selected results and plans," *Nuclear Engineering and Design,* vol. 207, no. 2, pp. 189-197, 2001, doi: https://doi.org/10.1016/S0029-5493(00)00385-X.

6. J. Daw, J. Rempe, K. Condie, D. Knudson, S. Wilkins, B. Fox, and H. Ban, "Hot wire needle probe for in-pile thermal conductivity detection," United States, 2001. https://www.osti.gov/servlets/purl/1004270

7. J. Rempe, D. Knudson, J. Daw, T. Unruh, B. Chase, K. Davis, A. Palmer, and R. Schley, "Advanced in-pile instrumentation for materials testing reactors," *IEEE Transactions on Nuclear Science,* vol. 61, no. 4, pp. 1984-1994, Aug. 2014, doi: 10.1109/TNS.2014.2335616.

8. *Standard test method for determination of thermal conductivity of soil and soft rock by thermal needle probe procedure*. ASTMD Standard, 5334-08, 2008.

9. L. Marmoret and H. Humaish, "Limit of validity of the log-linear model for determining thermal properties of light insulation materials with cylindrical hot probe," *International Journal of Thermal Sciences,* vol. 117, pp. 251-259, 2017, doi: https://doi.org/10.1016/j.ijthermalsci.2017.04.002.

10. H. Demir, A. Koyun, and G. Temir, "Heat transfer of horizontal parallel pipe ground heat exchanger and experimental verification," *Applied Thermal Engineering,* vol. 29, no. 2-3, pp. 224-233, 2009.

11. M. Li and A. C. K. Lai, "Heat-source solutions to heat conduction in anisotropic media with application to pile and borehole ground heat exchangers," *Applied Energy,* vol. 96, pp. 451-458, 2012.

12. M. Li and A. C. K. Lai, "Review of analytical models for heat transfer by vertical ground heat exchangers (GHEs): A perspective of time and space scales," *Applied Energy,* vol. 151, pp. 178-191, 2015.

13. Y. Yang and M. Li, "Short-time performance of composite-medium line-source model for predicting responses of ground heat exchangers with single U-shaped tube," *International Journal of Thermal Sciences,* vol. 82, pp. 130-137, 2014, doi: https://doi.org/10.1016/j.ijthermalsci.2014.04.002.

14. J. Blackwell, "A transient-flow method for determination of thermal constants of insulating materials in bulk part I—Theory," *Journal of Applied Physics,* vol. 25, no. 2, pp. 137-144, 1954.

15. W. F. Waite, L. Y. Gilbert, W. J. Winters, and D. H. Mason, "Estimating thermal diffusivity and specific heat from needle probe thermal conductivity data," *Review of Scientific Instruments,* vol. 77, no. 4, p. 044904, 2006.

16. L. Lamarche and B. Beauchamp, "New solutions for the short-time analysis of geothermal vertical boreholes," *International Journal of Heat and Mass Transfer,* vol. 50, no. 7-8, pp. 1408-1419, 2007.

17. P. Metz, "A simple computer program to model three-dimensional underground heat flow with realistic boundary conditions," *Journal of Solar Energy Engineering,* vol. 105, no. 1, pp. 42-49, 1983.

18. Y. Gu and D. L. O'Neal, "An analytical solution to transient heat conduction in a composite region with a cylindrical heat source," *Journal of Solar Energy Engineering,* vol. 117, no. 3, pp. 242-248, 1995.

19. G. Bandyopadhyay, W. Gosnold, and M. Mann, "Analytical and semi-analytical solutions for short-time transient response of ground heat exchangers," *Energy and Buildings,* vol. 40, no. 10, pp. 1816-1824, 2008.

20. M. D. Mikhailov, M. N. Özişik, and N. L. Vulchanov, "Diffusion in composite layers with automatic solution of the eigenvalue problem," *International Journal of Heat and Mass Transfer,* vol. 26, no. 8, pp. 1131-1141, 1983.

21. A. Haji-Sheikh and J. V. Beck, "Temperature solution in multi-dimensional multi-layer bodies," *International Journal of Heat and Mass Transfer,* vol. 45, no. 9, pp. 1865-1877, 2002.

22. D. Maillet, *Thermal quadrupoles: solving the heat equation through integral transforms*. John Wiley & Sons Inc, 2000.

23. "Technical Information - Polytetrafluoroethylene Polytetrafluoroethylene PTFE." http://www.goodfellow.com/catalogue/GFCat2H.php?ewd_token=QyTGBL1K7e14OPEIT7SvAejfQ1bDty&n=krjr2hZewT9mQyqnNN1FVhT4nNzToZ&ewd_urlNo=GFCat2L3&Head=FP30 (accessed January 23, 2019).

24. J. Blumm, A. Lindemann, M. Meyer, and C. Strasser, "Characterization of PTFE using advanced thermal analysis techniques," *International Journal of Thermophysics,* vol. 31, no. 10, pp. 1919-1927, 2010.

25. B. F. Blackwell, W. Gill, K. Dowding, and T. E. Voth, "Determiniation of thermal conductivity of 304 stainless steel using parameter estimation techniques," *ASME Paper,* NHTC2000-12141, 2000.

26. R. S. Graves, T. G. Kollie, D. L. McElroy, and K. E. Gilchrist, "The thermal conductivity of AISI 304L stainless steel," *International Journal of Thermophysics,* vol. 12, no. 2, pp. 409-415, 1991.

27. F. Reisdorffer, B. Garnier, N. Horny, C. Renaud, M. Chirtoc, and T.-P. Nguyen, "Thermal conductivity of organic semi-conducting materials using 3omega and photothermal radiometry techniques," *EPJ Web of Conferences,* vol. 79, 2014.

28. R. Celorrio, A. Mendioroz, E. Apiñaniz, A. Salazar, C. Wang, and A. Mandelis, "Reconstruction of radial thermal conductivity depth profile in case hardened steel rods," *Journal of Applied Physics,* vol. 105, no. 8, p. 083517, 2009.

CHAPTER 5: CONCLUSIONS

5.1 Conclusions for Thermoelectric Work

This study has reported the high-performance of flexible Bi_2Te_3 thin films fabricated from a low-cost and scalable solution wet-chemistry synthesis process. It was found that as the annealing temperature increases, the room-temperature electrical conductivity increases from 1.8×10^4 to 2.9×10^4 S/m. The higher annealing temperature allowed for the removal of PVP on the surface while enhancing the interaction between nanoplates. However, the annealing temperature had to be kept below the melting point of the polyimide substrate. Bi_2Te_3 thin films annealed at 623 K exhibit a power factor of 0.35 $mW/m \cdot K^2$ at 433 K, indicating that the thermoelectric properties can be optimized by controlling the annealing temperature. This power factor is higher than any other reported wet-chemistry fabricated Bi_2Te_3 films.

Evaluation of the sample's flexibility was achieved by performing room-temperature electrical resistance bend test measurements. Initial static bend tests were performed on various radii of curvature: 10 mm, 20 mm, 30 mm, 40 mm, and 50 mm. Bending films around a 10 mm ROC resulted in the highest change in resistance of 17%. Meanwhile, the 50 mm ROC exhibited the lowest change in resistance of 5%. From there, dynamic bend tests were performed. For a 50 mm ROC, the electrical change in resistance of the spin coated films showed less than a 13% increase after 100 cycles and after 1000 cycles there was a 23% increase. By comparison, screen-printed Bi_2Te_3 had an increase in resistance of 4.5% during a 150 bend cycle around a 5 mm ROC while AJP films showed a 7% increase for 1000 bending cycles for a 50 mm ROC. The smaller resistance increase for screen-printed and aerosol jet printed films is due to a higher film thickness. This creates a more robust film that is less sensitive to electrical resistance changes during bend testing.

It was also demonstrated that the Bi_2Te_3 ink could be used to successfully create AJP thin films. The electrical conductivity of AJP films was 939.64 S/m and the Seebeck coefficient was -57 μV/K. The decrease in electrical conductivity of AJP films can be attributed due to the increase in porosity since the AJP process initially aerosolizes the ink before it is deposited on the film.

5.2 Conclusions for Needle Probe Work

This study developed a transient, multilayer analytical model using the quadrupoles method. The analytic model can be used to predict the needle probe measurement process for materials of various thermal conductivities. Verification was performed by comparing the analytic model with a finite element software model. Validation of the custom INL probe was performed using cylindrical PTFE and stainless steel 304 samples of varying diameters. In order to further understand how each parameter influenced the thermal conductivity measurements using the needle probe method, a sensitivity parameter study was performed. The parameter study also demonstrated how the current needle probe thermal conductivity measurement process could be optimized.

Employing the standard equation for data reduction involving the slope of the temperature v. time plot to determine thermal conductivity is not feasible for prototypic UO_2 fuel. However, with the developed analytic model, a more complex data reduction technique could be used to determine the thermal conductivity. Furthermore, the sensitivity study for various parameters showed a large region of time when the sample's radius and thermal conductivity had a high sensitivity. Thus, it was possible to determine the thermal conductivity of samples that have a known geometry by fitting the thermal response. This approach could be applied to measure samples that even have a diameter of 10 mm.

Based on the current needle probe geometry and experimental studies, the thermal contact resistance and probe size are the most important factors to consider for improvement measurements. It has been shown that a thermal contact resistance less than 0.1 $K \cdot m^2/W$ has a negligible influence on the thermal conductivity measurements. In addition, using a smaller probe diameter can drastically increase the amount of time spent within the 5% thermal conductivity range.

CHAPTER 6: FUTURE WORK

6.1 Future Work for Thermoelectric Work

Current energy consumption presents a challenge that society must continue to address. In particular, power dissipation requires excess energy to be used as a result of inefficient electronics. Thermoelectric materials provide a solution to waste heat recovery through the use of small scale energy harvesters.

The work presented here resulted in the development of a low-cost and scalable chemistry method for fabrication of Bi_2Te_3 thin films. A thin film peak power factor of 0.35 $mW/m \cdot K^2$ at 433K is among the highest reported values for flexible TE films. The next step is to create a TEG using n-type and p-type TE inks. Previously, p-type Cu_2Se thin films were created using a wet-chemical synthesis method. Utilizing both the Bi_2Te_3 and Cu_2Se inks, additive manufacturing can be used to create thin film TEGs.

Employing additive manufacturing allows for more flexibility in designs. As a result, the design space can be maximized and is less restricted relative to spin coated films. Furthermore, this allows for more flexibility in the overall design of the TEG while also providing a faster solution to production.

6.2 Future Work for Needle Probe Work

Measuring the thermal conductivity of nuclear fuels in-pile will further the application of new fuels and testing. Additionally, it will provide a better understanding of the structural materials of nuclear reactors.

This work improved the accuracy of the in-pile transient needle probe method through the development of a time-based quadrupoles method. This model was verified and validated using a finite element model and experimental results, respectively. The next step is to extend this method to a frequency-based domain. This will allow for longer measurement periods since the heat will no longer travel to the outer surface. As a result of the measurement period being extended, the amount of time spent within the 5% thermal conductivity range will improve accuracy.

Another interest is to use the transient needle probe method to measure liquid fuels. As of now, solid fuels are used in light water reactors. This previously resulted in a need to

understand how much influence the thermal contact resistance had on the measurement. However, molten salts are a type of liquid fuel that will eventually be used. This introduces new challenges to determine how to accurately measure the thermal conductivity of such liquid fuels. Such future work will aid in the progression of advanced technology fuels used to improve the energy production of nuclear reactors.

REFERENCES

1. Quadrennial Technology Review 2015. **2019**.

2. Where Greenhouse Gases Come From - Energy Explained, Your Guide To Understanding Energy - Energy Information Administration. https://www.eia.gov/energyexplained/index.php?page=environment_where_ghg_come_from.

3. Pop, E., Energy dissipation and transport in nanoscale devices. *Nano Research* **2010,** *3* (3), 147-169.

4. Kaplan, J. M.; Forrest, W.; Kindler, N. *Revolutionizing data center energy efficiency*; Technical report, McKinsey & Company: 2008.

5. EPA report to Congress on server and data center energy efficiency. **2019**.

6. Roundy, S.; Steingart, D.; Frechette, L.; Wright, P.; Rabaey, J. In *Power sources for wireless sensor networks*, 2004; Springer: pp 1-17.

7. Wei, X.; Liu, J., Power sources and electrical recharging strategies for implantable medical devices. *Frontiers of Energy and Power Engineering in China* **2008,** *2* (1), 1-13.

8. Cadei, A.; Dionisi, A.; Sardini, E.; Serpelloni, M., Kinetic and thermal energy harvesters for implantable medical devices and biomedical autonomous sensors. *Measurement Science and Technology* **2014,** *25* (1), 14.

9. Roundy, S.; Wright, P. K., A piezoelectric vibration based generator for wireless electronics. *Smart Materials and structures* **2004,** *13* (5), 1131.

10. Rasouli, M.; Phee, L. S. J., Energy sources and their development for application in medical devices. *Expert Review of Medical Devices* **2010,** *7* (5), 693-709.

11. Williams, C. B.; Shearwood, C.; Harradine, M. A.; Mellor, P. H.; Birch, T. S.; Yates, R. B., Development of an electromagnetic micro-generator. *Iee Proceedings-Circuits Devices and Systems* **2001,** *148* (6), 337-342.

12. Beeby, S. P.; Torah, R. N.; Tudor, M. J.; Glynne-Jones, P.; O'Donnell, T.; Saha, C. R.; Roy, S., A micro electromagnetic generator for vibration energy harvesting. *Journal of Micromechanics and microengineering* **2007,** *17* (7), 1257.

13. Sari, I.; Balkan, T.; Kulah, H., An electromagnetic micro power generator for wideband environmental vibrations. *Sensors and Actuators A: Physical* **2008,** *145*, 405-413.

14. Paracha, A. M.; Basset, P.; Marty, F.; Chasin, A. V.; Poulichet, P.; Bourouina, T., A high power density electrostatic vibration-to-electric energy converter based on an in-plane overlap plate (IPOP) mechanism. *arXiv preprint arXiv:0802.3063* **2008**.

15. Romero, E.; Warrington, R. O.; Neuman, M. R., Energy scavenging sources for biomedical sensors. *Physiological Measurement* **2009,** *30* (9), R35-R62.

16. Williams, C. B.; Shearwood, C.; Harradine, M. A.; Mellor, P. H.; Birch, T. S.; Yates, R. B., Development of an electromagnetic micro-generator. *IEE Proceedings-Circuits, Devices and Systems* **2001,** *148* (6), 337-342.

17. Tashiro, R.; Kabei, N.; Katayama, K.; Ishizuka, Y.; Tsuboi, F.; Tsuchiya, K., Development of an electrostatic generator that harnesses the motion of a living body (use of a resonant phenomenon). *Jsme International Journal Series C-Mechanical Systems Machine Elements and Manufacturing* **2000,** *43* (4), 916-922.

18. Tian, Z.; Lee, S.; Chen, G., A comprehensive review of heat transfer in thermoelectric materials and devices. *Ann. Rev. Heat Transfer* **2014,** *17*, 425-483.

19. Rowe, D. M., *Thermoelectrics handbook: macro to nano*. CRC press: 2005.

20. Riffat, S. B.; Ma, X. L., Thermoelectrics: a review of present and potential applications. *Applied Thermal Engineering* **2003,** *23* (8), 913-935.

21. Po, J. M.; Brito, M. C.; Alves, J. M.; Silva, J. A.; Serra, J. M.; Vallera, A. M., Measurement of the dopant concentration in a semiconductor using the Seebeck effect. *Measurement Science and Technology* **2013,** *24* (5).

22. Zhang, Y., Thermal and thermoelectric transport in nanostructured materials from pnictogen chalcogenide nanoplate crystals. **2011**.

23. Kim, S. J.; We, J. H.; Cho, B. J., A wearable thermoelectric generator fabricated on a glass fabric. *Energy & Environmental Science* **2014,** *7* (6), 1959-1965.

24. Jo, S. E.; Kim, M. K.; Kim, M. S.; Kim, Y. J., Flexible thermoelectric generator for human body heat energy harvesting. *Electronics letters* **2012,** *48* (16), 1.

25. Leonov, V., Energy Harvesting for Self-Powered Wearable Devices. In *Wearable Monitoring Systems*, Springer US: Boston, MA, 2011; pp 27-49.

26. Francioso, L.; De Pascali, C.; Farella, I.; Martucci, C.; Cretì, P.; Siciliano, P.; Perrone, A., Flexible thermoelectric generator for ambient assisted living wearable biometric sensors. *Journal of Power Sources* **2011,** *196* (6), 3239-3243.

27. Monteith, J. L.; Mount, L. E., *Heat loss from animals and man: assessment and control*. Elsevier: 2013.

28. Electricity in the United States - Energy Explained, Your Guide To Understanding Energy - Energy Information Administration. https://www.eia.gov/energyexplained/index.php?page=electricity_in_the_united_states.

29. Fossil fuels still dominate U.S. energy consumption despite recent market share decline. **2019**.

30. Global gas production growth, 2016-2022. **2019**.

31. Durucan, S.; Korre, A.; Munoz-Melendez, G., Mining life cycle modelling: a cradle-to-gate approach to environmental management in the minerals industry. *Journal of Cleaner Production* **2006,** *14* (12-13), 1057-1070.

32. Even as renewables increase, fossil fuels continue to dominate U.S. energy mix. **2019**.

33. United States remains the world's top producer of petroleum and natural gas hydrocarbons. **2019**.

34. EIA - Annual Energy Outlook 2018. https://www.eia.gov/outlooks/aeo/.

35. Nuclear - Energy Explained, Your Guide To Understanding Energy - Energy Information Administration. https://www.eia.gov/energyexplained/index.php?page=nuclear_home.

36. EPRI Executive Summary. https://www.epri.com/#/pages/summary/000000003002011803/?lang=en.

37. Shafiee, S.; Topal, E., When will fossil fuel reserves be diminished? *Energy policy* **2009,** *37* (1), 181-189.

38. How long will the world's uranium supplies last? **2019**.

39. Cooling Power Plants.

40. Daw, J. E.; Rempe, J. L.; Knudson, D. L., Hot Wire Needle Probe for In-Reactor Thermal Conductivity Measurement. *IEEE Sensors Journal* **2012,** *12* (8), 2554-2560.

41. Kim, B. G.; Rempe, J. L.; Villard, J.-F.; Solstad, S., Review of instrumentation for irradiation testing of nuclear fuels and materials. *Nuclear Technology* **2011,** *176* (2), 155-187.

42. Gao, X.; Uehara, K.; Klug, D. D.; Tse, J. S., Rational design of high-efficiency thermoelectric materials with low band gap conductive polymers. *Computational Materials Science* **2006,** *36* (1-2), 49-53.

43. Glosch, H.; Ashauer, M.; Pfeiffer, U.; Lang, W., A thermoelectric converter for energy supply. *Sensors and Actuators a-Physical* **1999,** *74* (1-3), 246-250.

44. Nolas, G. S.; Sharp, J.; Goldsmid, J., *Thermoelectrics: basic principles and new materials developments*. Springer Science & Business Media: 2013.

45. Sootsman, J. R.; Chung, D. Y.; Kanatzidis, M. G., New and Old Concepts in Thermoelectric Materials. *Angewandte Chemie International Edition* **2009,** *48* (46), 8616-8639.

46. Boffoué, O.; Jacquot, A.; Dauscher, A.; Lenoir, B.; Stölzer, M., Experimental setup for the measurement of the electrical resistivity and thermopower of thin films and bulk materials. *Review of Scientific Instruments* **2005,** *76* (5), 053907.

47. Bahk, J.-H.; Favaloro, T.; Shakouri, A., Thin film thermoelectric characterization techniques. *Annual Review of Heat Transfer* **2013,** *16* (1).

48. Hollar, C., Thermoelectric Material Property Measurement for Flexible Films. **2016**.

49. Schroder, D. K., *Semiconductor material and device characterization*. John Wiley & Sons: 2006.

50. Nalwa, H. S., *Handbook of Thin Films, Five-Volume Set*. Academic Press: 2001.

51. Wieder, H. H., *Laboratory notes on electrical and galvanomagnetic measurements*. Elsevier Scientific Pub. Co., distributors for the U.S. and Canada, Elsevier/North-Holland: Amsterdam, New York, 1979.

52. Valdes, L. B., RESISTIVITY MEASUREMENTS ON GERMANIUM FOR TRANSISTORS. *Proceedings of the Institute of Radio Engineers* **1954,** *42* (2), 420-427.

53. Matsumura, T.; Sato, Y., A theoretical study on Van der Pauw measurement values of inhomogeneous compound semiconductor thin films. *Journal of Modern Physics* **2010,** *1* (05), 340.

54. Pm, N. O., A method of measuring the resistivity and Hall coefficient on lamellae of arbitrary shape. **1958**.

55. Lu, Z.; Layani, M.; Zhao, X.; Tan, L. P.; Sun, T.; Fan, S.; Yan, Q.; Magdassi, S.; Hng, H. H., Fabrication of flexible thermoelectric thin film devices by inkjet printing. *Small* **2014,** *10* (17), 3551-3554.

56. Oh, J. Y.; Lee, J. H.; Han, S. W.; Chae, S. S.; Bae, E. J.; Kang, Y. H.; Choi, W. J.; Cho, S. Y.; Lee, J.-O.; Baik, H. K., Chemically exfoliated transition metal dichalcogenide nanosheet-based wearable thermoelectric generators. *Energy & Environmental Science* **2016,** *9* (5), 1696-1705.

57. Mehta, R. J.; Zhang, Y. L.; Karthik, C.; Singh, B.; Siegel, R. W.; Borca-Tasciuc, T.; Ramanath, G., A new class of doped nanobulk high-figure-of-merit thermoelectrics by scalable bottom-up assembly. *Nature Materials* **2012,** *11* (3), 233-240.

58. Wan, C. L.; Gu, X. K.; Dang, F.; Itoh, T.; Wang, Y. F.; Sasaki, H.; Kondo, M.; Koga, K.; Yabuki, K.; Snyder, G. J.; Yang, R. G.; Koumoto, K., Flexible n-type thermoelectric materials by organic intercalation of layered transition metal dichalcogenide TiS2. *Nature Materials* **2015,** *14* (6), 622-627.

59. Dettmer, E. S.; Romenesko, B. M.; Charles, H. K.; Carkhuff, B. G.; Merrill, D. J. In *Steady state thermal conductivity measurements of AlN and SiC substrate materials*, 1989; IEEE: pp 551-556.

60. Zawilski, B. M.; Littleton, R. T.; Tritt, T. M., Description of the parallel thermal conductance technique for the measurement of the thermal conductivity of small diameter samples. *Review of Scientific Instruments* **2001,** *72* (3), 1770-1774.

61. Dames, C., Measuring the thermal conductivity of thin films: 3 omega and related electrothermal methods. *Annual Review of Heat Transfer* **2013,** *16* (16).

62. Ju, Y. S.; Kurabayashi, K.; Goodson, K. E., Thermal characterization of anisotropic thin dielectric films using harmonic Joule heating. *Thin Solid Films* **1999,** *339* (1-2), 160-164.

63. Cahill, D. G.; Fischer, H. E.; Klitsner, T.; Swartz, E. T.; Pohl, R. O., THERMAL-CONDUCTIVITY OF THIN-FILMS - MEASUREMENTS AND UNDERSTANDING. *Journal of Vacuum Science & Technology a-Vacuum Surfaces and Films* **1989,** *7* (3), 1259-1266.

64. Paddock, C. A.; Eesley, G. L., TRANSIENT THERMOREFLECTANCE FROM THIN METAL-FILMS. *Journal of Applied Physics* **1986,** *60* (1), 285-290.

65. Garrelts, R.; Marconnet, A.; Xu, X. F., ASSESSMENT OF THERMAL PROPERTIES VIA NANOSECOND THERMOREFLECTANCE METHOD. *Nanoscale and Microscale Thermophysical Engineering* **2015,** *19* (4), 245-257.

66. Capinski, W. S.; Maris, H. J., Improved apparatus for picosecond pump‐and‐probe optical measurements. *Review of Scientific Instruments* **1996,** *67* (8), 2720-2726.

67. Taketoshi, N.; Baba, T.; Schaub, E.; Ono, A., Homodyne detection technique using spontaneously generated reference signal in picosecond thermoreflectance measurements. *Review of scientific instruments* **2003,** *74* (12), 5226-5230.

68. Bonello, B.; Perrin, B.; Rossignol, C., Photothermal properties of bulk and layered materials by the picosecond acoustics technique. *Journal of applied physics* **1998,** *83* (6), 3081-3088.

69. Cahill, D. G., Analysis of heat flow in layered structures for time-domain thermoreflectance. *Review of scientific instruments* **2004,** *75* (12), 5119-5122.

70. Parker, W. J.; Jenkins, R. J.; Butler, C. P.; Abbott, G. L., Flash method of determining thermal diffusivity, heat capacity, and thermal conductivity. *Journal of applied physics* **1961,** *32* (9), 1679-1684.

71. dos Santos, W. N.; Mummery, P.; Wallwork, A., Thermal diffusivity of polymers by the laser flash technique. *Polymer testing* **2005,** *24* (5), 628-634.

72. LFA 1000 | Linseis Messgeräte GmbH. **2019**.

73. Cahill, D. G.; Goodson, K.; Majumdar, A., Thermometry and thermal transport in micro/nanoscale solid-state devices and structures. *Journal of Heat Transfer* **2002,** *124* (2), 223-241.

74. Joshua, D.; Joy, R.; Keith, C.; Darrell, K.; Wilkins, S. C.; Brandon, S. F.; Heng, B. In *Hot Wire Needle Probe for In-Pile Thermal Conductivity Detection*, United States, United States, 2001.

75. Rempe, J. L.; Knudson, D. L.; Daw, J. E.; Unruh, T. C.; Chase, B. M.; Davis, K. L.; Palmer, A. J.; Schley, R. S., Advanced In-Pile Instrumentation for Materials Testing Reactors. *IEEE Transactions on Nuclear Science* **2014,** *61* (4), 1984-1994.

76. Rempe, J. L.; Knudson, D. L.; Daw, J. E.; Unruh, T.; Chase, B. M.; Palmer, J.; Condie, K. G.; Davis, K. L., Enhanced In-Pile Instrumentation at the Advanced Test Reactor. *IEEE Transactions on Nuclear Science* **2012,** *59* (4), 1214-1223.

77. Rempe, J. L.; Knudson, D. L.; Condie, K. G.; Daw, J. E.; Ban, H.; Fox, B. S.; Kohse, G. E., New Sensors for the Advanced Test Reactor National Scientific User Facility. *IEEE Transactions on Nuclear Science* **2010,** *57* (5), 2653-2661.

78. Demir, H.; Koyun, A.; Temir, G., Heat transfer of horizontal parallel pipe ground heat exchanger and experimental verification. *Applied thermal engineering* **2009,** *29* (2-3), 224-233.

79. Li, M.; Lai, A. C. K., Heat-source solutions to heat conduction in anisotropic media with application to pile and borehole ground heat exchangers. *Applied Energy* **2012,** *96*, 451-458.

80. Li, M.; Lai, A. C. K., Review of analytical models for heat transfer by vertical ground heat exchangers (GHEs): A perspective of time and space scales. *Applied Energy* **2015,** *151*, 178-191.

81. Blackwell, J., A transient‐flow method for determination of thermal constants of insulating materials in bulk part I—Theory. *Journal of applied physics* **1954,** *25* (2), 137-144.

82. Waite, W. F.; Gilbert, L. Y.; Winters, W. J.; Mason, D. H., Estimating thermal diffusivity and specific heat from needle probe thermal conductivity data. *Review of Scientific Instruments* **2006,** *77* (4), 044904.

83. Lamarche, L.; Beauchamp, B., New solutions for the short-time analysis of geothermal vertical boreholes. *International Journal of Heat and Mass Transfer* **2007,** *50* (7-8), 1408-1419.

84. Metz, P., A simple computer program to model three-dimensional underground heat flow with realistic boundary conditions. *Journal of Solar Energy Engineering* **1983,** *105* (1), 42-49.

85. Gu, Y.; O'Neal, D. L., An analytical solution to transient heat conduction in a composite region with a cylindrical heat source. *Journal of solar energy engineering* **1995,** *117* (3), 242-248.

86. Bandyopadhyay, G.; Gosnold, W.; Mann, M., Analytical and semi-analytical solutions for short-time transient response of ground heat exchangers. *Energy and Buildings* **2008,** *40* (10), 1816-1824.

87. Mikhailov, M. D.; Özişik, M. N.; Vulchanov, N. L., Diffusion in composite layers with automatic solution of the eigenvalue problem. *International Journal of Heat and Mass Transfer* **1983,** *26* (8), 1131-1141.

88. Haji-Sheikh, A.; Beck, J. V., Temperature solution in multi-dimensional multi-layer bodies. *International Journal of Heat and Mass Transfer* **2002,** *45* (9), 1865-1877.

89. Maillet, D., *Thermal quadrupoles: solving the heat equation through integral transforms*. John Wiley & Sons Inc: 2000.

90. Jensen, C. B., Bridging the Nano-and Macro-Worlds: Thermal Property Measurement Using Thermal Microscopy and Photothermal Radiometry–Application to Particle-Irradiation Damage Profile in Zirconium Carbide. **2014**.

91. Fleming, A., Personal interview. 2018.

92. Bahk, J. H.; Fang, H. Y.; Yazawa, K.; Shakouri, A., Flexible thermoelectric materials and device optimization for wearable energy harvesting. *Journal of Materials Chemistry C* **2015,** *3* (40), 10362-10374.

93. Wearable Technology Market worth 51.60 Billion USD by 2022. https://www.marketsandmarkets.com/PressReleases/wearable-electronics.asp.

94. Haahr, R. G.; Duun, S.; Thomsen, E. V.; Hoppe, K.; Branebjerg, J. In *A wearable "electronic patch" for wireless continuous monitoring of chronically diseased patients*, 2008 5th International Summer School and Symposium on Medical Devices and Biosensors, 1-3 June 2008; 2008; pp 66-70.

95. Son, D.; Lee, J.; Qiao, S.; Ghaffari, R.; Kim, J.; Lee, J. E.; Song, C.; Kim, S. J.; Lee, D. J.; Jun, S. W.; Yang, S.; Park, M.; Shin, J.; Do, K.; Lee, M.; Kang, K.; Hwang, C. S.; Lu, N. S.; Hyeon, T.; Kim, D. H., Multifunctional wearable devices for diagnosis and therapy of movement disorders. *Nature Nanotechnology* **2014,** *9* (5), 397-404.

96. Sun, M. G.; Fernstrom, J. D.; Jia, W. Y.; Hackworth, S. A.; Yao, N.; Li, Y. C.; Li, C. L.; Fernstrom, M. H.; Sclabassi, R. J., A Wearable Electronic System for Objective Dietary Assessment. *Journal of the American Dietetic Association* **2010,** *110* (1), 45-47.

97. Roundy, S.; Steingart, D.; Frechette, L.; Wright, P.; Rabaey, J. In *Power Sources for Wireless Sensor Networks*, Berlin, Heidelberg, Springer Berlin Heidelberg: Berlin, Heidelberg, 2004; pp 1-17.

98. Zhou, G.; Li, F.; Cheng, H.-M., Progress in flexible lithium batteries and future prospects. *Energy & Environmental Science* **2014,** *7* (4), 1307-1338.

99. Hu, L.; Wu, H.; La Mantia, F.; Yang, Y.; Cui, Y., Thin, flexible secondary Li-ion paper batteries. *ACS nano* **2010,** *4* (10), 5843-5848.

100. Meninger, S.; Mur-Miranda, J. O.; Amirtharajah, R.; Chandrakasan, A. P.; Lang, J. H., Vibration-to-electric energy conversion. *Ieee Transactions on Very Large Scale Integration (Vlsi) Systems* **2001,** *9* (1), 64-76.

101. Paracha, A. M.; Basset, P.; Marty, F.; Vaisman Chasin, A.; Poulichet, P.; Bourouina, T., A High Power Density Electrostatic Vibration-to-Electric Energy Converter Based On An In-Plane Overlap Plate (IPOP) Mechanism. *eprint arXiv:0802.3063* **2008**, arXiv:0802.3063.

102. Yang, Y.; Wei, X.-J.; Liu, J., Suitability of a thermoelectric power generator for implantable medical electronic devices. *Journal of Physics D: Applied Physics* **2007,** *40* (18), 5790.

103. Karami, M. A.; Inman, D. J., Powering pacemakers from heartbeat vibrations using linear and nonlinear energy harvesters. *Applied Physics Letters* **2012,** *100* (4).

104. Wong, L. S. Y.; Hossain, S.; Ta, A.; Edvinsson, J.; Rivas, D. H.; Naas, H., A very low-power CMOS mixed-signal IC for implantable pacemaker applications. *Ieee Journal of Solid-State Circuits* **2004,** *39* (12), 2446-2456.

105. MacKenzie, J. D.; Ho, C., Perspectives on Energy Storage for Flexible Electronic Systems. *Proceedings of the IEEE* **2015,** *103* (4), 535-553.

106. Rowe, D. M., *CRC handbook of thermoelectrics*. CRC press: 1995.

107. Goldsmid, H. J., Thermoelectric refrigeration. **1964**.

108. Khitun, A.; Balandin, A.; Liu, J. L.; Wang, K. L., In-plane lattice thermal conductivity of a quantum-dot superlattice. *Journal of Applied Physics* **2000,** *88* (2), 696-699.

109. Scheele, M.; Oeschler, N.; Meier, K.; Kornowski, A.; Klinke, C.; Weller, H., Synthesis and thermoelectric characterization of Bi2Te3 nanoparticles. *Advanced Functional Materials* **2009,** *19* (21), 3476-3483.

110. Poudel, B.; Hao, Q.; Ma, Y.; Lan, Y.; Minnich, A.; Yu, B.; Yan, X.; Wang, D.; Muto, A.; Vashaee, D., High-thermoelectric performance of nanostructured bismuth antimony telluride bulk alloys. *Science* **2008,** *320* (5876), 634-638.

111. Biswas, K.; He, J.; Blum, I. D.; Wu, C.-I.; Hogan, T. P.; Seidman, D. N.; Dravid, V. P.; Kanatzidis, M. G., High-performance bulk thermoelectrics with all-scale hierarchical architectures. *Nature* **2012,** *489* (7416), 414-418.

112. Li, J.-F.; Liu, W.-S.; Zhao, L.-D.; Zhou, M., High-performance nanostructured thermoelectric materials. *NPG Asia Materials* **2010,** *2* (4), 152-158.

113. Ashalley, E.; Chen, H.; Tong, X.; Li, H.; Wang, Z. M., Bismuth telluride nanostructures: preparation, thermoelectric properties and topological insulating effect. *Frontiers of Materials Science* **2015,** *9* (2), 103-125.

114. Kusagaya, K.; Hagino, H.; Tanaka, S.; Miyazaki, K.; Takashiri, M., Structural and Thermoelectric Properties of Nanocrystalline Bismuth Telluride Thin Films Under Compressive and Tensile Strain. *Journal of Electronic Materials* **2015,** *44* (6), 1632-1636.

115. Zhang, J. X.; Li, Q.; Niu, P. J.; Yang, Q. X.; Tan, B. M.; Niu, X. H.; Gao, B. H., Effect of annealing temperature on microstructure and thermoelectric properties of bismuth–telluride multilayer thin films prepared by magnetron sputtering. *Materials Research Innovations* **2015,** *19* (sup10), S10-408.

116. Takashiri, M.; Kurita, K.; Hagino, H.; Tanaka, S.; Miyazaki, K., Enhanced thermoelectric properties of phase-separating bismuth selenium telluride thin films via a two-step method. *Journal of Applied Physics* **2015,** *118* (6), 065301.

117. Lin, J.-M.; Chen, Y.-C.; Lin, C.-P.; Chien, H.-C.; Wen, C.-Y.; Chang, J.-Y.; Zhan, Z.-Y., Annealing effects on the thermoelectric properties of silver-doped bismuth telluride thin films. *Microelectronic Engineering* **2015,** *148*, 51-54.

118. Kato, K.; Hatasako, Y.; Kashiwagi, M.; Hagino, H.; Adachi, C.; Miyazaki, K., Fabrication of a Flexible Bismuth Telluride Power Generation Module Using Microporous Polyimide Films as Substrates. *Journal of Electronic Materials* **2014,** *43* (6), 1733-1739.

119. Manzano, C. V.; Abad, B.; Rojo, M. M.; Koh, Y. R.; Hodson, S. L.; Martinez, A. M. L.; Xu, X.; Shakouri, A.; Sands, T. D.; Borca-Tasciuc, T., Anisotropic Effects on the Thermoelectric Properties of Highly Oriented Electrodeposited Bi2Te3 Films. *Scientific reports* **2016,** *6*, 19129.

120. Yamaguchi, M.; Yamamuro, H.; Takashiri, M., Characteristics of electrodeposited bismuth telluride thin films with different crystal growth by adjusting electrolyte temperature and concentration. *Current Applied Physics* **2018,** *18* (12), 1513-1522.

121. Kaur, H.; Sharma, L.; Singh, S.; Sivaiah, B.; Reddy, G. B.; Senguttuvan, T. D., Enhancement in Figure of Merit (ZT) by Annealing of BiTe Nanostructures Synthesized by Microwave-Assisted Flash Combustion. *Journal of Electronic Materials* **2014,** *43* (6), 1782-1789.

122. Du, Y.; Cai, K. F.; Chen, S.; Cizek, P.; Lin, T., Facile preparation and thermoelectric properties of Bi2Te3 based alloy nanosheet/PEDOT: PSS composite films. *ACS applied materials & interfaces* **2014,** *6* (8), 5735-5743.

123. Cao, Z.; Koukharenko, E.; Tudor, M. J.; Torah, R. N.; Beeby, S. P., Flexible screen printed thermoelectric generator with enhanced processes and materials. *Sensors and Actuators A: Physical* **2016,** *238*, 196-206.

124. Son, J. S.; Choi, M. K.; Han, M.-K.; Park, K.; Kim, J.-Y.; Lim, S. J.; Oh, M.; Kuk, Y.; Park, C.; Kim, S.-J., n-Type nanostructured thermoelectric materials prepared from chemically synthesized ultrathin Bi2Te3 nanoplates. *Nano letters* **2012,** *12* (2), 640-647.

125. Hong, M.; Chen, Z.-G.; Yang, L.; Zou, J., Enhancing thermoelectric performance of Bi 2 Te 3-based nanostructures through rational structure design. *Nanoscale* **2016,** *8* (16), 8681-8686.

126. Wang, T.; Mehta, R.; Karthik, C.; Ganesan, P. G.; Singh, B.; Jiang, W.; Ravishankar, N.; Borca-Tasciuc, T.; Ramanath, G., Microsphere bouquets of bismuth telluride nanoplates: room-temperature synthesis and thermoelectric properties. *The Journal of Physical Chemistry C* **2010,** *114* (4), 1796-1799.

127. Zhang, Y.; Hu, L. P.; Zhu, T. J.; Xie, J.; Zhao, X. B., High yield Bi2Te3 single crystal nanosheets with uniform morphology via a solvothermal synthesis. *Crystal growth & design* **2013,** *13* (2), 645-651.

128. Rashad, M. M.; El-Dissouky, A.; Soliman, H. M.; Elseman, A. M.; Refaat, H. M.; Ebrahim, A., Structure evaluation of bismuth telluride (Bi2Te3) nanoparticles with enhanced

Seebeck coefficient and low thermal conductivity. *Materials Research Innovations* **2018,** *22* (6), 315-323.

129. Paulsen, J. A.; Renn, M.; Christenson, K.; Plourde, R. In *Printing conformal electronics on 3D structures with Aerosol Jet technology*, 2012; IEEE: pp 1-4.

130. Noor, A. K., *Structures technology for future aerospace systems*. American Institute of Aeronautics and Astronautics: 2000.

131. Hoey, J. M.; Reich, M. T.; Halvorsen, A.; Vaselaar, D.; Braaten, K.; Maassel, M.; Akhatov, I. S.; Ghandour, O.; Drzaic, P.; Schulz, D. L., Rapid prototyping RFID antennas using direct-write. *IEEE Transactions on Advanced Packaging* **2009,** *32* (4), 809-815.

132. Goth, C.; Putzo, S.; Franke, J. In *Aerosol Jet printing on rapid prototyping materials for fine pitch electronic applications*, 2011; IEEE: pp 1211-1216.

133. Lin, Z. Y.; Chen, Y.; Yin, A. D.; He, Q. Y.; Huang, X. Q.; Xu, Y. X.; Liu, Y. A.; Zhong, X.; Huang, Y.; Duan, X. F., Solution Processable Colloidal Nanoplates as Building Blocks for High-Performance Electronic Thin Films on Flexible Substrates. *Nano Letters* **2014,** *14* (11), 6547-6553.

134. Kong, D.; Dang, W.; Cha, J. J.; Li, H.; Meister, S.; Peng, H.; Liu, Z.; Cui, Y., Few-layer nanoplates of Bi2Se3 and Bi2Te3 with highly tunable chemical potential. *Nano letters* **2010,** *10* (6), 2245-2250.

135. Zhang, G.; Kirk, B.; Jauregui, L. A.; Yang, H.; Xu, X.; Chen, Y. P.; Wu, Y., Rational synthesis of ultrathin n-type Bi2Te3 nanowires with enhanced thermoelectric properties. *Nano letters* **2011,** *12* (1), 56-60.

136. Lin, Z.; Hollar, C.; Kang, J. S.; Yin, A.; Wang, Y.; Shiu, H. Y.; Huang, Y.; Hu, Y.; Zhang, Y.; Duan, X., A Solution Processable High‐Performance Thermoelectric Copper Selenide Thin Film. *Advanced Materials* **2017**.

137. Guo, Y.; Aisijiang, M.; Zhang, K.; Jiang, W.; Chen, Y.; Zheng, W.; Song, Z.; Cao, J.; Liu, Z.; Peng, H., Selective-Area Van der Waals Epitaxy of Topological Insulator Grid Nanostructures for Broadband Transparent Flexible Electrodes. *Advanced Materials* **2013,** *25* (41), 5959-5964.

138. Pandhi, T.; Kreit, E.; Aga, R.; Fujimoto, K.; Sharbati, M. T.; Khademi, S.; Chang, A. N.; Xiong, F.; Koehne, J.; Heckman, E. M.; Estrada, D., Electrical Transport and Power Dissipation in Aerosol-Jet-Printed Graphene Interconnects. *Scientific reports* **2018,** *8* (1), 10842.

139. Ronchi, C.; Sheindlin, M.; Staicu, D.; Kinoshita, M., Effect of burn-up on the thermal conductivity of uranium dioxide up to 100.000 MWdt−1. *Journal of Nuclear Materials* **2004,** *327* (1), 58-76.

140. Ishimoto, S.; Hirai, M.; Ito, K.; Korei, Y., Effects of Soluble Fission Products on Thermal Conductivities of Nuclear Fuel Pellets. *Journal of Nuclear Science and Technology* **1994,** *31* (8), 796-802.

141. Hirai, M., Thermal diffusivity of UO2-Gd2O3 pellets. *Journal of Nuclear Materials* **1990,** *173* (3), 247-254.

142. Welland, M. J.; Böhler, R.; Vlahovic, L.; Boboridis, K.; Manara, D., Co-development of experimental and simulation methods for the laser flash heating and melting technique: The thermoelastic effects of UO2. *International Journal of Thermal Sciences* **2018,** *132*, 174-185.

143. Wiesenack, W.; Tverberg, T., The OECD Halden reactor project fuels testing programme: methods, selected results and plans. *Nuclear Engineering and Design* **2001,** *207* (2), 189-197.

144. Mechanics, A. I. S. D. o. R., *Standard Test Method for Determination of Thermal Conductivity of Soil and Soft Rock by Thermal Needle Probe Procedure*. ASTM International: 2008.

145. Marmoret, L.; Humaish, H., Limit of validity of the log-linear model for determining thermal properties of light insulation materials with cylindrical hot probe. *International Journal of Thermal Sciences* **2017,** *117*, 251-259.

146. Yang, Y.; Li, M., Short-time performance of composite-medium line-source model for predicting responses of ground heat exchangers with single U-shaped tube. *International Journal of Thermal Sciences* **2014,** *82*, 130-137.

147. Technical Information - Polytetrafluoroethylene Polytetrafluoroethylene PTFE. http://www.goodfellow.com/catalogue/GFCat2H.php?ewd_token=QyTGBL1K7e14OPEIT7S

vAejfQ1bDty&n=krjr2hZewT9mQyqnNN1FVhT4nNzToZ&ewd_urlNo=GFCat2L3&Head=FP30 (accessed January 23, 2019).

148. Blumm, J.; Lindemann, A.; Meyer, M.; Strasser, C., Characterization of PTFE using advanced thermal analysis techniques. *International Journal of Thermophysics* **2010,** *31* (10), 1919-1927.

149. Blackwell, B. F.; Gill, W.; Dowding, K.; Voth, T. E. *Determiniation of Thermal Conductivity of 304 Stainless Steel Using Parameter Estimation Techniques*; Sandia National Labs., Albuquerque, NM (US); Sandia National Labs …: 2000.

150. Graves, R. S.; Kollie, T. G.; McElroy, D. L.; Gilchrist, K. E., The thermal conductivity of AISI 304L stainless steel. *International journal of thermophysics* **1991,** *12* (2), 409-415.

151. Reisdorffer, F.; Garnier, B.; Horny, N.; Renaud, C.; Chirtoc, M.; Nguyen, T.-P., Thermal conductivity of organic semi-conducting materials using 3omega and photothermal radiometry techniques. *EPJ Web of Conferences* **2014,** *79*.

152. Celorrio, R.; Mendioroz, A.; Apiñaniz, E.; Salazar, A.; Wang, C.; Mandelis, A., Reconstruction of radial thermal conductivity depth profile in case hardened steel rods. *Journal of Applied Physics* **2009,** *105* (8), 083517.

APPENDIX A: SUPPORTING INFORMATION FOR CHAPTER 3

A.1 Chemicals

Bismuth nitrate pentahydrate ($Bi(NO_3)_3 \cdot 5H_2O$, > 99.9%), Sodium tellurite ($NaTeO_3$, > 99.5%), Sodium hydroxide (NaOH, > 99%), Poly(vinyl pyrrolidone) (PVP, MW≈40,000) and Ethylene glycol (EG) were all purchased from Sigma-Aldrich. All the chemicals were used as received without further purification.

A.2 Solution-Phase Synthesis of Bi_2Te_3 Nanoplatelets

0.2 mmol $Bi(NO_3)_3 \cdot 5H_2O$ (0.0970 g), 0.3 mmol $NaTeO_3$ (0.0665 g), 4 mmol NaOH (0.1600 g) and 2 mmol PVP (0.2223 g) were mixed with 10 mL ethylene glycol. The mixture was stirred for ~ 10 min to fully dissolve all solids and then heated to 190°C (in about 12 min) in a 25 mL three-neck flask equipped with a thermocouple and reflux condenser in a heating mantle. After 3 hr, the heating mantle was removed and the mixture was allowed to cool down to room temperature naturally. The mixture was then centrifuged at 10000 rpm for 10 min after the addition of 20 mL isopropanol and 10 mL acetone. The supernatant was discarded and the solid was dispersed in another 40 mL isopropanol assisted by sonication. The washing steps were repeated with isopropanol two more times to remove the excessive ethylene glycol, PVP and other impurities. The final product was dispersed in isopropanol in various concentrations for further characterization.

A.3 Spin Coat Deposition of Bi_2Te_3 Film on Plastic Substrates

The dispersion of Bi_2Te_3 in isopropanol was centrifuged at 3000-4000 rpm for 3 min. The upper dispersion (the top half) was carefully taken out with pipette and the bottom precipitated solid was discarded. This step removes the aggregated nanocrystals, which is critical to obtain the high-quality thin film. The dispersion was spin coated onto an oxygen-plasma-treated polyimide substrate (90 W, 3 min) at a speed of 1000-2000 rpm. Multiple spin coating processes were repeated in order to achieve thicker films. For the post deposition thermal treatment, the films were typically annealed on a hot plate inside of an argon-filled glove box at 300-400°C (573 K-673 K) for 1 hr.

A.4 Aerosol Jet Printing of Bi_2Te_3 Film on Plastic Substrates

Thermoelectric (TE) thin films were printed with an Optomec Aerosol Jet 200 system using the UA-max atomizer. A recirculating bath temperature of 20°C helped to stabilize the ink temperature and prevented the output from being too solvent rich. A tool platen temperature of 40°C was used to ensure drying of the ink once on the substrate, and to minimize oxidation of TE powders while exposed to open air. TE ink exhibited good atomization at 0.450 mA, and the nitrogen flow for the sheath and atomizer were set to 80 and 35 sccm, respectively. TE material was deposited on a polyimide substrate with a 200 μm inner diameter ceramic nozzle and polyethylene tubing. While printing, the nozzle was kept at a constant distance of 3 mm from the substrate, and a serpentine filling pattern having a 30-40% overlap was utilized for the 2 mm by 10 mm printed structures. Printed samples were further dried in an inert glove box, and sintered under argon atmosphere at 350^{o}C for 1 hr.

A.5 AFM Characterization

Bi_2Te_3 nanoplates were imaged using a Bruker Dimension Icon AFM housed in an inert argon environment containing <0.1 ppm H_2O and O_2. Imaging was performed using a ScanAsyst-Air probe (Bruker, 2 nm nominal radius of curvature) operating in PeakForce Tapping mode. Once acquired, the images were processed with a first order flatten to remove sample tip and tilt as well as any line-to-line offsets in the Z-axis. Thirty five nanoplates were imaged to derive statistics. The height of each nanoplate was recorded as the peak value from the substrate, excluding any particulates present in the image. Width measurements were obtained for each of the three pairs of sides on the hexagonal nanoplates and averaged to report a lateral dimension.

A.6 SEM Characterization

SEM characterizations were performed using scanning electron microscopy (SEM, JEOL JSM-6700F FE-SEM) with an acceleration voltage of 5 KV.

A.7 TEM Ink Characterization

TEM samples were prepared by diluting the ink with isopropyl alcohol and drop casting onto a 300 mesh TEM Cu grid coated with a carbon support film. Bright-field, high resolution lattice imaging (HREM) and selected area electron diffraction (SAED) studies were

carried out using a JEOL 2100 HR transmission electron microscope (TEM) operated at 200 kV. Energy dispersive x-ray spectroscopy (EDS) line scans and EELS/EFTEM were performed using a FEI Tecnai G^2 F30 STwin scanning transmission electron microscope (STEM) operated at 300kV.

A.8 TEM Film Characterization

The TEM lamellas were prepared using lift-out technique in a FEI Quanta 3D FEG dual-beam Focused ion beam (FIB). Microstructure characterization was carried out by using a FEI Tecnai G^2 F30 STEM FEG scanning transmission electron microscope (STEM) at 300kV. Both bright-field (BF) imaging technique in TEM mode and Z-contrast imaging technique in STEM mode were utilized to reveal fine structures of the flakes and porosity of the two samples. Energy dispersive x-ray spectroscopy (EDS) technique was used to confirm sample composition.

A.9 Thermoelectric Measurement

Temperature-dependent in-plane Seebeck coefficient and electrical conductivity measurements were performed simultaneously using a commercial Linseis Seebeck and Resistivity instrument in a helium atmosphere. Determining the Seebeck coefficient consisted of measuring the Seebeck voltage and the temperature difference established in parallel to the sample surface. The electrical resistivity measurements used a linear four-probe configuration. The measurement uncertainties are less than 3% for the Seebeck coefficient and 2% for the electrical conductivity.

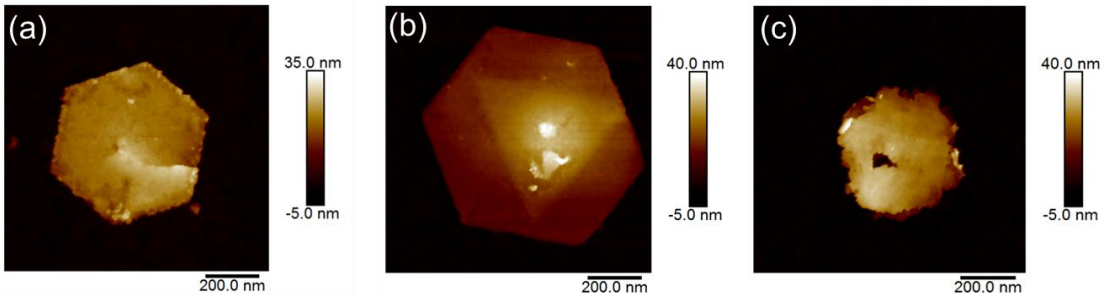

Figure A.1: Atomic force microscopy (AFM) images depicting the three types of Bi_2Te_3 nanoplate morphology observed in this study. (a) Pristine flat morphology (b) Screw – dislocation in the center of the flake as indicated by a triangular growth region, and (c) coarse morphology with rough edges and pores.

(a)

	Result type	Atomic %
	Te	Bi
Spectrum 1	65.99	34.01
Spectrum 2	65.13	34.87
Spectrum 3	66.64	33.36

(b)

	Result type	Atomic %
	Te	Bi
Spectrum 1	62.88	37.12
Spectrum 2	62.67	37.33
Spectrum 3	62.38	37.62

Figure A.2: Energy-dispersive X-ray spectroscopy (EDS) of Bi_2Te_3 ink. (a) Composition of ink created by UCLA, (b) composition of ink created by University of Idaho.

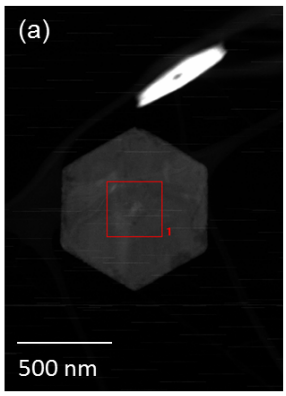

(b)

Element	Weight %	Atomic %
Te	59.05	70.25
Bi	40.94	29.74

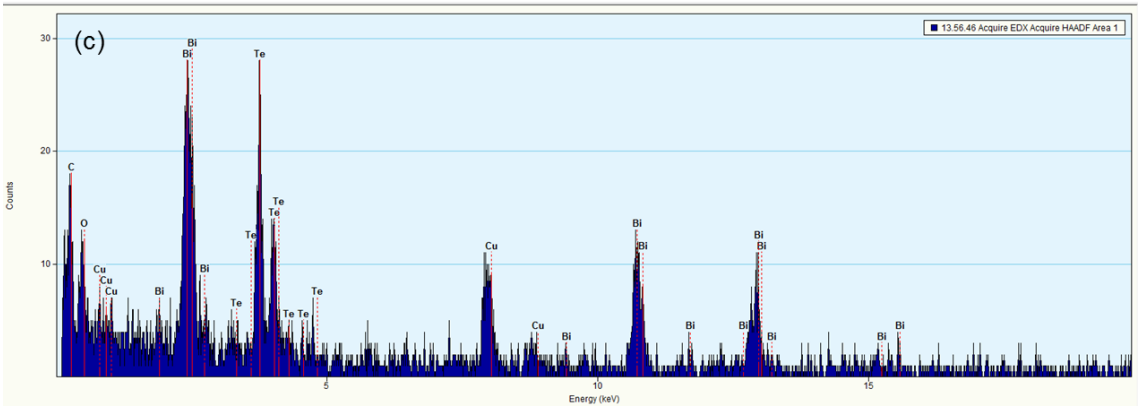

Figure A.3: Energy-dispersive X-ray Spectroscopy (EDS) of Bi_2Te_3 nanoplate. (a) STEM Z-contrast image of a Bi_2Te_3 nanoplate, (b) table of composition, (c) EDS spectrum.

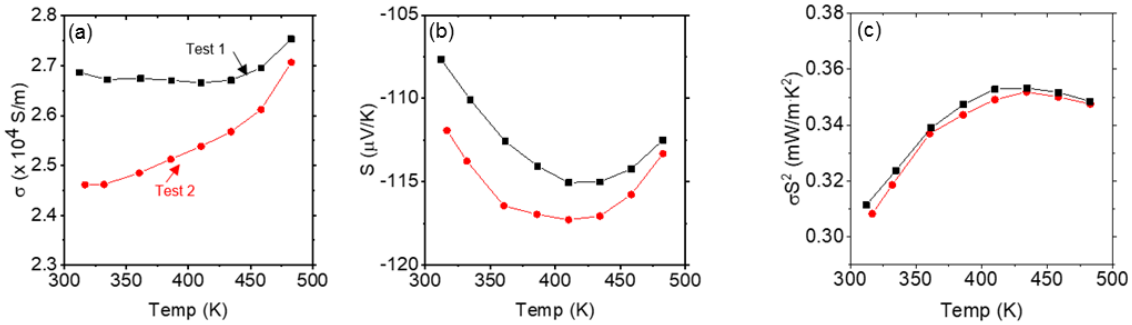

Figure A.4: Thermoelectric measurement cycling test of Bi_2Te_3 spin coated thin film sample annealed at 623 K. (a) electrical conductivity σ, (b) Seebeck coefficient S, and (c) power factor σS^2.

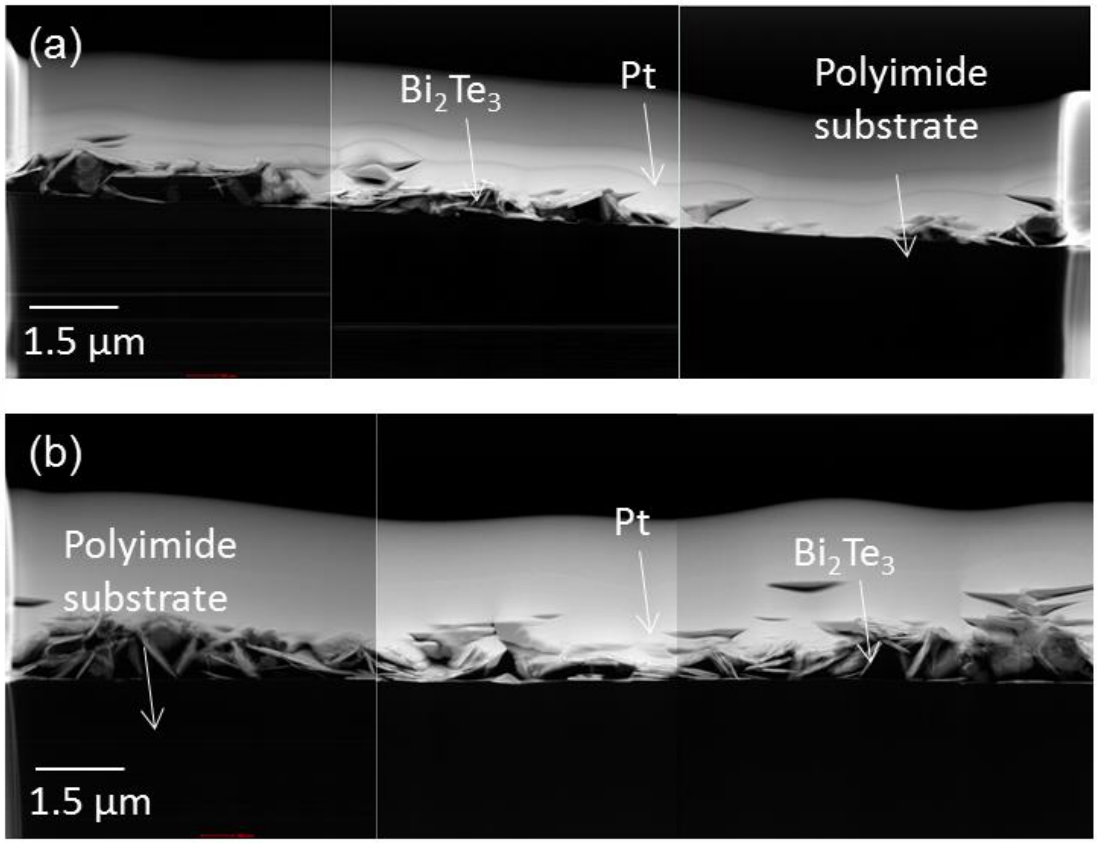

Figure A.5: Scanning Transmission electron microscopy (STEM) cross section of Bi_2Te_3 thin film samples. (a) Spin coated Bi_2Te_3 thin film and (b) aerosol jet printed Bi_2Te_3 thin film.

APPENDIX B: ANALYTIC QUADRUPOLES MODEL CODE

B.1 Experimentally Determine Thermal Conductivity

```
%Transient, multilayered analytic model using the quadrupoles method
%Needle probe - Thermal contact resistance - Sample - Convection
%Determine temperature v. time of needle probe
clear all;
clc;

%Original properties
%Global variables
global R1_cyl
global R2_cyl
global R3_cyl
global a1_cyl
global a2_cyl
global lambda1_cyl
global lambda2_cyl
global length_cyl
global Resist1_cyl
global area_cyl
global h_convect
global Q0

R1_cyl= 0.000447;%inner probe radius [m]
R2_cyl= 0.001;%outer probe radius/inner sample radius [m]
R3_cyl= 0.02;%outer sample radius [m]
a1_cyl= 1.37e-5;%thermal diffusivity of probe [m^2/s]
a2_cyl= 6.2e-7;%thermal diffusivity of sample [m^2/s]
lambda1_cyl= 42;%thermal conductivity of probe [W/mK]
lambda2_cyl= 2.5;%thermal conductivity of sample [W/mK]
length_cyl=0.2;%length of probe [m]
Resist1_cyl=1;%thermal contact resistance [Km^2/W]
area_cyl=2*pi*R3_cyl*length_cyl;%outer sample surface area [m^2]
h_convect=10;%convection coefficient [W/m^2K]
Q0=10;%power [W]

%5% change from original properties
%Global variables
global R1_cyl_high
```

```
global R2_cyl_high
```

```
global R3_cyl_high
```

```
global a1_cyl_high
global a2_cyl_high
global lambda1_cyl_high
global lambda2_cyl_high
global length_cyl_high
global Resist1_cyl_high
global area_cyl_high
global h_convect_high
global Q0_high

R1_cyl_high= 0.000447;%inner probe radius [m]
R2_cyl_high= 0.001;%outer probe radius/inner sample radius [m]
R3_cyl_high= 0.02;%outer sample radius [m]
a1_cyl_high= 1.37e-5;%thermal diffusivity of probe [m^2/s]
a2_cyl_high= 6.2e-7;%thermal diffusivity of sample [m^2/s]
lambda1_cyl_high=42;%thermal conductivity of probe [W/mK]
lambda2_cyl_high= 2.5;%thermal conductivity of sample [W/mK]
length_cyl_high=0.2;%length of probe [m]
Resist1_cyl_high=1;%thermal contact resistance [Km^2/W]
area_cyl_high=2*pi*R3_cyl*length_cyl;%outer sample surface area [m^2]
h_convect_high=10;%convection coefficient [W/m^2K]
Q0_high=10;%power [W]

t_step=0.1;%time increment
t_start=0.1;%initial time
t_final=10000;%final time
S_final=round(((t_final-t_start)/t_step)+1);%# of time elements

%Based on original properties
t=[t_start:t_step:t_final]';%time matrix
f=invlap('identity',t,0,1e-9);%calculate the Laplace inverse
%transform of the function using "Identity.m" over t.
%See Invlap.m for other defn's.
dy = diff(f(:))./diff(log(t(:)));%derivative of Temp. v. time curve

%Based on 5% change from original properties
f_high=invlap('identity_high',t,0,1e-9);%calculate the Laplace inverse
%transform of the function using "Identity.m" over t.
```

```
%See Invlap.m for other defn's.
dy_high = diff(f_high(:))./diff(log(t(:)));%derivative of Temp. v. time curve
```

```
%Determine known thermal conductivity and +/- 5% range
```

```
%using traditional slope method
initial_S=1;
S_actual=zeros(S_final,1);
S_low=zeros(S_final,1);
S_high=zeros(S_final,1);
for S_initial=1:S_final;
S_actual(S_initial,:)=Q0/(4*pi*length_cyl*lambda2_cyl);
S_low(S_initial,:)=(Q0/(4*pi*length_cyl*lambda2_cyl))*.95;
S_high(S_initial,:)=(Q0/(4*pi*length_cyl*lambda2_cyl))*1.05;
end

%Determining sensitivity change
delta_h_high=(dy_high-dy);
sensitivity_h_high=delta_h_high./dy_high*100;

%Graph sensitivity change
figure (3)
plot(t(2:end),sensitivity_h_high)
hold on
set(gca, 'XScale','log');
xlabel('Time (s)');
ylabel('delta(r3)/r3 (%)');
title('Sensitivity plot','FontWeight','bold');

%%%%%%%% INVLAP  numerical inverse Laplace transform  %%%%%%%%%%%%%%%%%%

% f = invlap(F, t, alpha, tol, P1,P2,P3,P4,P5,P6,P7,P8,P9);
%
% F       laplace-space function (string refering to an m-file),
%           must have form F(s, P1,..,P9), where s is the Laplace parameter,
%           and return column vector as result
% t       column vector of times for which real-space function values are
%           sought
% alpha   largest pole of F (default zero)
% tol     numerical tolerance of approaching pole (default 1e-9)
% P1-P9   optional parameters to be passed on to F
```

```
% f       vector of real-space values f(t)
%
% example: identity function in Laplace space:
%   function F = identity(s);                    % save these two lines
%            F = 1./(s.^2);                      % ...  as "identity.m"
%   invlap('identity', [1;2;3])                  % gives [1;2;3]
%
% algorithm: de Hoog et al's quotient difference method with accelerated
%   convergence for the continued fraction expansion
%   [de Hoog, F. R., Knight, J. H., and Stokes, A. N. (1982). An improved
%    method for numerical inversion of Laplace transforms. S.I.A.M. J. Sci.
%    and Stat. Comput., 3, 357-366.]
% Modification: The time vector is split in segments of equal magnitude
%   which are inverted individually. This gives a better overall accuracy.

%  details: de Hoog et al's algorithm f4 with modifications (T->2*T and
%    introduction of tol). Corrected error in formulation of z.
%
%  Copyright: Karl Hollenbeck
%             Department of Hydrodynamics and Water Resources
%             Technical University of Denmark, DK-2800 Lyngby
%             email: karl@isv16.isva.dtu.dk
%  22 Nov 1996, MATLAB 5 version 27 Jun 1997 updated 1 Oct 1998
%  IF YOU PUBLISH WORK BENEFITING FROM THIS M-FILE, PLEASE CITE IT AS:
%    Hollenbeck, K. J. (1998) INVLAP.M: A matlab function for numerical
%    inversion of Laplace transforms by the de Hoog algorithm,
%    http://www.isva.dtu.dk/staff/karl/invlap.htm

function f = invlap(F, t, alpha, tol, P1,P2,P3,P4,P5,P6,P7,P8,P9);

if nargin <= 2,
  alpha = 0;
elseif isempty(alpha),
  alpha = 0;
end
if nargin <= 3,
  tol = 1e-9;
elseif isempty(tol),
  tol = 1e-9;
end
```

```
      f = [];

      % split up t vector in pieces of same order of magnitude, invert one piece
      %   at a time. simultaneous inversion for times covering several orders of
      %   magnitudes gives inaccurate results for the small times.

      allt = t;                                % save full times vector
      logallt = log10(allt);
      iminlogallt = floor(min(logallt));
      imaxlogallt = ceil(max(logallt));
      for ilogt = iminlogallt:imaxlogallt,     % loop through all pieces

        t = allt(find((logallt>=ilogt) & (logallt<(ilogt+1))));
        if ~isempty(t),                        % maybe no elements in that magnitude

          T = max(t)*2;
          gamma = alpha-log(tol)/(2*T);
          % NOTE: The correction alpha -> alpha-log(tol)/(2*T) is not in de Hoog's
          %   paper, but in Mathematica's Mathsource (NLapInv.m) implementation of
          %   inverse transforms
          nt = length(t);
          M = 20;
          run = [0:1:2*M]';    % so there are 2M+1 terms in Fourier series
expansion

          % find F argument, call F with it, get 'a' coefficients in power series
          s = gamma + i*pi*run/T;
          command = ['a = ' F '(s'];
          if nargin > 4,                       % pass on parameters
            for iarg = 1:nargin-4,
                  command = [command ',P' int2str(iarg)];
            end
          end
          command = [command ');'];
          eval(command);
          a(1) = a(1)/2;                       % zero term is halved

          % build up e and q tables. superscript is now row index, subscript column
          %   CAREFUL: paper uses null index, so all indeces are shifted by 1 here
          e = zeros(2*M+1, M+1);
```

```
          q = zeros(2*M  , M+1);              % column 0 (here: 1) does not exist
          e(:,1) = zeros(2*M+1,1);
          q(:,2) = a(2:2*M+1,1)./a(1:2*M,1);
          for r = 2:M+1,                      % step through columns (called r...)
            e(1:2*(M-r+1)+1,r) = ...
                q(2:2*(M-r+1)+2,r) - q(1:2*(M-r+1)+1,r) + e(2:2*(M-r+1)+2,r-1);
            if r<M+1,                         % one column fewer for q
              rq = r+1;
              q(1:2*(M-rq+1)+2,rq) = ...
                 q(2:2*(M-rq+1)+3,rq-1).*e(2:2*(M-rq+1)+3,rq-1)./e(1:2*(M-rq+1)+2,rq-
1);
            end
          end

          % build up d vector (index shift: 1)
          d = zeros(2*M+1,1);
          d(1,1) = a(1,1);
          d(2:2:2*M,1) = -q(1,2:M+1).'; % these 2 lines changed after niclas
          d(3:2:2*M+1,1) = -e(1,2:M+1).'; % ...

          % build up A and B vectors (index shift: 2)
          %   - now make into matrices, one row for each time
          A = zeros(2*M+2,nt);
          B = zeros(2*M+2,nt);
          A(2,:) = d(1,1)*ones(1,nt);
          B(1:2,:) = ones(2,nt);
          z = exp(i*pi*t'/T);          % row vector
          % after niclas back to the paper (not: z = exp(-i*pi*t/T)) !!!
          for n = 3:2*M+2,
            A(n,:) = A(n-1,:) + d(n-1,1)*ones(1,nt).*z.*A(n-2,:);  % different
index
            B(n,:) = B(n-1,:) + d(n-1,1)*ones(1,nt).*z.*B(n-2,:);  %  shift for d!
          end

          % double acceleration
          h2M = .5 * ( ones(1,nt) + ( d(2*M,1)-d(2*M+1,1) )*ones(1,nt).*z );
          R2Mz = -h2M.*(ones(1,nt) - ...
              (ones(1,nt)+d(2*M+1,1)*ones(1,nt).*z/(h2M).^2).^.5);
          A(2*M+2,:) = A(2*M+1,:) + R2Mz .* A(2*M,:);
          B(2*M+2,:) = B(2*M+1,:) + R2Mz .* B(2*M,:);
```

```
            % inversion, vectorized for times, make result a column vector
            fpiece = ( 1/T * exp(gamma*t') .* real(A(2*M+2,:)./B(2*M+2,:)) )';
            f = [f; fpiece];                    % put pieces together

          end % if not empty time piece

        end % loop through time vector pieces
        end

        %Original properties

        %Needle probe - Thermal contact resistance - Sample - Convection

        function F = identity(s);
        global R1_cyl
        global R2_cyl
        global R3_cyl
        global a1_cyl
        global a2_cyl
        global lambda1_cyl
        global lambda2_cyl
        global length_cyl
        global Resist1_cyl
        global area_cyl
        global h_convect
        global Q0

        alpha11_cyl=R1_cyl.*sqrt(s/a1_cyl);%alpha1 for probe (material 1)
        alpha21_cyl=R2_cyl.*sqrt(s/a1_cyl);%alpha2 for probe (material 1)

        alpha12_cyl=R2_cyl.*sqrt(s/a2_cyl);%alpha1 for sample (material 2)
        alpha22_cyl=R3_cyl.*sqrt(s/a2_cyl);%alpha2 for sample (material 2)

        A_material1=alpha21_cyl.*((besseli(0,alpha11_cyl).*besselk(1,alpha21_cyl))+(b
esseli(1,alpha21_cyl).*besselk(0,alpha11_cyl)));
        B_material1=(1/(2.*pi.*lambda1_cyl.*length_cyl)).*((besseli(0,alpha21_cyl).*b
esselk(0,alpha11_cyl))-(besseli(0,alpha11_cyl).*besselk(0,alpha21_cyl)));
        C_material1=2.*pi.*lambda1_cyl.*length_cyl.*alpha11_cyl.*alpha21_cyl.*((besse
li(1,alpha21_cyl).*besselk(1,alpha11_cyl))-
(besseli(1,alpha11_cyl).*besselk(1,alpha21_cyl)));
```

```
      D_material1=alpha11_cyl.*((besseli(0,alpha21_cyl).*besselk(1,alpha11_cyl))+(b
esseli(1,alpha11_cyl).*besselk(0,alpha21_cyl)));

      A_resistance1=1;
      B_resistance1= Resist1_cyl;
      C_resistance1=0;
      D_resistance1=1;

      A_material2=alpha22_cyl.*((besseli(0,alpha12_cyl).*besselk(1,alpha22_cyl))+(b
esseli(1,alpha22_cyl).*besselk(0,alpha12_cyl)));
      B_material2=(1/(2.*pi.*lambda2_cyl.*length_cyl)).*((besseli(0,alpha22_cyl).*b
esselk(0,alpha12_cyl))-(besseli(0,alpha12_cyl).*besselk(0,alpha22_cyl)));
```

```
      C_material2=2.*pi.*lambda2_cyl.*length_cyl.*alpha12_cyl.*alpha22_cyl.*((besse
li(1,alpha22_cyl).*besselk(1,alpha12_cyl))-
(besseli(1,alpha12_cyl).*besselk(1,alpha22_cyl)));
```

```
      D_material2=alpha12_cyl.*((besseli(0,alpha22_cyl).*besselk(1,alpha12_cyl))+(b
esseli(1,alpha12_cyl).*besselk(0,alpha22_cyl)));

      A_convection=1;
      B_convection=0;
      C_convection=h_convect*area_cyl;
      D_convection=1;

      F=(Q0).*((A_material2.*A_material1)+(C_material2.*B_resistance1.*A_material1)
+(C_material2.*B_material1)+(C_convection.*A_material1.*B_material2)+(C_convection.
*D_material2.*B_resistance1.*A_material1)+(C_convection.*D_material2.*B_material1))
./(s.*((A_material2.*C_material1)+(C_material2.*B_resistance1.*C_material1)+(C_mate
rial2.*D_material1)+(C_convection.*B_material2.*C_material1)+(C_convection.*D_mater
ial2.*B_resistance1.*C_material1)+(C_convection.*D_material2.*D_material1)));
      end


      %5% change from original properties
      %Needle probe - Thermal contact resistance - Sample - Convection
      function F = identity_high(s);
      global R1_cyl_high
      global R2_cyl_high
      global R3_cyl_high
      global a1_cyl_high
      global a2_cyl_high
```

```
        global lambda1_cyl_high
        global lambda2_cyl_high
        global length_cyl_high
        global Resist1_cyl_high
        global area_cyl_high
        global h_convect_high
        global Q0_high

        alpha11_cyl_high=R1_cyl_high.*sqrt(s/a1_cyl_high);%alpha1 for probe (material
1)
        alpha21_cyl_high=R2_cyl_high.*sqrt(s/a1_cyl_high);%alpha2 for probe (material
1)
```

```
        alpha12_cyl_high=R2_cyl_high.*sqrt(s/a2_cyl_high);%alpha1 for sample
(material 2)
```

```
        alpha22_cyl_high=R3_cyl_high.*sqrt(s/a2_cyl_high);%alpha2 for sample
(material 2)

        A_material1_high=alpha21_cyl_high.*((besseli(0,alpha11_cyl_high).*besselk(1,a
lpha21_cyl_high))+(besseli(1,alpha21_cyl_high).*besselk(0,alpha11_cyl_high)));
        B_material1_high=(1/(2.*pi.*lambda1_cyl_high.*length_cyl_high)).*((besseli(0,
alpha21_cyl_high).*besselk(0,alpha11_cyl_high))-
(besseli(0,alpha11_cyl_high).*besselk(0,alpha21_cyl_high)));
        C_material1_high=2.*pi.*lambda1_cyl_high.*length_cyl_high.*alpha11_cyl_high.*
alpha21_cyl_high.*((besseli(1,alpha21_cyl_high).*besselk(1,alpha11_cyl_high))-
(besseli(1,alpha11_cyl_high).*besselk(1,alpha21_cyl_high)));
        D_material1_high=alpha11_cyl_high.*((besseli(0,alpha21_cyl_high).*besselk(1,a
lpha11_cyl_high))+(besseli(1,alpha11_cyl_high).*besselk(0,alpha21_cyl_high)));

        A_resistance1_high=1;
        B_resistance1_high= Resist1_cyl_high;
        C_resistance1_high=0;
        D_resistance1_high=1;

        A_material2_high=alpha22_cyl_high.*((besseli(0,alpha12_cyl_high).*besselk(1,a
lpha22_cyl_high))+(besseli(1,alpha22_cyl_high).*besselk(0,alpha12_cyl_high)));
        B_material2_high=(1/(2.*pi.*lambda2_cyl_high.*length_cyl_high)).*((besseli(0,
alpha22_cyl_high).*besselk(0,alpha12_cyl_high))-
(besseli(0,alpha12_cyl_high).*besselk(0,alpha22_cyl_high)));
```

```
      C_material2_high=2.*pi.*lambda2_cyl_high.*length_cyl_high.*alpha12_cyl_high.*
alpha22_cyl_high.*((besseli(1,alpha22_cyl_high).*besselk(1,alpha12_cyl_high))-
(besseli(1,alpha12_cyl_high).*besselk(1,alpha22_cyl_high)));
      D_material2_high=alpha12_cyl_high.*((besseli(0,alpha22_cyl_high).*besselk(1,a
lpha12_cyl_high))+(besseli(1,alpha12_cyl_high).*besselk(0,alpha22_cyl_high)));

      A_convection_high=1;
      B_convection_high=0;
      C_convection_high=h_convect_high*area_cyl_high;
      D_convection_high=1;

      F=(Q0_high).*((A_material2_high.*A_material1_high)+(C_material2_high.*B_resis
tance1_high.*A_material1_high)+(C_material2_high.*B_material1_high)+(C_convection_h
igh.*A_material1_high.*B_material2_high)+(C_convection_high.*D_material2_high.*B_re
sistance1_high.*A_material1_high)+(C_convection_high.*D_material2_high.*B_material1
_high))./(s.*((A_material2_high.*C_material1_high)+(C_material2_high.*B_resistance1
_high.*C_material1_high)+(C_material2_high.*D_material1_high)+(C_convection_high.*B
_material2_high.*C_material1_high)+(C_convection_high.*D_material2_high.*B_resistan
ce1_high.*C_material1_high)+(C_convection_high.*D_material2_high.*D_material1_high)
));
      end
```

B.2 Parameter Sensitivity Study

```
%Transient, multilayered analytic model using the quadrupoles method
%Needle probe - Thermal contact resistance - Sample - Convection
%Determine temperature v. time of needle probe
clear all;
clc;

%Original properties
%Global variables
global R1_cyl
global R2_cyl
global R3_cyl
global a1_cyl
global a2_cyl
global lambda1_cyl
global lambda2_cyl
global length_cyl
global Resist1_cyl
global area_cyl
global h_convect
global Q0

R1_cyl= 0.000447;%inner probe radius [m]
R2_cyl= 0.001;%outer probe radius/inner sample radius [m]
R3_cyl= 0.02;%outer sample radius [m]
a1_cyl= 1.37e-5;%thermal diffusivity of probe [m^2/s]
a2_cyl= 6.2e-7;%thermal diffusivity of sample [m^2/s]
lambda1_cyl= 42;%thermal conductivity of probe [W/mK]
lambda2_cyl= 2.5;%thermal conductivity of sample [W/mK]
length_cyl=0.2;%length of probe [m]
Resist1_cyl=1;%thermal contact resistance [Km^2/W]
area_cyl=2*pi*R3_cyl*length_cyl;%outer sample surface area [m^2]
h_convect=10;%convection coefficient [W/m^2K]
Q0=10;%power [W]

%5% change from original properties
%Global variables
global R1_cyl_high
global R2_cyl_high
global R3_cyl_high
global a1_cyl_high
```

```
global a2_cyl_high
global lambda1_cyl_high
global lambda2_cyl_high
global length_cyl_high
global Resist1_cyl_high
global area_cyl_high
global h_convect_high
global Q0_high

R1_cyl_high= 0.000447;%inner probe radius [m]
R2_cyl_high= 0.001;%outer probe radius/inner sample radius [m]
R3_cyl_high= 0.02;%outer sample radius [m]
a1_cyl_high= 1.37e-5;%thermal diffusivity of probe [m^2/s]
a2_cyl_high= 6.2e-7;%thermal diffusivity of sample [m^2/s]
lambda1_cyl_high=42;%thermal conductivity of probe [W/mK]
lambda2_cyl_high= 2.5;%thermal conductivity of sample [W/mK]
length_cyl_high=0.2;%length of probe [m]
Resist1_cyl_high=1;%thermal contact resistance [Km^2/W]
area_cyl_high=2*pi*R3_cyl*length_cyl;%outer sample surface area [m^2]
h_convect_high=10;%convection coefficient [W/m^2K]
Q0_high=10;%power [W]

t_step=0.1;%time increment
t_start=0.1;%initial time
t_final=10000;%final time
S_final=round(((t_final-t_start)/t_step)+1);%# of time elements

%Based on original properties
t=[t_start:t_step:t_final]';%time matrix
f=invlap('identity',t,0,1e-9);%calculate the Laplace inverse
%transform of the function using "Identity.m" over t.
%See Invlap.m for other defn's.
dy = diff(f(:))./diff(log(t(:)));%derivative of Temp. v. time curve

%Based on 5% change from original properties
f_high=invlap('identity_high',t,0,1e-9);%calculate the Laplace inverse
%transform of the function using "Identity.m" over t.
%See Invlap.m for other defn's.
dy_high = diff(f_high(:))./diff(log(t(:)));%derivative of Temp. v. time curve

%Determine known thermal conductivity and +/- 5% range
```

```
%using traditional slope method

initial_S=1;

S_actual=zeros(S_final,1);
S_low=zeros(S_final,1);
S_high=zeros(S_final,1);
for S_initial=1:S_final;
S_actual(S_initial,:)=Q0/(4*pi*length_cyl*lambda2_cyl);
S_low(S_initial,:)=(Q0/(4*pi*length_cyl*lambda2_cyl))*.95;
S_high(S_initial,:)=(Q0/(4*pi*length_cyl*lambda2_cyl))*1.05;
end

%Determining sensitivity change
delta_h_high=(dy_high-dy);
sensitivity_h_high=delta_h_high./dy_high*100;

%Graph sensitivity change
figure (3)
plot(t(2:end),sensitivity_h_high)
hold on
set(gca, 'XScale','log');
xlabel('Time (s)');
ylabel('delta(r3)/r3 (%)');
title('Sensitivity plot','FontWeight','bold');

%%%%%%%% INVLAP  numerical inverse Laplace transform  %%%%%%%%%%%%%%%%%%

% f = invlap(F, t, alpha, tol, P1,P2,P3,P4,P5,P6,P7,P8,P9);
%
% F       laplace-space function (string refering to an m-file),
%           must have form F(s, P1,..,P9), where s is the Laplace parameter,
%           and return column vector as result
% t       column vector of times for which real-space function values are
%           sought
% alpha   largest pole of F (default zero)
% tol     numerical tolerance of approaching pole (default 1e-9)
% P1-P9   optional parameters to be passed on to F
% f       vector of real-space values f(t)
%
% example: identity function in Laplace space:
%   function F = identity(s);                    % save these two lines
```

```
%            F = 1./(s.^2);                      % ...  as "identity.m"
%   invlap('identity', [1;2;3])                  % gives [1;2;3]
%
% algorithm: de Hoog et al's quotient difference method with accelerated
%   convergence for the continued fraction expansion
%   [de Hoog, F. R., Knight, J. H., and Stokes, A. N. (1982). An improved
%    method for numerical inversion of Laplace transforms. S.I.A.M. J. Sci.
%    and Stat. Comput., 3, 357-366.]
% Modification: The time vector is split in segments of equal magnitude
%   which are inverted individually. This gives a better overall accuracy.

%  details: de Hoog et al's algorithm f4 with modifications (T->2*T and
%    introduction of tol). Corrected error in formulation of z.
%
%  Copyright: Karl Hollenbeck
%             Department of Hydrodynamics and Water Resources
%             Technical University of Denmark, DK-2800 Lyngby
%             email: karl@isv16.isva.dtu.dk
%  22 Nov 1996, MATLAB 5 version 27 Jun 1997 updated 1 Oct 1998
%  IF YOU PUBLISH WORK BENEFITING FROM THIS M-FILE, PLEASE CITE IT AS:
%    Hollenbeck, K. J. (1998) INVLAP.M: A matlab function for numerical
%    inversion of Laplace transforms by the de Hoog algorithm,
%    http://www.isva.dtu.dk/staff/karl/invlap.htm

function f = invlap(F, t, alpha, tol, P1,P2,P3,P4,P5,P6,P7,P8,P9);

if nargin <= 2,
  alpha = 0;
elseif isempty(alpha),
  alpha = 0;
end
if nargin <= 3,
  tol = 1e-9;
elseif isempty(tol),
  tol = 1e-9;
end
f = [];

% split up t vector in pieces of same order of magnitude, invert one piece
%   at a time. simultaneous inversion for times covering several orders of
```

```
        %   magnitudes gives inaccurate results for the small times.

        allt = t;                                % save full times vector
        logallt = log10(allt);
        iminlogallt = floor(min(logallt));
        imaxlogallt = ceil(max(logallt));
        for ilogt = iminlogallt:imaxlogallt,     % loop through all pieces

          t = allt(find((logallt>=ilogt) & (logallt<(ilogt+1))));
          if ~isempty(t),                        % maybe no elements in that magnitude

            T = max(t)*2;
            gamma = alpha-log(tol)/(2*T);
            % NOTE: The correction alpha -> alpha-log(tol)/(2*T) is not in de Hoog's
            %   paper, but in Mathematica's Mathsource (NLapInv.m) implementation of
            %   inverse transforms
            nt = length(t);
            M = 20;
            run = [0:1:2*M]';    % so there are 2M+1 terms in Fourier series
expansion

            % find F argument, call F with it, get 'a' coefficients in power series
            s = gamma + i*pi*run/T;
            command = ['a = ' F '(s'];
            if nargin > 4,                       % pass on parameters
              for iarg = 1:nargin-4,
                    command = [command ',P' int2str(iarg)];
              end
            end
            command = [command ');'];
            eval(command);
            a(1) = a(1)/2;                       % zero term is halved

            % build up e and q tables. superscript is now row index, subscript column
            %   CAREFUL: paper uses null index, so all indeces are shifted by 1 here
            e = zeros(2*M+1, M+1);
            q = zeros(2*M  , M+1);               % column 0 (here: 1) does not exist
            e(:,1) = zeros(2*M+1,1);
            q(:,2) = a(2:2*M+1,1)./a(1:2*M,1);
            for r = 2:M+1,                       % step through columns (called r...)
```

```
            e(1:2*(M-r+1)+1,r) = ...
                q(2:2*(M-r+1)+2,r) - q(1:2*(M-r+1)+1,r) + e(2:2*(M-r+1)+2,r-1);
            if r<M+1,                          % one column fewer for q
              rq = r+1;
              q(1:2*(M-rq+1)+2,rq) = ...
               q(2:2*(M-rq+1)+3,rq-1).*e(2:2*(M-rq+1)+3,rq-1)./e(1:2*(M-rq+1)+2,rq-
1);
            end
          end

          % build up d vector (index shift: 1)
          d = zeros(2*M+1,1);
          d(1,1) = a(1,1);
          d(2:2:2*M,1) = -q(1,2:M+1).'; % these 2 lines changed after niclas
          d(3:2:2*M+1,1) = -e(1,2:M+1).'; % ...

          % build up A and B vectors (index shift: 2)
          %   - now make into matrices, one row for each time
          A = zeros(2*M+2,nt);
          B = zeros(2*M+2,nt);
          A(2,:) = d(1,1)*ones(1,nt);
          B(1:2,:) = ones(2,nt);
          z = exp(i*pi*t'/T);          % row vector
          % after niclas back to the paper (not: z = exp(-i*pi*t/T)) !!!
          for n = 3:2*M+2,
            A(n,:) = A(n-1,:) + d(n-1,1)*ones(1,nt).*z.*A(n-2,:);  % different
index
            B(n,:) = B(n-1,:) + d(n-1,1)*ones(1,nt).*z.*B(n-2,:);  %  shift for d!
          end

          % double acceleration
          h2M = .5 * ( ones(1,nt) + ( d(2*M,1)-d(2*M+1,1) )*ones(1,nt).*z );
          R2Mz = -h2M.*(ones(1,nt) - ...
              (ones(1,nt)+d(2*M+1,1)*ones(1,nt).*z/(h2M).^2).^.5);
          A(2*M+2,:) = A(2*M+1,:) + R2Mz .* A(2*M,:);
          B(2*M+2,:) = B(2*M+1,:) + R2Mz .* B(2*M,:);

          % inversion, vectorized for times, make result a column vector
          fpiece = ( 1/T * exp(gamma*t') .* real(A(2*M+2,:)./B(2*M+2,:)) )';
          f = [f; fpiece];                    % put pieces together
```

```
        end % if not empty time piece

    end % loop through time vector pieces
    end

    %Original properties
    %Needle probe - Thermal contact resistance - Sample - Convection
    function F = identity(s);

    global R1_cyl

    global R2_cyl
    global R3_cyl
    global a1_cyl
    global a2_cyl
    global lambda1_cyl
    global lambda2_cyl
    global length_cyl
    global Resist1_cyl
    global area_cyl
    global h_convect
    global Q0

    alpha11_cyl=R1_cyl.*sqrt(s/a1_cyl);%alpha1 for probe (material 1)
    alpha21_cyl=R2_cyl.*sqrt(s/a1_cyl);%alpha2 for probe (material 1)

    alpha12_cyl=R2_cyl.*sqrt(s/a2_cyl);%alpha1 for sample (material 2)
    alpha22_cyl=R3_cyl.*sqrt(s/a2_cyl);%alpha2 for sample (material 2)

    A_material1=alpha21_cyl.*((besseli(0,alpha11_cyl).*besselk(1,alpha21_cyl))+(b
esseli(1,alpha21_cyl).*besselk(0,alpha11_cyl)));
    B_material1=(1/(2.*pi.*lambda1_cyl.*length_cyl)).*((besseli(0,alpha21_cyl).*b
esselk(0,alpha11_cyl))-(besseli(0,alpha11_cyl).*besselk(0,alpha21_cyl)));
    C_material1=2.*pi.*lambda1_cyl.*length_cyl.*alpha11_cyl.*alpha21_cyl.*((besse
li(1,alpha21_cyl).*besselk(1,alpha11_cyl))-
(besseli(1,alpha11_cyl).*besselk(1,alpha21_cyl)));
    D_material1=alpha11_cyl.*((besseli(0,alpha21_cyl).*besselk(1,alpha11_cyl))+(b
esseli(1,alpha11_cyl).*besselk(0,alpha21_cyl)));

    A_resistance1=1;
    B_resistance1= Resist1_cyl;
```

```
C_resistance1=0;
D_resistance1=1;

A_material2=alpha22_cyl.*((besseli(0,alpha12_cyl).*besselk(1,alpha22_cyl))+(b
esseli(1,alpha22_cyl).*besselk(0,alpha12_cyl)));
B_material2=(1/(2.*pi.*lambda2_cyl.*length_cyl)).*((besseli(0,alpha22_cyl).*b
esselk(0,alpha12_cyl))-(besseli(0,alpha12_cyl).*besselk(0,alpha22_cyl)));
C_material2=2.*pi.*lambda2_cyl.*length_cyl.*alpha12_cyl.*alpha22_cyl.*((besse
li(1,alpha22_cyl).*besselk(1,alpha12_cyl))-
(besseli(1,alpha12_cyl).*besselk(1,alpha22_cyl)));
```

```
D_material2=alpha12_cyl.*((besseli(0,alpha22_cyl).*besselk(1,alpha12_cyl))+(b
esseli(1,alpha12_cyl).*besselk(0,alpha22_cyl)));
```

```
A_convection=1;
B_convection=0;
C_convection=h_convect*area_cyl;
D_convection=1;

F=(Q0).*((A_material2.*A_material1)+(C_material2.*B_resistance1.*A_material1)
+(C_material2.*B_material1)+(C_convection.*A_material1.*B_material2)+(C_convection.
*D_material2.*B_resistance1.*A_material1)+(C_convection.*D_material2.*B_material1))
./(s.*((A_material2.*C_material1)+(C_material2.*B_resistance1.*C_material1)+(C_mate
rial2.*D_material1)+(C_convection.*B_material2.*C_material1)+(C_convection.*D_mater
ial2.*B_resistance1.*C_material1)+(C_convection.*D_material2.*D_material1)));
end


%5% change from original properties
%Needle probe - Thermal contact resistance - Sample - Convection
function F = identity_high(s);
global R1_cyl_high
global R2_cyl_high
global R3_cyl_high
global a1_cyl_high
global a2_cyl_high
global lambda1_cyl_high
global lambda2_cyl_high
global length_cyl_high
global Resist1_cyl_high
global area_cyl_high
```

```
        global h_convect_high
        global Q0_high

        alpha11_cyl_high=R1_cyl_high.*sqrt(s/a1_cyl_high);%alpha1 for probe (material
1)
        alpha21_cyl_high=R2_cyl_high.*sqrt(s/a1_cyl_high);%alpha2 for probe (material
1)

        alpha12_cyl_high=R2_cyl_high.*sqrt(s/a2_cyl_high);%alpha1 for sample
(material 2)
        alpha22_cyl_high=R3_cyl_high.*sqrt(s/a2_cyl_high);%alpha2 for sample
(material 2)
```

```
        A_material1_high=alpha21_cyl_high.*((besseli(0,alpha11_cyl_high).*besselk(1,a
lpha21_cyl_high))+(besseli(1,alpha21_cyl_high).*besselk(0,alpha11_cyl_high)));
        B_material1_high=(1/(2.*pi.*lambda1_cyl_high.*length_cyl_high)).*((besseli(0,
alpha21_cyl_high).*besselk(0,alpha11_cyl_high))-
(besseli(0,alpha11_cyl_high).*besselk(0,alpha21_cyl_high)));
        C_material1_high=2.*pi.*lambda1_cyl_high.*length_cyl_high.*alpha11_cyl_high.*
alpha21_cyl_high.*((besseli(1,alpha21_cyl_high).*besselk(1,alpha11_cyl_high))-
(besseli(1,alpha11_cyl_high).*besselk(1,alpha21_cyl_high)));
        D_material1_high=alpha11_cyl_high.*((besseli(0,alpha21_cyl_high).*besselk(1,a
lpha11_cyl_high))+(besseli(1,alpha11_cyl_high).*besselk(0,alpha21_cyl_high)));

        A_resistance1_high=1;
        B_resistance1_high= Resist1_cyl_high;
        C_resistance1_high=0;
        D_resistance1_high=1;

        A_material2_high=alpha22_cyl_high.*((besseli(0,alpha12_cyl_high).*besselk(1,a
lpha22_cyl_high))+(besseli(1,alpha22_cyl_high).*besselk(0,alpha12_cyl_high)));
        B_material2_high=(1/(2.*pi.*lambda2_cyl_high.*length_cyl_high)).*((besseli(0,
alpha22_cyl_high).*besselk(0,alpha12_cyl_high))-
(besseli(0,alpha12_cyl_high).*besselk(0,alpha22_cyl_high)));
        C_material2_high=2.*pi.*lambda2_cyl_high.*length_cyl_high.*alpha12_cyl_high.*
alpha22_cyl_high.*((besseli(1,alpha22_cyl_high).*besselk(1,alpha12_cyl_high))-
(besseli(1,alpha12_cyl_high).*besselk(1,alpha22_cyl_high)));
        D_material2_high=alpha12_cyl_high.*((besseli(0,alpha22_cyl_high).*besselk(1,a
lpha12_cyl_high))+(besseli(1,alpha12_cyl_high).*besselk(0,alpha22_cyl_high)));
```

```
        A_convection_high=1;
        B_convection_high=0;
        C_convection_high=h_convect_high*area_cyl_high;
        D_convection_high=1;

        F=(Q0_high).*((A_material2_high.*A_material1_high)+(C_material2_high.*B_resis
tance1_high.*A_material1_high)+(C_material2_high.*B_material1_high)+(C_convection_h
igh.*A_material1_high.*B_material2_high)+(C_convection_high.*D_material2_high.*B_re
sistance1_high.*A_material1_high)+(C_convection_high.*D_material2_high.*B_material1
_high)).*(s.*((A_material2_high.*C_material1_high)+(C_material2_high.*B_resistance1
_high.*C_material1_high)+(C_material2_high.*D_material1_high)+(C_convection_high.*B
_material2_high.*C_material1_high)+(C_convection_high.*D_material2_high.*B_resistan
ce1_high.*C_material1_high)+(C_convection_high.*D_material2_high.*D_material1_high)
));
```

```
        end
```